DIE-ENTRY FLOW

OF POLYMERS

ANDREW MARTIN HULL

Department of Chemical Engineering and Chemical Technology
Imperial College of Science and Technology

A Thesis submitted for the degree of
DOCTOR OF PHILOSOPHY, August 1981

ABSTRACT

A theoretical study of die-entry flow is presented with particular emphasis on the experimental rheology of rubber.

Assuming that the die-entry has a large contraction ratio occurring over a short distance or that the flow rates are high, the geometry is idealised to one of infinite extent upstream with a point or line-efflux downstream. An approximation method is advanced which splits the flow field along a streamline into two distinct regions; an inner irrotational sink flow occupying most of the field and an outer highly sheared self-lubricating layer adjacent to the walls. Solutions are obtained with a number of constitutive equations for flow through a wedge and a cone.

Two recently developed machines are used to perform the start-up of simple shear and uniaxial extension. It is established that the machines measure the shear and elongational stresses accurately. Hencky strains in excess of 8 at constant strain rates over 100 s^{-1} are achieved for two highly filled compounds of Butyl and Chloroprene rubbers. In general no steady state is attained. It is shown that the time temperature superposition principle holds for start-up flows resulting in a family of master curves. The elongational stresses are one or two orders of magnitude greater than the shear stresses at comparable deformation rates, which is the necessary dynamic justification for the approximation method above.

An exact solution is presented for the slow flow of a general linear upper convected viscoelastic fluid through a 180° wedge. The solution, which is probably an isolated result, has radial streamlines. It is used to examine the convergence properties of existing perturbation or series solutions, which are found to be divergent. An attempt to obtain a series expansion, valid close to the origin, reveals some novel mathematical difficulties.

ACKNOWLEDGEMENTS

CONTENTS

CHAPTER 1

INTRODUCTION AND BACKGROUND

This thesis is a study of the die-entry flow of polymers, which is a flow through a converging region and plays an important role in a number of engineering and rheological situations. It features in all injection moulding and extrusion processes as well as in capillary rheometry. It also falls into a wider group of flows through converging or diverging sections which include calendering, film blowing and melt-spinning, to name but a few.

The first chapter contains background material, describing previous research into die-entry flows both experimental and theoretical. It will be shown how certain avenues of theoretical research introduce and require a considerable use of rheology as a framework for plausible mathematical modelling of the flow. This provides the motivation for a study and experimental investigation of aspects of the rheology of certain polymers, forming the basis of Chapter 2. The polymers are two types of rubber, namely, Butyl and Chloroprene, which are used mainly in a compounded form with high proportions of carbon black and oil. The principal results obtained are for the

stresses in the start-up of simple shear and constant strain

rate elongational flows. The rates of deformation used in both

of these experiments are comparable to those observed in

typical extrusion and injection moulding processes.

In Chapter 3 an exact solution is presented for the

slow flow of a general viscoelastic fluid through a $180°$

converging channel or wedge. This result is important for a

number of reasons, chief of which is that exact solutions for

such fluids are rare. Another reason is that it should be useful

as a standard for the checking of numerical computations. Also

it sheds light on approximation methods for the converging flow

of slightly elastic, viscous fluids. These methods involve

small perturbations in some parameter related to a measure of fluid

elasticity about a slow flow, which is usually the asymptotic

Newtonian solution. It will be shown that although the perturbations

are an asymptotic series, they are nevertheless divergent.

Finally, an attempt is made to extend the exact solution by

an approximation method valid for highly elastic, viscous fluids.

Chapter 4 describes a different approach to die-entry

flows using an approximation scheme which is valid not only for

converging channels, but also for converging cylinders and annuli.

The scheme is appropriate for highly elastic, shear-thinning fluids

and relies on the experimental data from Chapter 2. The prime

interest is in converging sections either with large contraction

ratios occuring over short distances or for high flow rates.

The other extreme, that of small contraction ratios over large

distances at low flow rates can already be successfully handled

using a lubrication approximation.

Finally, the conclusions of the thesis and possibilities for further work are presented in Chapter 5. It is to be hoped that the experimental innovations of Chapter 2 and particularly the theoretical advances made in Chapters 3 and 4 will lead to other fruitful work in this field.

1.1   Die-Entry Flow - Processing

Die-entry flow refers to the region of flow between the end of the screw, or possibly a ram, in the extruder barrel and the die or nozzle. Fig. 1.1 shows a typical configuration for a cylindrical die. Many other shapes are possible; wedge and annulus dies are particularly common for extrusion processes.
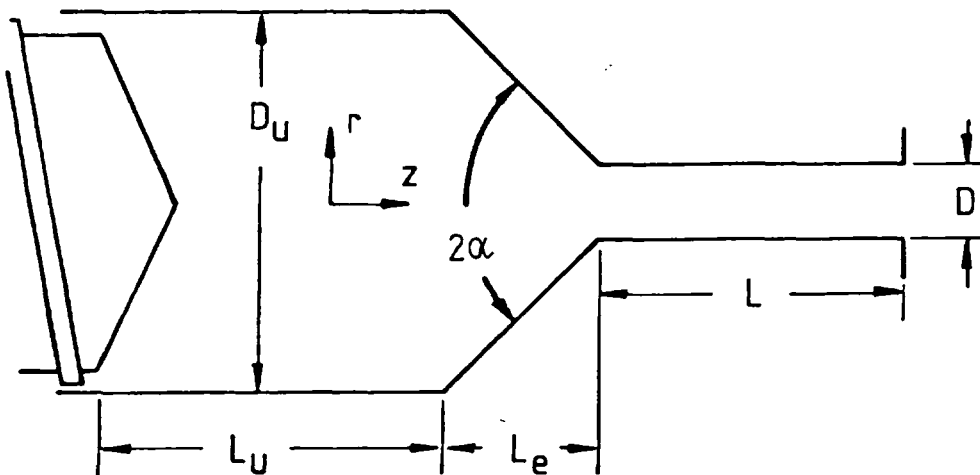

Fig. 1.1 Typical cylindrical die geometry.

The shear rates generated in the die can often be as high as $10^4 s^{-1}$ in injection moulding and fast wire-coating dies but the range of rates normally expected for die-entry flows is $10-10^4 s^{-1}$ [1]. For most melts inertia effects are negligible or small even at the highest rates. However, for some rubber compounds which exhibit

a power-law index of less than 0.1 and for polymer solutions, it may not be possible to disregard inertia effects. On the other hand, heat generation can play a significant role in melt flows, whereas for polymer solutions, isothermal conditions are normally appropriate. A discussion of these effects will be facilitated by way of an example.

A standard design for an injection nozzle used for testing moulding machine performance has the following dimensions [1]; referring to Fig. 1.1,

$$D = 2.38mm, \quad D_u = 15.9mm, \quad L = 25.4mm, \quad 2\alpha = 90^\circ.$$

These dimensions are also similar to those of a Davenport Capillary Rheometer. Estimates of the influence of inertia and heating effects in the die-entry region can be obtained by considering the flow in the nozzle, taking D as the characteristic length scale. A dimensional analysis can be carried out for the nozzle if the lubrication approximation is assumed to hold; i.e. L/D >> 1 and $\partial D/\partial z$ << 1 in which case the velocity field is one-dimensional [2].

The relevant melt properties for a polychloroprene rubber compound at ambient pressure and a processing temperature of 100°C are a reference viscosity μ_o at a shear rate γ_o, power-low index n, temperature coefficient of viscosity b, density ρ, specific heat C_p and thermal conductivity k.

$$\mu_o = 1.3 \times 10^5 \text{N sm}^{-2} \quad \text{at} \quad \dot{\gamma} = 1 \text{ s}^{-1}, \quad n = 0.25$$

$$b = 0.02 \text{K}^{-1}, \quad \rho = 1.17 \times 10^3 \text{kgm}^{-3}, \quad c_p = 2.18 \times 10^3 \text{J kg}^{-1}\text{K}^{-1}$$

$$k = 0.192 \text{ W m}^{-1}\text{K}^{-1}.$$

Two specific choices of the flow rate variables are made

(i)   a standard mass flow rate of 50 g s^{-1}

corresponding to the standard test of

moulding performance,

(ii)   a mean shear rate of 50 s^{-1} corresponding

to the middle of the normal shear rate

range of a capillary rheometer.

Following Pearson [2] characteristic Reynolds, Graetz and

Nahme-Griffith numbers can be calculated. (It should be pointed

out that polychloroprene satisfies the no-slip boundary condition

over a wide shear rate range.)   These require, a characteristic

mean velocity $\bar{U}$, shear rate $\bar{\dot{\gamma}}$, stress $\bar{\tau}$ and viscosity $\bar{\mu}$. Also a

characteristic mean extrusion rate $\bar{\dot{\epsilon}}$, Wiessenberg and Deborah

numbers are calculated although their relevance only becomes clear

later on. The volumetric flow rate is given by Q, and λ is

relaxation time in seconds.

		(i)	(ii)
$\bar{U} = \left\| \dfrac{4Q}{\pi D^2} \right\|$		9.6 ms^{-1}	$.12 \text{ms}^{-1}$
$\bar{\dot{\gamma}} = \dfrac{\bar{U}}{D}$		$4.0 \times 10^3 \text{ s}^{-1}$	50 s^{-1}

$$\bar{\dot{\epsilon}} = \frac{U_u + U}{2L_e} \ell n \left(\frac{D_u}{D} \right)^2 \qquad\qquad 2\times10^3 \ s^{-1} \qquad\qquad 28 \ s^{-1}$$

$$\bar{\mu} = \mu_o \left(\frac{\bar{\dot{\gamma}}}{\dot{\gamma}_o} \right)^{n-1} \qquad\qquad 260 \ N \ sm^{-2} \qquad\qquad 6.9\times10^3 N \ sm^{-2}$$

$$Re = \frac{\rho \bar{U} D}{\bar{\mu}} \qquad\qquad 0.10 \qquad\qquad 48\times10^{-6}$$

$$Gz = \frac{\rho C_p \bar{U} D^2}{kL} \qquad\qquad 2.8\times10^4 \qquad\qquad 3.6\times10^2$$

$$Na = \frac{b\bar{\dot{\tau\gamma}}D^2}{k} \qquad\qquad 2.4\times10^3 \qquad\qquad 10$$

$$Ws = \frac{\lambda Q}{D^3} \qquad\qquad 3\times10^3\lambda \qquad\qquad 40\lambda$$

$$De = \frac{\lambda Q}{D^2 L_e} \qquad\qquad 10^3\lambda \qquad\qquad 10\lambda$$

If the relaxation time is taken to be constant, then it can be estimated from the data of Chapter 2 to lie within 10-100s , so clearly elastic effects are considerable for a wide flow rate range, demonstrated by the high values of the Weissenberg and Deborah numbers. If λ is taken as the maximum relaxation time in steady simple shear flow defined as [3]

$$\lambda = \frac{\tau_{11} - \tau_{22}}{2\tau_{12}\dot{\gamma}} \qquad\qquad (1.1)$$

in which $\tau_{11} - \tau_{22}$ and τ_{12} are the first normal stress difference and shear stress, respectively, then the limited data of Chapter 2 suggests that λ decreases with $\dot{\gamma}$ such that at sufficiently high shear rates

$$\lambda \dot{\gamma} \sim 1 \qquad\qquad\qquad (1.2)$$

This behaviour is confirmed for other melts, including LDPE and HDPE, by the data of Ide and White [3]. Using this value of λ would mean that

$$Ws = \frac{\lambda Q}{D^3} = \lambda \dot{\gamma} \sim 1 \qquad\qquad\qquad (1.3)$$

But the flow through a converging region contains an extensional component. Comparing $\bar{\epsilon}$ with $\bar{\dot{\gamma}}$ shows that the mean extension rate and shear rate are of comparable magnitude.

The Reynolds numbers are small for both (i) and (ii) and slow flow is a valid assumption. The large Graetz numbers indicate that heat convection dominates heat conduction except near the walls bounding the flow. Again following Pearson [2], the ratios of the Nahme-Griffiths to the Graetz number are 0.09(i), 0.028(ii) which indicates that heat generation is negligible. This is because the temperature profile is developing and the mean residence times $L/\bar{U}$, a factor which is accounted for in Na/Gz, are small. An isothermal analysis may be a reasonable first approximation [1].

Such heating that does occur will be situated near the walls bounding the flow. This will give rise to a flow situation where a hot low-viscosity layer lubricates a relatively cool core. Fenner [1] shows that the combined integrated effects of pressure and temperature on the viscosity roughly compensate for each other. This is probably too simple in view of the remark above, whereas the pressure field is approximately uniform across the flow, temperature rises will be non-uniform with the maximum in the

temperature profile occuring near the walls.

1.2   Die-Entry Flow - Experimental

Since the publication of the now famous photographs by

Giesekus [4] in 1969 showing large toroidal vortices in the velocity

field of an aqueous polyacrylamide solution near a sudden

cylindrical contraction, a large number of investigations into this

phenomenon have appeared. The basic geometry of the region is

shown in Fig. 1.2 with recirculating vortices either for a

cylindrical or wedge contraction. Only half of the flow field

is shown.   Not all melts and polymer solutions exhibit such

vortices, nor are vortices exhibited for all entrance angles, 2α.

A definitive study has been given by White and Kondo [5]. Their

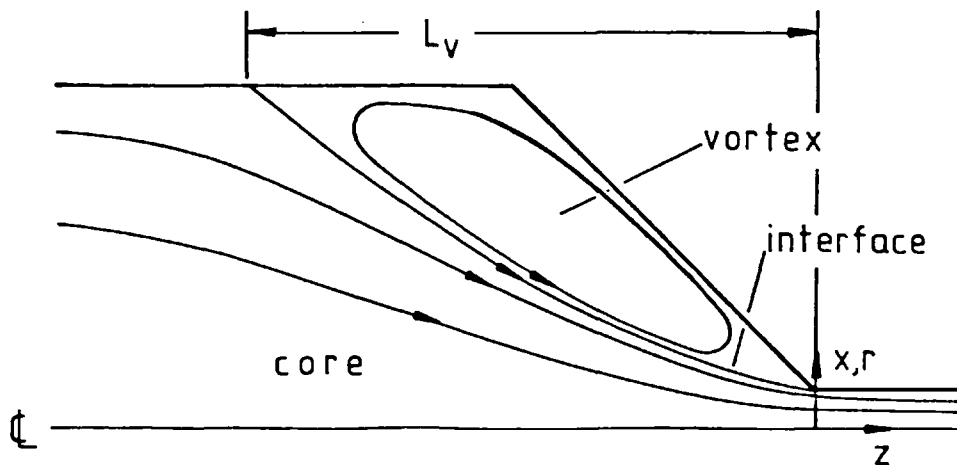main conclusions are summarised below.

Fig. 1.2 Schematic diagram of streamlines showing
         recirculating flow, either in 2D or
         axially symmetric geometry.

In a converging cylinder with $180°$ entrance angle, LDPE,

PS and PMMA exhibit vortices which for LDPE and PS increase in

size with increasing flow. The same behaviour is observed

for certain polymer solutions including polyisobutylene.

The melts HDPE, PP, PVC and polybutadiene exhibit no vortices.

The data on entrance angles other than 180°are scarce but for

LDPE, which displayed the largest vortices for the 180° case, no

vortices are observed for an entrance angle of 60° at all flow rates

below melt fracture [6]. In a converging wedge with a 180°

entrance angle, LDPE, PS exhibit vortices but the other melts

do not, certain solutions such as polyacrylamide do. LDPE exhibits

vortices for all entrance angles greater than 80°. In general,

for the melts and solutions which do not exhibit vortices, the

streamlines resemble the slow flow of a Newtonian fluid.

Other researchers such as Han and Drexler [7,8] have

observed no vortices occuring in wedge flow for PS, PP and HDPE.

For PS this contradicts the results of White and Kondo [5].

However, since Han and Drexler were primarily interested in

measuring the stresses developed, using a stress birefringence

technique, their flow rates necessarily could not be large, possibly

remaining below the rates required for the appearance of vortices.

Some of the results of their stress measurements are used in

Chapter 3 for comparison with theoretical predictions.

Pickup [9] has noted large vortices for wedge flow of a

Separan solution with entrance angles 2α, of 180° and 120°. Also

Strauss and Kinast [10] report a vortex flow with backflow along

the centreline for a polymer solution. This is a different type

from that normally observed and it may be due to inertial effects.

A number of workers have made measurements of

the velocity profiles in converging flow. Of particular interest

is the velocity of the interface between the recirculating vortex

and the core flow.   For both a cylindrical and wedge die

Metzner [11], Pearson and Pickup [12], and Cogswell [13] report

little variation in the velocity across the core region for both

melts and solutions.   In particular, Cogswell has found that the

boundary velocity is within 10% of the centreline velocity.   This

implies an almost irrotational flow situation in the core leading

to an almost extensional deformation regime.   Cogswell [14]

has attempted to capitalise on this fact, to produce a uniform

rate, extensional flow in the melt by using a specially shaped

tapered die-entry with lubricated walls.   The tapered region

has a shape similar to that of the core flow when vortices are

present.   However, this attempt does not yet appear to be

successful in producing reliable rheological data on stresses during

elongational flow.

Measurements of axial velocity profiles have also been

made for polymer solutions by Ramamurthy and McAdam [15] and

Cable and Boger [16,17,18], in the case of a cylindrical die-entry

and Tan and Tiu [19] for an annular die-entry.   Ramamurthy

and McAdam's work supports the conclusions above of an almost

flat axial velocity profile, however the other two report some

variation across the core region.   In fact, according to fig.6,7

of [17] and fig.7 of [18] as examples, the interface boundary

velocity is given as 0.   That this cannot be the case can immediately

be seen with reference to the photographs of the flow patterns.

Also on physical grounds, in the absence of stagnation points,

the only positions of zero velocity which may occur are at the centre

of the vortex region.

The centreline velocity $v_{z\ c.l}$ in the converging region

can be approximated quite well for a cylindrical die by a functional

relation of the form [17]

$$v_{z\ c.L.} = \alpha \exp\{-\beta^2 z^2\} \qquad\qquad (1.4)$$

where a cylindrical coordinate system is defined as in Fig. 1.2

with z = 0 being the position of the exit plane. For a wedge die

the form is similar [11]

$$v_{z\ c.L.} = \alpha \exp\{\ \beta z\} \qquad\qquad (1.5)$$

These formulae are only intended for $z\epsilon[-L,0]$, β is inversely

proportional to the length of the vortex region, L_v (see fig.1.2).

Finally, in a new initiative to understand the relative

influence of the shear thinning and the elastic properties of

viscoelastic fluids several research teams are experimenting

on the contraction flow of non-shear-thinning elastic polymer

solutions [20]. Large vortex regions are exhibited by these

solutions, though this does not mean that vortices are solely

attributable to elastic effects. Shear-thinning inelastic

solutions can also exhibit vortices [5]. However, by comparing

the deformation rates at the onset of vortex flow with measurements

of the shear modulus in simple shear of the polymer solution, Boger

concludes [20] that the occurrence of vortices "is associated with

deformation rate regions in which the normal stresses are not

quadratic (with shear rate)... or where the shear modulus is

deformation rate dependent". The relevance of this result to

theoretical studies of die-entry flow is that analyses based on

constitutive equations similar to the Upper Converted Maxwell

Fluid (UCMF), for which the normal stresses are quadratic and the

shear modulus is constant, will not give rise to large vortex regions [20]. It will be possible to comment further on this statement in Chapter 3.

1.3 Die-Entry Flow - Theoretical

Theoretical work on die-entry flow tends to be separated into analytic and numerical approaches. This thesis is an analytic study and is an attempt to extend the analytic approach to converging flow problems. For this reason, almost no consideration is given to the substantial developments in the numerical field. At present most analytic and numerical advances have been made for slightly elastic flows. By this is meant, that either the flow itself has a small Weissenberg or Deborah number or the constitutive equation used is for a slightly elastic fluid. It is to be hoped that analytic methods can be adapted to handle situations where Weissenberg numbers are of the order of magnitude of the example in section 1.1.

The normal procedure for obtaining solutions for converging cones or wedges is to idealise the geometry by considering

$$\frac{D_u}{D} \gg 1 \quad \text{for fixed entrance angle, } \alpha \quad \text{(see Fig.1.1)}$$

By doing this, the upstream and downstream boundary conditions are simplified. It is to be expected that solutions for finite regions can readily be obtained, once the asymptotic solution has been determined, by some sort of matching process, provided the relevant boundary conditions are known.

Solutions for converging channels

The exact solution for a Newtonian fluid in an infinite converging channel of half-angle α is well known for isothermal, incompressible flow and involves radial streamlines [21]. The velocity field in a polar coordinate system as in fig.1.3 is given by

$$v_r = - \frac{f(\theta)}{r} , \quad v_\theta = v_z = 0 \qquad (1.6)$$

where f is the solution of the mass conservation and dynamic equations

$$\nabla \cdot v = 0 \qquad (1.7)$$

$$\rho \frac{D}{Dt} v = - \nabla \cdot \pi \qquad (1.8)$$

which satisfies the no-slip boundary conditions on $\theta = \pm\alpha$. The momentum flux tensor π is defined as $\pi = \delta p - \mu(\nabla u + (\nabla u)^T)$
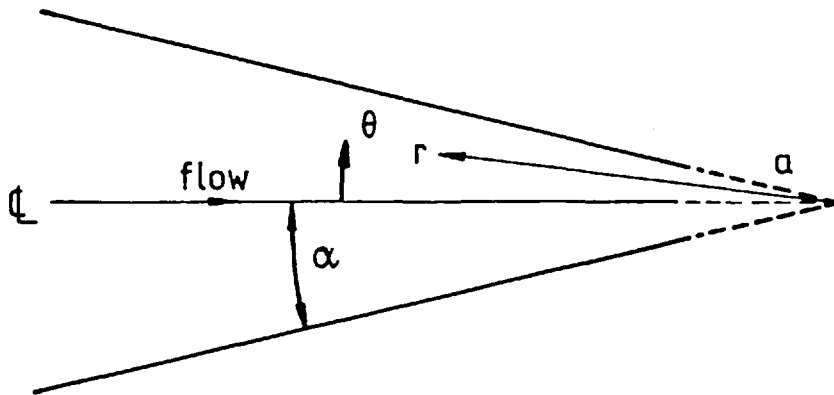

Fig. 1.3 Coordinate system for wedge flow.

For slow flow, f is given by

$$f = \frac{2Q(\cos 2\theta - \cos 2\alpha)}{\sin 2\alpha - 2\alpha \cos 2\alpha} \qquad (1.9)$$

in the asymptotic limit as $a \to 0$ where 2Q is the total flux per unit width. As noted by Moffatt and Duffy [22] there is a singularity for wedge angles of $2\alpha \approx 257.5°$, where the denominator in (1.2)

vanishes. They show further that for angles $2\alpha > 257.5°$, the inertia

terms in the dynamic equation (1.8) cannot be neglected, but for

$2\alpha < 257.5°$, it is valid to do so. In the latter instance a *local*

Reynolds number is defined as [22]

$$Re \sim (\rho Q/\mu)(a/r) \qquad (1.10)$$

which can be made initially small for any fixed r by letting $a \to 0$.

A solution for a power law fluid of the form of (1.6) has also

been obtained [8,23]. For viscoelastic fluids other than the

power-law, two approaches have been used to obtain solutions.

(i)   a perturbation expansion [24] in the Weissenberg

number $Ws = \dfrac{\lambda Q}{(a \sin\alpha)^2} = \dfrac{\lambda Q}{b^2}$ for wedges of

infinite upstream extent but with a finite down-

stream exit.

Characteristic length velocity and stress are defined as b, $\sqrt{Q/b}$,

$\mu Q/b^2$. The dimensionless velocity and stress fields v, τ, are

assumed to possess an expansion of the form

$$v = v_0 + Ws\, v_1 + (Ws)^2 v_2 + \dots$$
$$\tau = \tau_0 + Ws\, \tau_1 + (Ws)^2 \tau_2 + \dots \qquad (1.11)$$

valid for $Ws \ll 1$.

(ii) characteristic length, velocity and stress

are defined as $\sqrt{Q\lambda}$, $\sqrt{Q/\lambda}$, μ/λ.

A stream function is defined as the solution

to

$$v = \nabla \times (\psi e_z) \qquad (1.12)$$

where e_z is a unit vector in the z-direction.

A series expansion is assumed for ψ and τ of the form

$$\psi(r,\theta) = \sum_{n=0}^{\infty} \frac{\psi_n(\theta)}{r^n} \qquad (1.13)$$

$$\tau = \sum_{n=0}^{\infty} \frac{\tau_n(\theta)}{r^n} \qquad (1.14)$$

It can be shown that the two approaches are identical [24].

Solution of the first order terms gives the Newtonian result
(1.6, 1.9).

Perturbation or series solutions up to the second order
term have been obtained for the UCMF by [25,26]. The streamlines
for the flow which have been computed by Strauß are shown
approximately, in fig. 1.4 though as noted in [24] the region
of backflow is probably outside the validity of the procedure.
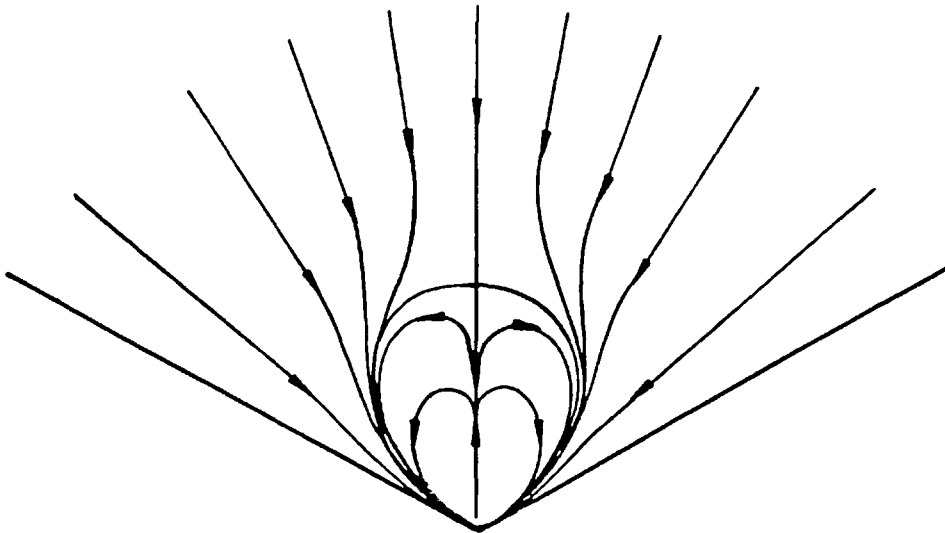

Fig. 1.4 Streamlines for slow flow of UCMF (Strauß [25]).

Neither Strauß nor Black give an indication of the error term
but it is claimed that the series converge, without adequate proof.

This matter is taken up in Chapter 3. The essential point, as far as later work in this thesis is concerned is that the streamlines close to the centreline as $r \to \infty$, diverge from the centreline as the origin is approached. This means that even if backflow does not occur, a relative deceleration of the fluid takes place along the centreline as $r \to 0$. In contrast to this, perturbation solutions obtained by Schümmer [27] for third and fourth order fluids show the reverse behaviour, streamlines converge towards the centreline as $r \to 0$.

Solutions for Flow in a Cone

A slow flow solution with radial streamlines exists for a Newtonian fluid and is due to Harrison [28]. The radial velocity is given by

$$v_r = \frac{3Q(\cos^2\alpha - \cos^2\theta)}{2\pi r^2(2\cos^3\alpha - 3\cos^2\alpha + 1)} \qquad (1.15)$$

and is valid for all angles α. When inertial effects are not negligible, vortices occur in the flow. A complete study of the series solutions is given by Ackerberg [29], who shows that there is backflow along the centreline in the neighbourhood of the origin.

For viscoelastic materials a perturbation solution has been obtained for a third order fluid [5]. The streamlines behave in a fashion similar to Schümmer's solution for the wedge with a concentration of flow along the centreline as $r \to 0$.

Extensional Primary Field

A different approach to the analysis of converging flow

has been suggested in two, apparently independent papers [12,30].

It relies upon the experimental measurements of the velocity field,

both in the presence and absence of recirculating vortices, which

show that a substantial proportion of flow field (see fig.1.5)

may be approximated by an elongational flow [11-14]. Metzner [30]

considers a local sink flow for a core, whereas Pearson and Pickup

[12] prefer a local pure shear flow for a wedge.
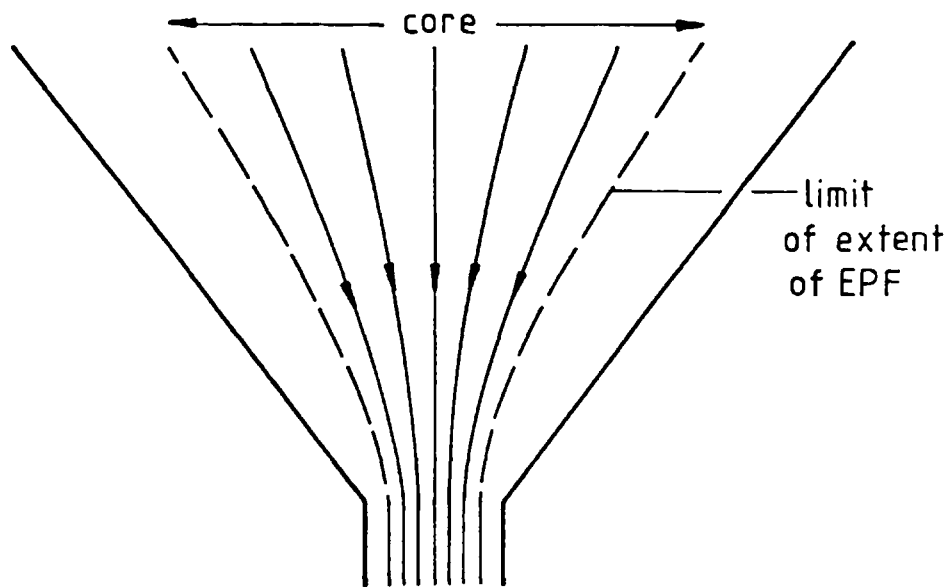

Fig.1.5 Die-entry showing streamlines for core region.

Further experimental justification for assuming that the core region

may be approximated by an elongational flow, is afforded by the high

values of the Trouton ratio N_{T_r} exhibited by many polymer solutions

and melts [11], where N_{T_r} is defined as the ratio of viscosity in

uniaxial extension and in simple shear

$$N_{T_r} = \frac{\eta_{el}}{\eta_{sh}} = \frac{(\tau_{11}-\tau_{22})/\frac{\partial v_1}{\partial x_1}}{\tau_{12}/\frac{\partial v_1}{\partial x_2}} , \quad at \left|\frac{\partial v_1}{\partial x_1}\right| = \left|\frac{\partial v_1}{\partial x_2}\right|$$

$$(1.16)$$

Typical reported values for polymer solutions are in excess of 100, whereas for LDPE, $N_{T_r} \approx 25$ for deformation rates $7 \times 10^{-2}-10$ s^{-1} [31]. In addition, Metzner [30] notes that the ratio of the primary normal stress difference to the shear stress in simple shear can be large at high deformation rates. The Extensional Primary Field (EPF) approximation follows and merely involves diagonalising the stress tensor, τ

$$\tau = \begin{pmatrix} \tau_{11} & [0] & [0] \\ [0] & \tau_{22} & [0] \\ [0] & [0] & \tau_{33} \end{pmatrix}$$

$$(1.17)$$

by neglecting the shear stress τ_{12}, τ_{13}, τ_{23}. Of course, τ must be defined relative to some non-rotating coordinate system. This approximation method has subsequently been used by Cogswell [14], Winter et. al. [32] and Pearson and Trottnow [33].

The major outstanding mathematical problem is how to treat the remainder of the flow region, in particular so that the no-slip boundary conditions can be fulfilled. This matter will be dealt with in Chapter 4.

The outstanding experimental requirement is for a comparison of stresses in melts undergoing uniaxial extension and simple shear deformations at extension rates typically involved in die-entry flows. Referring to the grossly simplified example in section 1.1,

data is needed for extension rates at least up to 100 s^{-1}. Laun

and Münstedt[31] report data for LDPE up to 10 s^{-1}, Ide and White

[34] up to 1.5s^{-1} for PS: these appear to be the highest rates

in the literature. The time-temperature superposition principle

could be used to effectively extend the rate range of the existing

machines, but this has not be done. Data presented in Chapter 2

shows the form which the principle takes for start-up flows in

uniaxial extension and simple shear. Stevenson [35] gives data

for a polyisobutylene-isoprene copolymer (Butyl 035) up to .05s^{-1}

with a Trouton ratio, at this rate, of 5. This rubber is investi-

gated in Chapter 2. Because of the lack of data and also for its

own sake, two rubber compounds are investigated in Chapter 2, principally

to determine the stresses involved in uniaxial extension at high

rates and to compare them with the shear stresses in simple shear.

CHAPTER 2
ASPECTS OF
RUBBER RHEOLOGY

The measurement of the rheological properties of polymer melts like rubber has a large number of diverse aspects which perhaps can be separated into two groups, each with different objectives. One objective is to obtain data which are directly relevant to the modelling of complex flows which occur in polymer engineering and the other is for data which are critical for a deeper appreciation of the molecular structure and behaviour of melts. Although in this chapter experimental results are presented which fit both objectives, they will be used only for the first in later chapters.

The data have been obtained using two recently constructed machines at an Avon Rubber Co. research laboratory. The first of these is a double cone and plate device which will be referred to as the T.M.S. Rheometer after their designers, Turner, Moore and Smith. It is specially appropriate for use with rubbers (unvulcanised) rather than plastics or polymer solutions and derives much from the Standard Mooney Viscometer. The second device, also designed by Avon Rubber Co. in collaboration with Dr J. Funt, then of

Imperial College, London, is a constant strain rate elongation rheometer
(E.R) which deforms rubber in a uniaxial extension at high rates;
up to about 100 s^{-1}. This enables stress measurements to be made
in a regime which corresponds with elongational strain rates observed
in typical melt flows through converging channels and tubes.

Since the machines are recent innovations they are described
in detail. Particular emphasis is placed on comparing their per-
formance with other similar 'established' machines, although in
the case of the Elongation Rheometer this proved difficult since
the operating range is presently higher than any yet reported in
the literature. The main results, presented in section 2.4 are
those of viscosity and stress growth in the start-up of simple
shear and uniaxial extension.

A major preoccupation in obtaining the experimental
measurements was to ensure that the rubber did not slip on the solid
surfaces of the rheometers. In sections 2.3 and 2.5 it is demonstrated
that the attempt was largely successful. This was achieved by a
careful choice of rubber compounds used in the experiments. However,
for rubber compounds which exhibit a large degree of slip, some
correlation of the data for steady shear flows was possible using
a simple model of the slip mechanism.

Finally section 2.6 is devoted to fitting the experimental
data to some simple viscoelastic constitutive equations. As the
equations are unsophisticated an excellent fit is not expected, but
it should be possible to describe the behaviour of the rubber compounds
at least semi-quantitively.

2.1   T.M.S. Rheometer

The T.M.S. Rheometer is described in Turner and Moore [36].
The relevant passage is quoted here in full.

"The basic configuration of the Mooney

viscometer has advantages in rheological

testing. The sample has a geometry set by

the cavity and rotor and the sample can be

conditioned by shear, prior to measurements

to eliminate thixotropic effects. It has

a heavily serrated rotor to eliminate wall

slip, but in most processing situations the

interaction between rubber and smooth surfaces

is more relevant. To have reproducible results

in such situations it is necessary to have a

fresh rubber surface coming into contact with

the rotor and to be able to control pressure.

The procedure adopted was therefore one used

for making precision rubber mouldings in the

factory. A transfer system was built on top

of the Mooney cavity, according to the layout

in Fig. 2.1.

This has the following advantages:

(i)   The pressure in the cavity is controlled by the force
applied to the injection ram.

(ii)   Fresh rubber surfaces make contact with the rotor and the
cavity.

(iii)   The cavity is always closed during filling and maintains precise dimensions.

(iv)   A single cylindrical blank is required so results are hardly influenced by operator skill

(v)   Pre-warming in the transfer chamber followed by injection enables a uniform temperature to be established more rapidly.

Three rotors were obtained for the machine:

(a)   With 48 radial grooves on each face according to Fig. 2.2

(b)   Ungrooved ground surface (Rockwell C. Min 60)

(c)   Polished surface.

The faces of the rotor are biconical with an angle of 6° 40' giving a shear rate of 0.895 reciprocal seconds at 1 rev/min. The clearance between the outer circumference of the rotor and the walls of the cavity provides the same shear rate. The cavity is the standard Mooney cavity with heavy grooving. This particular machine is fitted with a variable speed motor and a gearbox giving a rotor speed range of 0.2 to 40 rev/min. It also has the capability of measuring recovery, stress relaxation and stress development during start-up."
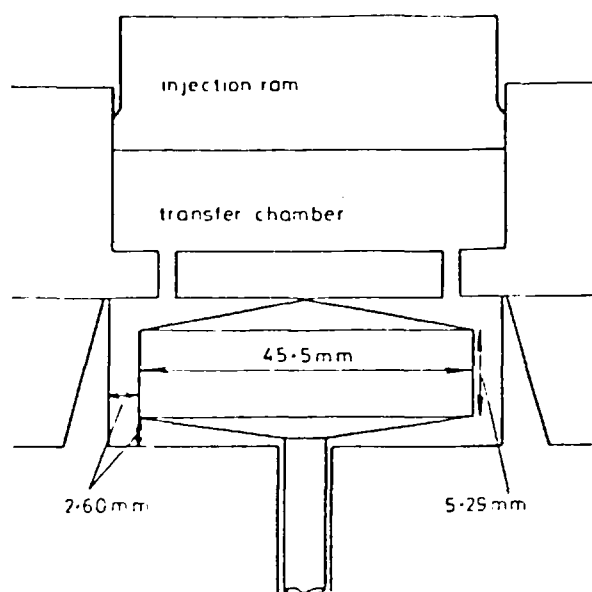
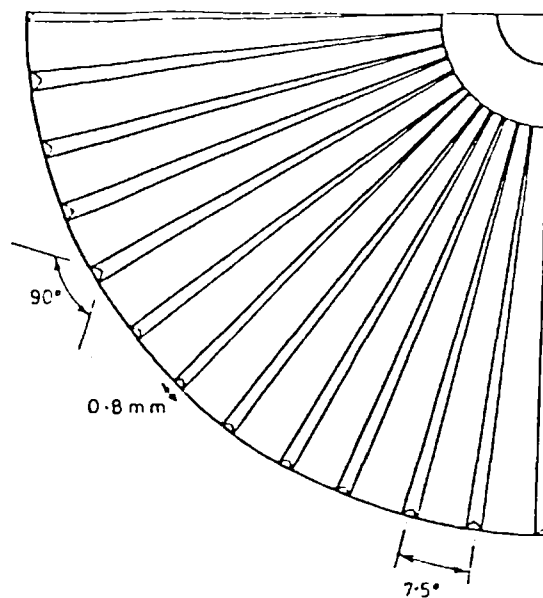Fig. 2.1 Layout of transfer chamber, rotor and test cavity

Fig. 2.2 Grooved rotor

To derive an expression for the shear stress component in a rubber sample in the T.M.S. Rheometer, the assumption is made that the cavity can be considered to be composed of three separate regions of flow as indicated in Fig. 2.3:

(i)   a cone and plate flow, region A , shear stress $\tau_{\phi\psi}$

(ii)   a couette flow, region B, shear stress $\tau_{r\theta}$

(iii)   a 'dead' volume, region C, which is supposed to have no effect on the flow.

It is assumed that there is no slip of the rubber on the surfaces of the cavity and rotor. The shear stress, $\tau_{\phi\psi}$, in region A is approximately constant since the cone angle α is sufficiently small, see Walters [37]. In region B there is a variation in the shear stress, $\tau_{r\theta}$, of up to 20%. However, the contribution of B to the torque on the rotor is small compared to
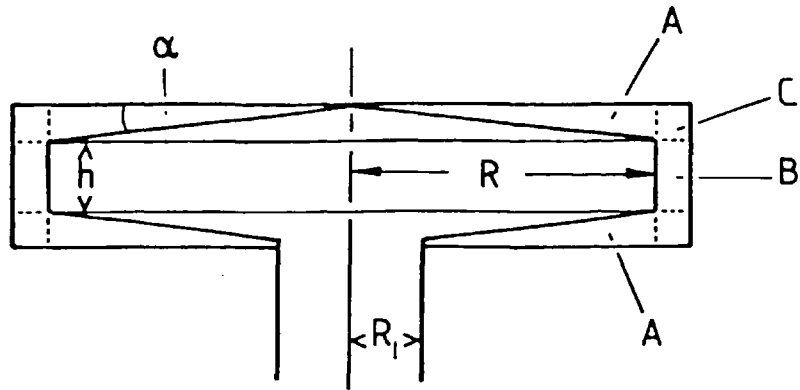
	Cavity + Rotor 1	Cavity + Rotor 2	
R =	22.7	22.0	(mm)
h =	5.29	1.60	(mm)
R_1 =	5.16	5.16	(mm)
α =	6.67	6.00	(degrees)

Fig. 2.3 Cavity and rotor of T.M.S. showing dimensions
and flow subdivision into regions A,B,C.

that from A.   It is expected that only a small error will result
from taking $\tau_{r\theta}$ as constant.   This is particularly the case for
cavity and rotor (2) which was modified specifically to reduce the
couette flow contribution.   The cavity and rotor geometry is such
that the shear stress is the same over the whole of the rotor
surface, $\tau_{r\theta} = \tau_{\phi\psi}$, and is given in terms of the torque T, by

$$\tau_{r\theta} = \frac{3T}{2\pi(2R^3 - R_1^3 + 3R^2 h)} \qquad (2.1)$$

The detailed calculation is given in Appendix 1.

2.2   Elongation Rheometer

The drive and clutch mechanism and heating arrangement

of the elongation rheometer is drawn schematically in Fig. 2.4, and

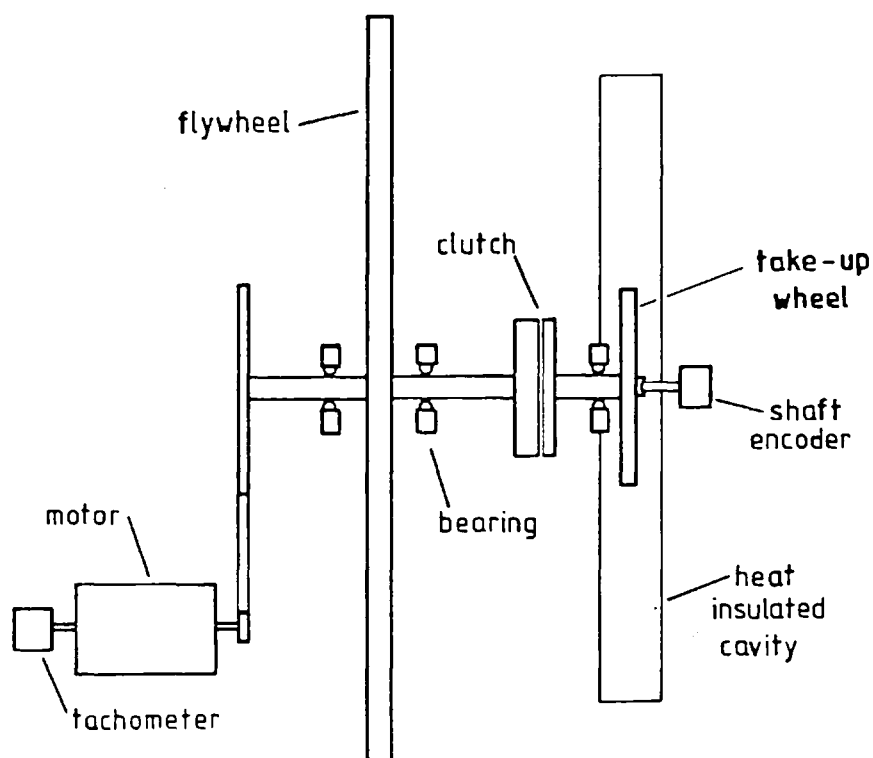has been considerably simplified for clarity.

Fig. 2.4   Mechanism of the Elongation Rheometer,
with position of heat insulated cavity
indicated.

Before the start of a test, the electromagnetic clutch is disengaged

and the flywheel rotates at a fixed angular velocity as controlled

by the motor and tachometer. At the appropriate moment, the clutch

is engaged causing the rotation of the take-up wheel, which, being of

low moment of inertia compared to the flywheel, assumes the same

angular velocity almost instantaneously. The sample is completely

encased in the heat insulated cavity which is maintained at a fixed

temperature by a hot air blower.   The temperature variation near

the inserted sample is $\pm 0.5°C$ over a range of temperatures $20-140°C$.

A sample is loaded by attaching it to the take-up wheel,

passing it round the small grooved wheel fixed to the transducer

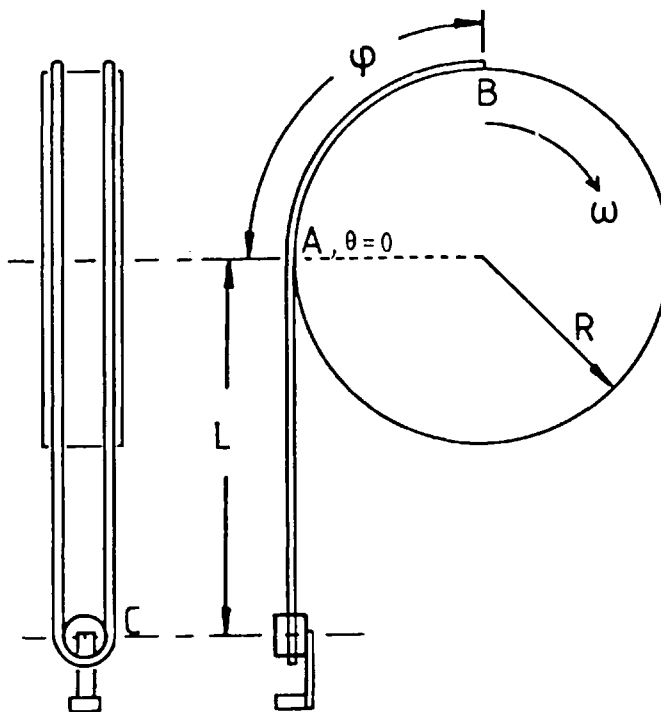and securing it again on the take-up wheel, see Fig. 2.5.

Fig. 2.5 Take-up wheel, side and end views, showing
initial position of rubber filament

This double cord arrangement has the advantage over a

single cord as it avoids high stress concentrations at the lower fixed

end. Observation of filaments at the relatively low extension rates

of about 1 s^{-1} confirm that it fails most frequently between points

A and C and that it deforms uniformly along its free length prior to

breaking. At higher rates of extension the deformation of the filament

is assumed to be uniform on the basis of experimental work by Connelly,

Garfield and Pearson [38]. They show that for a material with a

maximum relaxation time λ_{max}, uniform deformation occurs for extension

rates $\dot{\epsilon}$, such that $\dot{\epsilon}\lambda_{max} \gg 1$. Since the filament deformation was

observed to be uniform at rates of about 1 s^{-1}, it is reasonable to

expect it to be uniform at higher rates.

For the filament extension to occur at a constant rate it is required that

(i) the filament does not slip once it has made

contact with the take-up wheel

(ii) there is no slip where the filament is attached

to the transducer, point C

(iii) there is only a negligible change in the angular

velocity of the flywheel during the experiment.

The validity of (i) and (ii) is examined in later sections both theoretically and experimentally. The total change in the angular velocity of the flywheel can be calculated using the conservation of energy. Let 2D be the work done due to the couple exerted on the take-up wheel by the two strands of the filament. Let $I_F = 1.35$ kg m^2 be the moment of inertia of the flywheel. Neglecting the inertia of the take-up wheel and the filament, it can easily be shown that the ratio of the final to the initial angular velocity of the flywheel ω_f/ω_i is given by

$$1 \geq \frac{\omega_f}{\omega_i} = \{1 - \frac{2D}{\omega_i^2 I_F}\}^{\frac{1}{2}} \qquad (2.2)$$

A lower bound is required for ω_f/ω_i, which will occur at the lowest temperature and angular velocity used in the experiments. At 60°C and with $\omega_i = 7s^{-1}$ (corresponding to an extension rate of 3.5s^{-1}) experimental results give $D \approx 0.043$Nm. Evaluating (2.2) for this value of D gives $\omega_f/\omega_i = 0.9994$, which is the lower bound. So (iii) is valid throughout the operating range. Thus the filament is deformed at constant rate $\dot{\epsilon}$

$$\dot{\epsilon} = \frac{\omega R}{L} = \frac{\omega}{2} \qquad\qquad (2.3)$$

where ω is the angular velocity of the take-up wheel and R and L

are as in Fig. 2.5. The machine is presently capable of $\dot{\epsilon}$ in

the range 1-110 s^{-1}.

Samples are prepared by extruding a filament of circular

cross-section, about 3mm in diameter, at $100°C$. The filament is

allowed to relax in an oven at $90°C$ for 75 minutes. It is cut into

equal lengths and weighed. An average weight over all samples is

calculated and any falling outside 5% of the mean are rejected.

After securing in the apparatus, the samples are allowed about 3

minutes, depending on the filament thickness, to reach an equilibrium

temperature. This time was confirmed to be sufficient experimentally.

Measurements are made during testing by recording the

value of the force from the piezo-electric transducer at equal

increments of rotation of the take-up wheel as determined by the

shaft encoder. The Reynolds number for the flow is given by

$$Re = \frac{\rho L U}{\mu} = 0(10^{-3}) \qquad\qquad (2.4)$$

for rubbers with density $\rho = 0(10^{3})kgm^{-3}$, viscosity $\mu = 0(10^{6})N\ sm^{-2}$,

at the highest extension rate $\dot{\epsilon} = 0(10^{2})s^{-1}$. Since this is small

it can be shown that the stress is independent of position throughout

the free length of the filament. Allowance must be made for the

expansion of the rubber at elevated temperatures, for an increase

both in the cross-sectional area and the free length of filament $\overline{AC}$.

The first affects the stress, the second results in a small additional

length which must first be taken up before the sample is actually

elongated. The necessary corrections are easily made on the

basis of a linear expansion coefficient, e, temperature difference ΔT.

The stress $\tau_{zz}-\tau_{rr}$ is then given in terms of the force F on the

transducer by

$$(\tau_{zz}-\tau_{rr})(t) = \frac{F(t)}{2A_o(1+\Delta Te)^2\exp(-\dot{\epsilon}t)} \qquad (2.5)$$

where A_0 is the initial cross-sectional area and t is the time from

which the filament becomes taut.

2.3   Difficulties Encountered with Rubber Testing

Before presenting the experimental results, it is necessary

to discuss in detail some of the practical difficulties arising during

the tests.   In some respects many of these were previously recognised

by Mooney [39], in particular that of irregular melt flow of

rubber in a cone-and-plate device.   In an experiment using two

colours of rubber in the cavity he observed globules of rubber

which were formed at high shear rates instead of the laminar spirals

observed at lower rates. He refers to the globules as 'rheological

units'.   The same behaviour is observed in the T.M.S. Rheometer.

Other difficulties more peculiar to the work here are considered

under three headings:

      (i)   inhomogeneities in sample and material

      (ii) ageing of rubber stocks

      (iii) slip between rubber and solid surfaces.

Each of these is discussed separately in what follows.

(i)   Inhomogeneity of sample

The inhomogeneities considered here apply to compounded rubbers in particular.   The molecular weight distribution of the polymer is not considered since it is not expected that this varies during the tests except when the rubber is subjected to milling, and to a slight extent, extrusion. The main concern is with the heterogeneous dispersion of carbon black and oil in the rubber compound and the possible introduction of air bubbles whilst extruding samples for the Elongation Rheometer.

The first of these does not apply to gum rubbers but otherwise arises as the result of any mixing process. The effect of shearing deformation on the compounds in the testing machines is to generate further mixing and better dispersion of filler and oil in the material and generally leads to a lower viscosity. This is unavoidable, but can be kept to a minimum throughout the duration of an experiment on the T.M.S. Rheometer by frequent changes of rubber sample and by taking care not to deform the sample excessively during testing. A check is always made on the sample that its properties before and after testing are sufficiently similar; e.g. that a recording of steady shear stress does not vary by more than 0.5% between independent measurements. Shearing deformation is also present during production of samples for the Elongation Rheometer. However, it was suspected that this had a negligible effect, at least on the shear properties.   This was confirmed using a Butyl rubber compound by measuring flow curves of two samples: one of the samples was first extruded as for the production of filaments for the Elongation Rheometer, the other had no prior treatment. That which was extruded showed a lower viscosity of about 0.5%.

Unfortunately one of the compounds used, a Chloroprene

rubber is more prone to rheological change during testing than

the others. This possibly represents a high degree of inhomogeneity

in the material as it comes off the mill. It may also reflect a

thixotropic effect. By subjecting the Chloroprene compound to

a large amount of shear work prior to testing, its rheology becomes

more constant. However, the sheared compound less closely resembles

the material involved on the production line but it should be possible

to account for the errors introduced by this process if necessary.

The second inhomogeneity in the samples, that of air bubbles, is

easily detected by a close examination of the extrudate for irregu-

larities in the surface which are then immediately excised.

(ii)   Ageing of rubber stocks

Unvulcanised rubber compounds undergo considerable rheological

changes over large intervals of time particularly if they contain

a curing system. Normally, this leads to higher viscosities as a

result of cross-linking between polymer chains. The effect can be

reduced by storing the compounds at low temperatures. However, it is

found for compounds which do not contain curing systems that changes

still occur; in the case of a butyl compound the viscosity decreased

with storage time, even though the storage temperature was $-1°C$. This

is attributed to a dispersion of the oil, which is still mobile

at such temperatures, more homgeneously throughout the rubber stock.

The effects are unavoidable within the constraints of the laboratory

and requires that all experiments on a particular compound are

completed over the period of about one month.

(iii)   Slip between rubber and solid surfaces

The possibility of 'wall slip' occurring between rubber

and solid surfaces in the T.M.S. Rheometer has been established

by Turner and Moore [36] but was expected through the experience

of Mooney [39]. The degree of wall slip depends both on the rubber

compound and the physical nature of the solid surface. The phenomenon

is demonstrated by measuring the torque on different types of rotor

surface; for example, polished, smooth, or grooved; at various rotor

speeds (see Fig. 3 of Turner and Moore [36]). Although a number

of mechanisms have been proposed for the slip effect they are not

the main concern here. However, in the presence of wall slip, no

reliable measurements can be made of stresses in shear flow.   It is

held that no slip occurs on the grooved rotor, and that it is

suitable for rheological measurements.   This assertion requires

justification.

After tests on a number of compounds it was discovered

that the chloroprene compound and raw gum Butyl displayed no detectable

difference between measurements made with the polished and grooved rotors. These

are important conclusions which justify the use of the grooved rotor

in rheological measurements which require the no-slip boundary condition

on solid surfaces to be satisfied.

It is expected that slip also occurs in the operation of

the Elongation Rheometer between the rubber filament and the take-up

which, as noted in section 2.2.   Before any meaningful results can

be obtained from the E.R. it is essential to determine the likely

extent of the slip.   An experimental study of the problem is presented

in section 2.5.   A theoretical analysis is conducted in what follows.

When an elastomer slides over another surface it is possible

that no true sliding takes place [40]; rather, relative motion may proceed

through Schallamach waves. In order to make an estimate of the

frictional force two possibilities are examined. The first is to

apply the work of Grosch [41] who conducted sliding experiments

on various rubbers including Butyl. He measured a friction factor

μ, defined by

$$\mu = \frac{\text{Tangential or Frictional Force}}{\text{Normal Force}} = \frac{F}{N} \qquad (2.6)$$

for a flat block of vulcanised rubber sliding over a variety of

surfaces at various speeds and temperatures. Measurements showed that

μ was essentially load independent up to a normal pressure of 5.4kN m^{-2}.

Typical results from Grosch for a Butyl compound containing 50pph

of carbon black sliding over a clean abrasive surface show that

μ lies between 1.0 - 2.5. However, this is not completely satisfactory

because in the Elongation Rheometer a filament of rubber is used,

not a block as used by Grosch. Also, if Schallamach waves are

formed in the filament, then the frictional force depends on the true

area of contact A. The second possibility is to consider the

frictional force, F, to depend on a mean frictional stress, S,

approximately constant for a particular compound, as in Briggs and

Briscoe [40]

$$F = AS \qquad (2.7)$$

The area of contact A, is determined by solving the Hertz equation

and is given in Bowden and Tabor [42] by

$$A = 2L \left(\frac{4}{\pi} Wr \left(\frac{1-\nu^2}{E} \right) \right)^{\frac{1}{2}} \qquad (2.8)$$

where L is the contact length, r the filament radius, Young's Modulus

for Butyl rubber $E = 10^6 \text{ N m}^{-2}$ [43], and $\nu = \frac{1}{2}$ is Poisson's ratio.

The load per unit length W, is given in terms of the tension T, and stress by

$$W = \frac{T}{R} = - \pi \left(\frac{\tau_{zz} - \tau_{rr}}{R}\right) r^2 \qquad (2.9)$$

in which R is the take-up wheel radius, $R = 5 \times 10^{-2}$ m. Thus the friction factor μ, as in (2.6) is

$$\mu = \frac{AS}{Td\theta} = \frac{4RS}{\pi} \left(\frac{1-\nu^2}{-(\tau_{zz} - \tau_{rr}) ErR}\right)^{\frac{1}{2}} \qquad (2.10)$$

$$= 2.5 \times 10^{-4} \, S[-r(\tau_{zz} - \tau_{rr})]^{-\frac{1}{2}} \qquad (2.11)$$

in which $d\theta$ is a differential element of angle (see Fig. 2.6).

The minimum value of μ coincides with the maximum value of $-r(\tau_{zz} - \tau_{rr})$. It is now necessary to anticipate the experimental results of the next section, and progress can only be made if the effect of slip is small; an assumption which will be confirmed, afterwards. Referring to fig. 2.14 it is clear that the required maximum is attained at the limit of upward sweeping curves, i.e. close to the maximum of the elongation stress. As an example take the curve for $\dot{\epsilon} = 105.0 \, s^{-1}$. At time $t = 5 \times 10^{-2}$ s, $\tau_{zz} - \tau_{rr} = -\eta^+ \dot{\epsilon} = -10^8 N \, m^{-2}$ where η^+ is the stress growth function. The filament radius, for an initial radius of $r_o = 1.5 \times 10^{-3}$ m, is

$$r = r_o \, e^{-\dot{\epsilon}t/2}$$

$$= 10^{-4} \, m$$

Thus $\mu_{min} = 2.5 \times 10^{-6}$ S. Similarly a maximum value for μ can be calculated from data in Fig. 2.14 and is $\mu_{max} = 2 \times 10^{-4}$ S. This is a large variation of two orders of magnitude. The least certain of

the two values is μ_{min} since the filament radius is small and the

frictional forces of such fine filaments is not well known.

Values for S are given in Briggs and Briscoe [40]. For

Butyl rubber $S = 2\times10^5 N\ m^{-2}$, and for Chloroprene $S = 7\times10^5 N\ m^{-2}$,

so the estimates for μ lie between 0.5 - 40 for Butyl, somewhat

higher for Chloroprene. This range is somewhat extreme, the

experimental work of section 2.4 may clarify which value should be

chosen. It must be added that the measurements of S and μ for rubber

compounds of the type used here, are for vulcanised samples. Perhaps

understandably, there does not seem to be any data for unvulcanised

rubbers. It is not clear what effect vulcanisation has on the mean

frictional stress and the friction factor but the values quoted

should give a reasonable measure of their orders of magnitude.

Consider now the mechanics of a rubber filament moving

over a solid surface subject to a frictional force which will be taken

as proportional to the load. It is required to solve the conservation

of mass and stress equilibrium equations. However, because the body

force on the filament is not immediately obtainable, a force balance

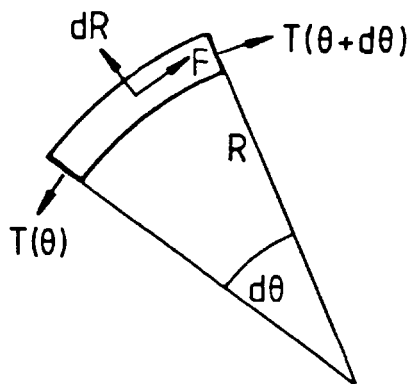is taken on a small section of the filament; see Fig. 2.6

Fig. 2.6 Diagram showing forces on an element of
the rubber filament situated on the take-up
wheel.

$$T(\theta+d\theta) - T(\theta) + F = 0 \qquad (2.12)$$

$$T(\theta)d\theta - dR = 0 \qquad (2.12)$$

Provided slip occurs $F = \mu dR$ and

$$\frac{\partial T}{\partial \theta} + \mu T = 0 \qquad (2.14)$$

This is the familiar capstan problem [44] which has the following

solution for the engineering stress σ;

$$\sigma = \frac{T}{A_o} = \sigma_o(t)e^{-\mu\theta} , \quad A_o \text{ the initial filament}$$
cross-sectional area.

$$(2.15)$$

If slip does not occur then the frictional force F in (2.12)

is unknown. This problem will be dealt with when it arises. The

stress equilibrium equation for the free length of filament, whose

parameters are designated by $\hat{}$, merely implies

$$\hat{\sigma} = \sigma_o(t) \qquad (2.16)$$

where continuity of tension is satisfied at $\theta = 0$, A in Fig. 2.5.

The mass conservation equation relating extension γ and

velocity U may be written as [45]

$$\gamma = A_o/A \qquad (2.17)$$

$$\left(\frac{1}{\gamma}\right)_t + \frac{1}{R}\left(\frac{u}{\gamma}\right)_\theta = 0 \quad \text{on take-up wheel} \qquad (2.18)$$

$$\left(\frac{1}{\hat{\gamma}}\right)_t + \frac{\hat{u}_z}{\hat{\gamma}} = 0 \quad \text{on free length} \qquad (2.19)$$

in which the velocity is in one direction only i.e. u is the θ

component and $\hat{u}$ is the z component. The subscripts denote

differentiation. The boundary conditions are continity of velocity

and extension at $\theta = 0$ and two fixed ends (2.20-23). The initial

conditions are that the extension is unity (2.24) and no slip

occurs on take-up wheel, at time $t = 0$, (2.25).

$$\hat{u}(L,t) = u(0,t) \tag{2.20}$$

$$\hat{\gamma}(t) = \gamma(0,t) \tag{2.21}$$

$$u(\omega t + \phi, t) = \omega R \tag{2.22}$$

$$\hat{u}(0,t) = 0 \tag{2.23}$$

$$\hat{\gamma}(0) = \gamma(\theta,0) = 1 \tag{2.24}$$

$$u(\theta,0) = \omega R \tag{2.25}$$

Slip does not occur initially for two physical reasons:

(i) At elevated temperatures there is always

some slack in the free filament

(ii) Even under conditions of no load, there is

a small adhesive force between rubber

and solid surface.

However, because of the mathematical approximations already made,

in this case, the assumption of slow flow, this last condition (2.25)

will not generally be satisfiable. This is however of only minor

importance; but it is discussed in Appendix 2.

It remains to specify a constitutive equation. Before

this is done, a measure of the elastic effects present in the flow

are afforded by calculating the Deborah Number, De,

$$De = \frac{\text{Characteristic time of fluid}}{\text{Characteristic duration of flow}} = \frac{\lambda \dot{\epsilon}}{\ln \gamma_{max}}$$

$$\tag{2.26}$$

Typical values of $\lambda, \dot{\epsilon}$ and the maximum Hencky strain $\ell n \; \gamma_{max}$ are

$\lambda = 12.5s$, $\dot{\epsilon} = 50s^{-1}$, $\ell n \; \gamma_{max} = 5$: thus $De = 0(10^2)$.

Because of the high value of De, it is expected that an

elastic constitutive equation is appropriate. This is carried out

in what follows.

The constitutive equation for a general elastic solid

may be written

$$\sigma = \sigma(\gamma) \tag{2.27}$$

Using (2.15) and (2.27) the mass conservation equations (2.18-19)

can be integrated to obtain expressions for the velocity

$$\hat{u} = z \; \frac{\hat{\gamma}_t}{\hat{\gamma}} \tag{2.28}$$

$$u = \frac{R}{\mu} \; \frac{\dot{\sigma}_o}{\sigma_o} + \gamma\psi(t) \tag{2.29}$$

for some function ψ satisfying the kinematic condition (2.22).

Differentiation with respect to time, t, is denoted by $\dot{\;}$. Satisfying

(2.22) yields

$$u = \frac{R}{\mu} \; \frac{\dot{\sigma}_o}{\sigma_o} + \frac{\gamma(\theta,t)}{\gamma(\omega t + \phi, t)} \{\omega R - \frac{R}{\mu} \; \frac{\dot{\sigma}_o}{\sigma_o}\} \tag{2.30}$$

Satisfying continity of γ, u and $\hat{\gamma}, \hat{u}$ at $\theta = 0$, $z = L$ (2.20-21) yields

a differential equation for σ_o:

$$\frac{\gamma_t}{\gamma}\bigg|_{\theta = 0} = \frac{R\dot{\sigma}_o}{L\mu\sigma_o} + \frac{\gamma(0,t)}{\gamma(\omega t + \phi, t)} \{\dot{\epsilon} - \frac{R\dot{\sigma}_o}{L\mu\sigma_o}\} \tag{2.31}$$

in which use has been made of $\dot{\epsilon} = \omega R/L$. Slip ceases when

$$u = \omega R = \left. \frac{L\gamma_t}{\gamma} \right|_{\theta = 0} \tag{2.32}$$

that is when

$$\left. \frac{\gamma_t}{\gamma} \right|_{\theta = 0} = \dot{\epsilon} \tag{2.33}$$

From (2.30) and (2.31) it can be seen that (2.33) is satisfied when

$$\frac{R\dot{\sigma}_o}{L\mu\sigma_o} = \dot{\epsilon} \tag{2.34}$$

and that slip ceases simultaneously for all θ.

A typical plot of experimental measurements of σ_o against time for Butyl CI is shown in Fig. 2.7. Only the initial part of the curve is included but it shows the extent of the elastic part of the flow, up to the maximum in σ_0. Thereafter viscous effects are strictly not negligible.

From the graph and equation (2.34) it is readily shown for example, that slip ceases after a time $t = 3 \times 10^{-3}$s if μ is taken as unity. This point is marked in Fig. 2.7 and it lies well within the elastic regime. Since the total strain achieved in the experiment was about 8 only a small part of the experiment involves slip, provided once slip ceases it does not recur. This is now considered.
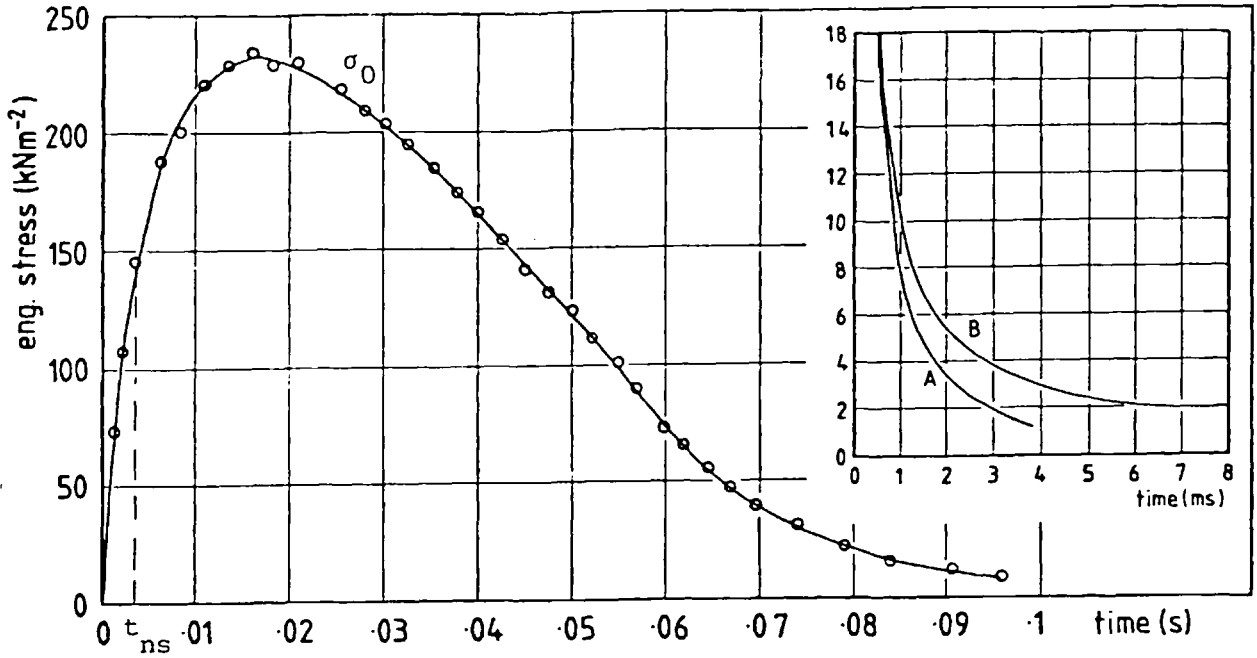
Fig. 2.7 Engineering stress against time for Butyl CI
compound; extension rate 105 s^{-1} at 100°C.
Cessation of slip occurs for $\mu=1$ at $t=t_{ns}$.
Also shown is a plot of $\dot{\sigma}_0/(\sigma_0\dot{\epsilon})$ as a function
of time, curve A and the time to no slip as a function
of μ for a linear elastic solid, curve B.

Intuitively, for an elastic solid, the tension is constant following
a solid particle. Mathematically this is expressed as

$$\frac{\partial\sigma}{\partial t} + \omega\frac{\partial\sigma}{\partial\theta} = 0 \qquad (2.35)$$

with the solution

$$\sigma = \sigma_0(t-\theta/\omega) \qquad \text{for } t-\theta/\omega \geq t_{ns} \qquad (2.36)$$

$$= \sigma_0(t_{ns})e^{-\mu(\theta-\omega(t-t_{ns}))} \qquad \text{for } t-\theta/\omega < t_{ns} \qquad (2.37)$$

where t_{ns} is the time when slip ceases and σ_0 has the same meaning
as in (2.15). Slip does not recur if

$$-\frac{\partial\sigma}{\partial\theta} \leq \mu\sigma \qquad (2.38)$$

which is equivalent to $\qquad \dfrac{\dot{\sigma}_0}{\sigma_0} \leq \dfrac{L\mu\dot{\epsilon}}{R} \qquad (2.39)$

Since $\overset{\bullet}{\sigma}$ is a decreasing function of t within the elastic regime (see Fig. 2.7), the no slip condition (2.39) is clearly satisfied. It can also be shown (see Appendix 2) that for a viscoelastic fluid with relaxation time λ, slip does not occur when viscous effects become important if

$$\frac{L\epsilon}{R} \lambda\mu \geq 1 \qquad\qquad (2.40)$$

This is a sufficient condition only. Because of the high relaxation time of rubbers and the high extension rates used in the experiment this relation is satisfied.

To calculate the time to cessation of slip theoretically, it is necessary to assume a specific form of the constitutive equation (2.27). For strains close to unity, elastic behaviour is suitably modelled by the equation [46]

$$\sigma = G(\gamma - \gamma^{-2}) \qquad\qquad (2.41)$$

and for $\gamma - 1 \ll 1$, linear behaviour is obtained:

$$\sigma = G(\gamma - 1) \qquad\qquad (2.42)$$

A slight overestimate of the time to no slip results from the use of (2.42) rather than (2.41), but it is negligible as $\gamma \to 1$. A solution to (2.31) is derived for the linear elastic solid (2.42) in Appendix 2. Essentially, the function $\sigma_0(t)$ is determined. The time to no slip, t_{ns}, is obtained from (A2.5) using the condition for no slip in (A2.8); thus

$$t_{ns} = \frac{R}{\overset{\bullet}{\mu\epsilon}L} \ln\{e^1(y+1) - ye^{-\mu\pi/2}\} \ , \ y = (\frac{\mu L}{R} - 1)^{-1}$$

$$(2.43)$$

Since equation (2.34) holds when slip ceases, t_{ns} can be plotted

against $\dot{\sigma}_o/(\sigma_o\dot{\epsilon}) = L\mu/R = 2\mu$, which has been done in fig. 2.7,

Curve B. It appears that Curves A and B do not intersect though

they both have the same asymptote as $\gamma \rightarrow 1$, $t \rightarrow 0$, which suggests

that the friction factor is very large and that slip does not occur.

2.4   Results

The first results to be presented concern an essential

checking of the data obtained from the two rheometers as far as that

is possible.   As Dealy [47] remarks, it is important with new

machines to establish that the required property is being measured

correctly. This proves to be difficult with the Elongation Rheometer

since it covers a range of constant strain rates of 1-110 s^{-1}.

At the time of the experimentation the author was not aware of any

machine with a comparable range. However, a machine belonging

to Loughborough University with a maximum strain rate of 1 s^{-1}

was used in the hope that it would be possible to 'butt' the data.

Checks for the T.M.S. Rheometer were much easier to achieve and

the results show that it compares well with a Davenport Capillary

Rheometer and the Rheometrics Mechanical Spectrometer.

Having established the validity of the Rheometers, the main

experimental results are presented for two types of rubber,

namely poly(chloroprene) and poly(isobutene-co-isoprene) which will

be referred to as Chloroprene and Butyl rubber, respectively.   The

Chloroprene rubber is used as a fully formulated unvulcanised compound

with the following constituents:

Component	parts per hundred
poly(chloroprene)gum	100
carbon black	16.67
calcium carbonate	58
paraffin oil	6.3
curing system	-

Details of the curing system are not given, but it is in any case only a small component, probably with little influence on the properties of the unvulcanised compound.

The Butyl rubber is used both as a raw gum and as a semi-formulated compound with the constituents:

Component	parts per hundred (quantity)
poly(isobutene-co-isoprene)	100
carbon black	71
zinc oxide	3.5
stearic acid	1
paraffin oil	27

This compound contains no curing system which makes it easier to use than the Chloroprene compound but still changes its properties over long periods of storage time. (A reference to this is made later in the experimental results).

2.4.1 Checking the rheometer data

Turner and Moore [36] compared the data obtained from the T.M.S. Rheometer and a Davenport Capillary Rheometer for the steady

shear flow of a non-wall slip compound B-O-A (B6138) at 100°C.

Both the grooved and smooth rotors were used for the T.M.S.

measurements confirming that the material exhibited no slip in the

shear rate range investigated.   A 30 × 2mm die was used for the

Davenport measurements.   Fig. 2.8 shows a replot of their results

of stress against true shear rate at the wall.   The agreement is

good with less than 5% error where they overlap.   Also shown in Fig. 2.8
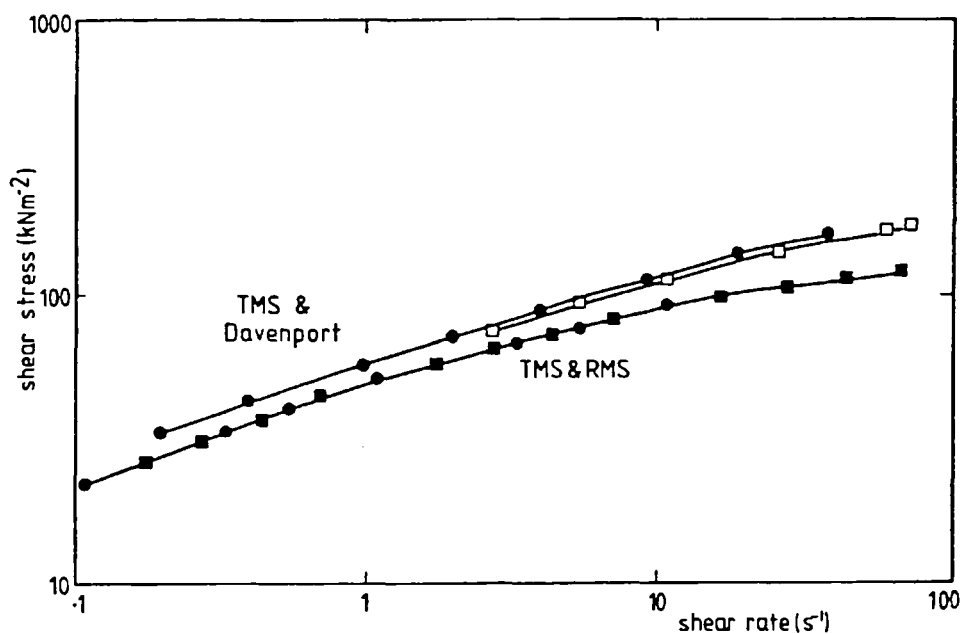

Fig. 2.8   Comparison of steady state shear stress
measurements on the B-O-A compound: T.M.S.
Rheometer ●, Davenport Capillary Rheometer □,
and on the Butyl compound, shear stress using
the T.M.S. ● compared with oscillatory data
from the R.M.S. ■; Cox-Merz rule has been used.

are measurements on the Butyl compound using the T.M.S. and a

Rheometrics Spectrometer.   The latter results were obtained inde-

pendently: courtesy of Dr J. Funt, then of Rheometrics Inc.   As only

the oscillatory data from the R.M.S. was acceptable (the Butyl

compound appears to be too stiff or elastic to be contained properly

within the R.M.S device under conditions of steady shear) the Cox-Merz

rule [48] is used for comparison with the steady shear data from

the T.M.S. The agreement is remarkable, though the result is not as

strong as it would be if data from the same experiment were compared.

For rubbers which exhibit wall-slip, see fig. 2.9 for

a typical plot of the results, it is possible to compare the data

from the T.M.S. and Davenport by using a simple model of the slip

mechanism. The model has been used for calculations on tube flow

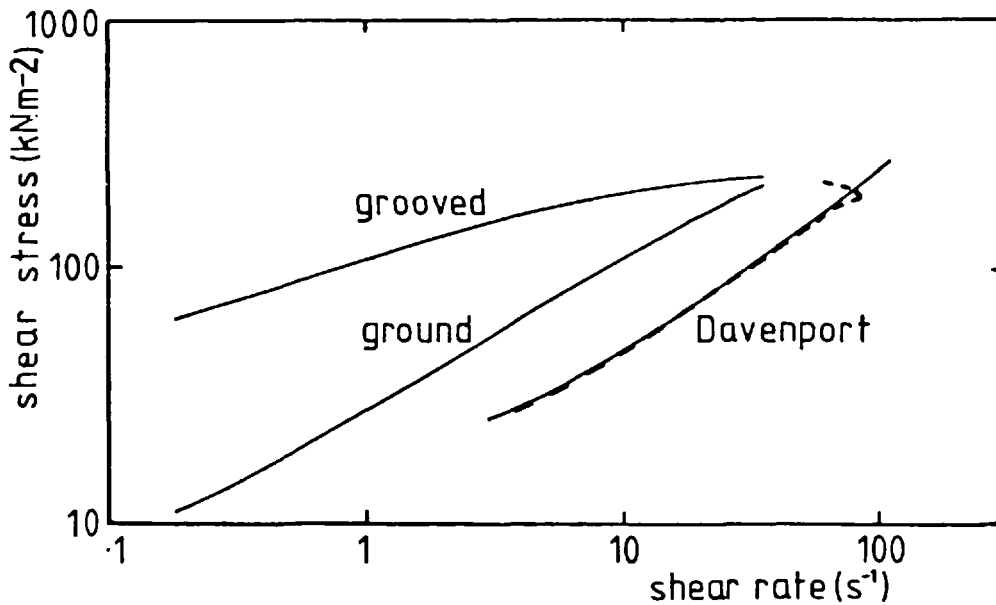by Uhland [49]. An extension of the basic idea is now considered.

Fig. 2.9 Shear stress as a function of apparent shear
rate from measurements on EPDM using the grooved
and ground rotors of T.M.S. and Davenport
Rheometer (————) Prediction of (2.44) using
experimental data (——————).

It is assumed that a thin, low viscosity layer can develop between

a sufficiently smooth metal surface and the bulk of the rubber.

Neither the layer thickness nor the rheology is specifically known.

However, it is further assumed that the total flow is viscometric

in both layers and that a power-law model is a suitable description

of the viscosity. One further assumption is that the relative

thickness of the lubricating layer to the bulk rubber layer depends

only on the local shear stress. This provides a means of comparing

the flow in a cylindrical die with that in a cone and plate. The

detailed calculation is carried out in Appendix 3. The final result

relating the apparent shear rate in the capillary $\dot{\gamma}_A$ to the shear rate

in the T.M.S. using the grooved rotor $\dot{\gamma}_{grooved}$ and the apparent shear

rate using the ground rotor $\dot{\gamma}_{ground}$ is

$$\dot{\gamma}_A = 4\{\dot{\gamma}_{ground} - \frac{2n+1}{3n+1} \dot{\gamma}_{grooved}\} \qquad (2.44)$$

where the shear stress is the same for each $\dot{\gamma}$ and n is the

power-law index. In Fig. 2.9 the capillary rheometer data is compared

with the prediction in (2.44) with excellent agreement except at the

shear stress where the curves from the ground and grooved rotors

approach an intersection. Here the predicted curve suggests an

instability in the capillary results, similar in form to many other

results in the literature e.g. Uhland [49], which does not, in fact,

occur. It may be that slip is occurring on the grooved rotor at

the higher stresses, but presently the explanation is not clear. Even

still, it is intended that fig. 2.9 is seen as a further confirmation

of the accuracy of the results from the TMS Rheometer and that

it should prove a useful tool for the study of the wall-slip

phenomenon.

As already mentioned at the beginning of section 2.4, veri-

fication of the results from the Elongation Rheometer is less

straightforward. Also after the experiments were completed, a fault

in the construction of the Loughborough machine was discovered, which

invalidated the data through most of the strain rate range; only

the uppermost range up to 1 s^{-1} seemed unaffected by the fault.

Rather than repeat the experiments, just the data obtained at 1 s^{-1}

is used for comparison with the Elongation Rheometer: Instead

of plotting the data at a constant strain rate it is plotted in

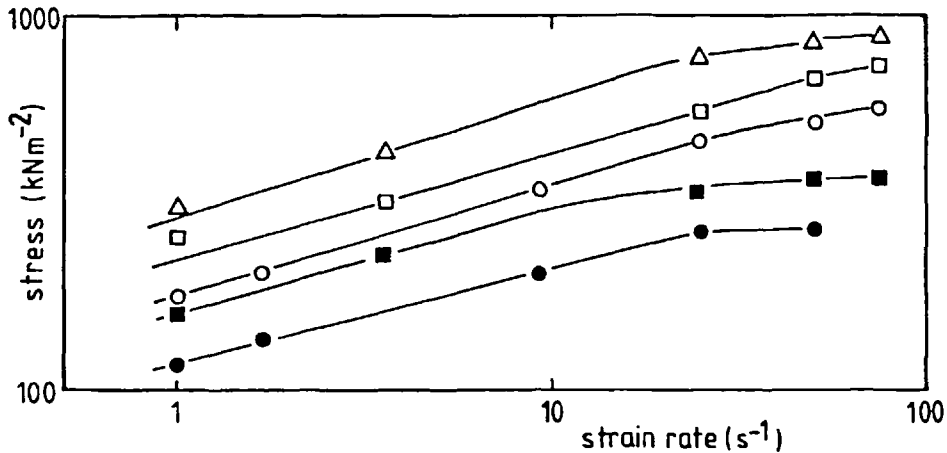fig. 2.10 at a constant strain $\dot{\epsilon}t$ (and temperature).   The

Fig. 2.10   Elongational stress as a function of
            strain rate for butyl compound:
            $\triangle$ 60°C, $\dot{\epsilon}t$ = 1.0; $\square$ 80°C, $\dot{\epsilon}t$ = 1.0;
            O 100°C, $\dot{\epsilon}t$ = 1.0; $\blacksquare$ 80°C, $\dot{\epsilon}t$ = 0.5;
            $\bullet$ 100°C, $\dot{\epsilon}t$ = 0.5.   Loughborough data
            are the points at a strain rate of 1 s^{-1}

material used is the Butyl compound. As can be seen from the figure,

the Loughborough data consistently lies on straight lines through

each set of points over a wide range of strain and at different

temperatures.   This is some confirmation of the Elongation Rheometer

results.

It will prove more relevant to consider the linear viscoelastic

behaviour of the rubbers for a confirmation of the results. As is

well known, at small rates of deformation, and/or small strains

the start-up flows of viscoelastic fluids in simple shear and uniaxial

extension should be related by a factor of 3.   This will be checked

when the main results are presented later in this section.

2.4.2   Main results

        The viscosity is defined as a function of shear rate by [48]

$$\eta = - \tau_{xy}/\dot{\gamma}_{xy} \tag{2.45}$$

        Viscosity data are shown in Fig. 2.11 for both Butyl and Chloroprene rubbers. The time-temperature superposition principle (T-T.S.P) has been used for the more extensive data.   It is necessary to extrapolate the data to obtain the viscosity at limitingly small shear rates, η_o. This is an unfortunate consequence of the large relaxation times of rubbers. There is not much significance in the fact that the viscosity of the Butyl gum is higher than that of the Butyl compound, since a considerable reduction in the molecular weight takes place in the mixing process. The effects of ageing can be clearly seen from the figure. There is a interval of about six months between the two Butyl compound curves. The later measurements, Butyl C II, have both a lower viscosity and different high shear rate slopes. This demonstrates the care necessary in planning experiments.

        The T.M.S. Rheometer cannot be used to measure the first normal stress difference in shear flow but one such measurement using the Rheometrics Mechanical Spectrometer has been made independently for the Butyl compound.   This is shown together with the shear stress in Fig. 2.12. At low shear rates, the normal stress curve has a greater slope than the shear stress, but at higher rates the slope decreases more rapidly. The shear stress is greater than the normal stress for all shear rates. This is in contrast to the measurements of Vinogradov et. al. [50] on a polyisobutylene gum
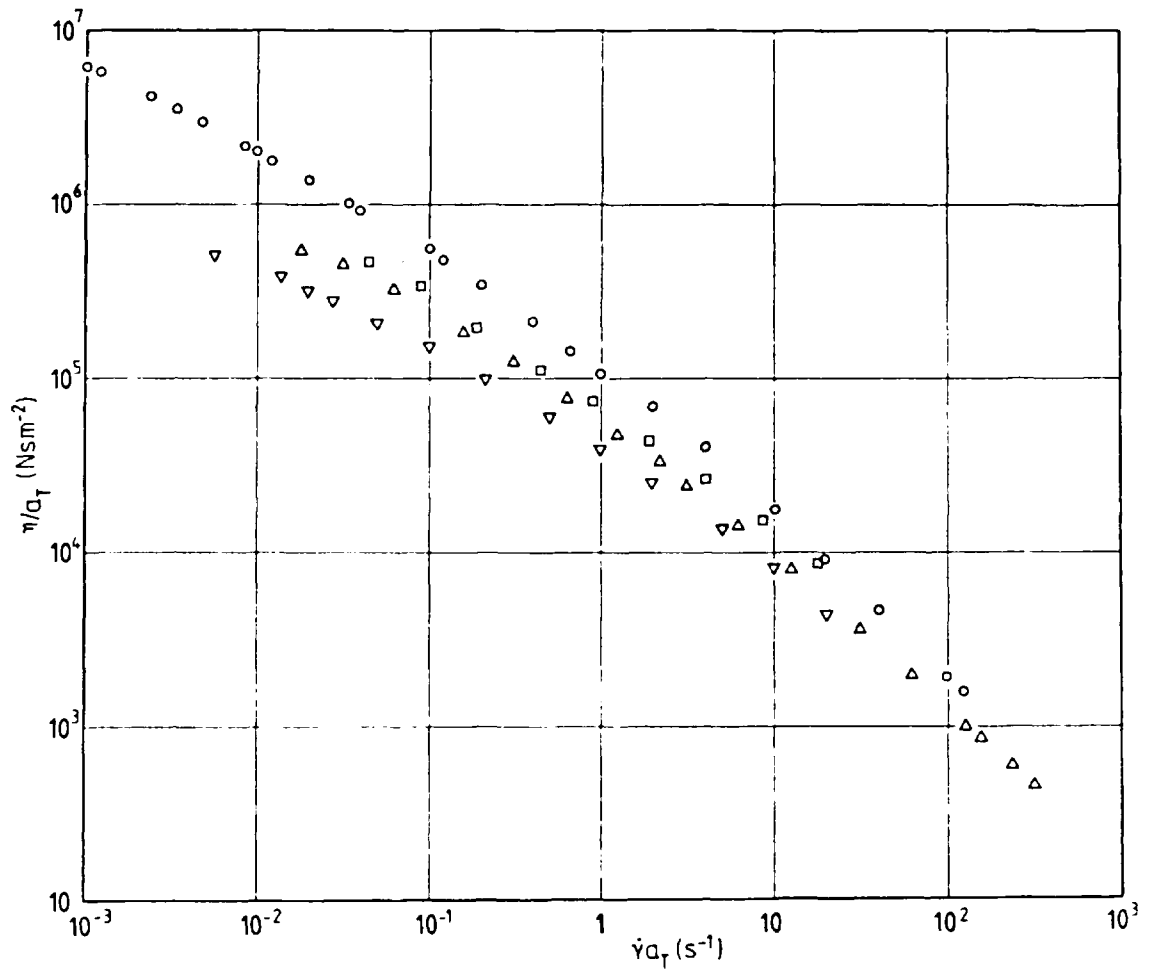

Fig. 2.11   Viscosity data for Butyl gum rubber, O,
Chloroprene compound □, Butyl compound CI △,
Butyl Compound CII ▽, plotted as reduced viscosity
vs. reduced shear rate, reference temperature 100°=373K.
(Data for Butyl gum rubber, courtesy A.C Bickley).

where at a shear rate of about 1 s^{-1} (at 100°C) the two stress

curves intersect and at higher values of shear rate, the normal

stress is significantly higher than the shear stress.   In fact

they find that $N_1 \propto \tau_{r\theta}^2$.

The time-temperature shift factor a_T is shown as a function

of temperature in fig. 2.13 for the Butyl CI compound. The glass

transition temperature is 202K [43] and the reference temperature

is 373K. The data points can be fitted either to the WLF equation

or an Arhenius equation; both these are shown in the figure where

$$\lg \ a_T \ = \ 4.816 \ - \ \frac{8.86(T+21)}{101.6 \ +(T+21)} \qquad \text{(WLF)}$$

$$a_T \ = \ 1.864 \times 10^{-8} \ \exp\{6.641 \times 10^3/T\} \quad \text{(Arhenius)}.$$

The graph shows that at the normal processing temperatures

of 80°C-140°C the viscosity changes quite rapidly with temperature;

the viscosity changing by a factor of two for a temperature

difference of 15°C.

Measurements of stress during the start-up of elongation

and simple shear flow for the Butyl compound are shown in figs.

2.14-2.16 over a range of temperatures 60°C, 80°C and 100°C. The

results are plotted in terms of the stress growth function η^+ [48]

and is defined in the two different deformation modes below.

In uniaxial extension

$$\eta_{el}^+(\dot{\epsilon},t) \ = \ - \ \frac{(\tau_{zz} - \tau_{rr})}{\dot{\epsilon}}$$

and in simple shear

$$\eta_{sh}^+(\dot{\gamma},t) \ = \ - \ \frac{\tau_{r\theta}}{\dot{\gamma}} \qquad\qquad (2.46)$$
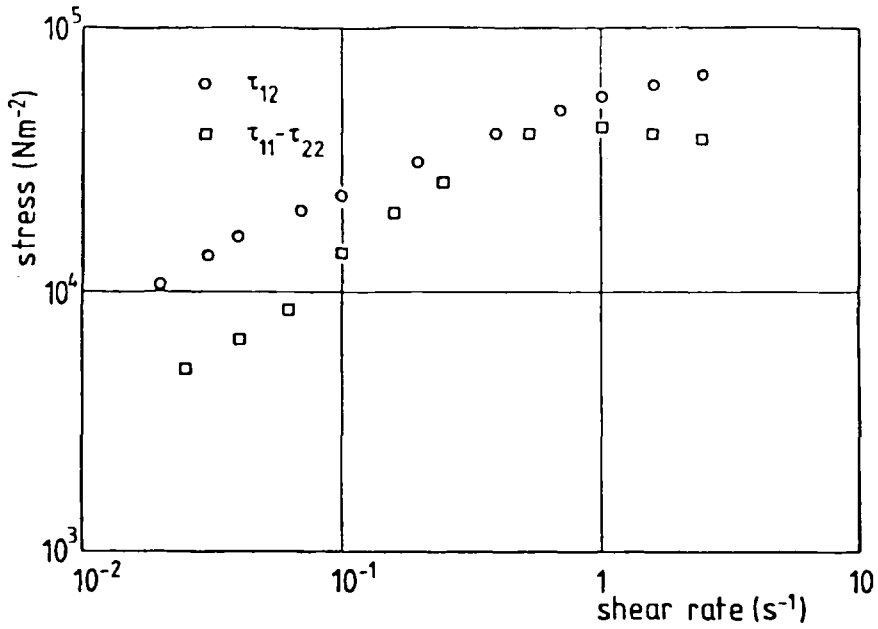
Fig. 2.12 Comparison of first normal stress difference
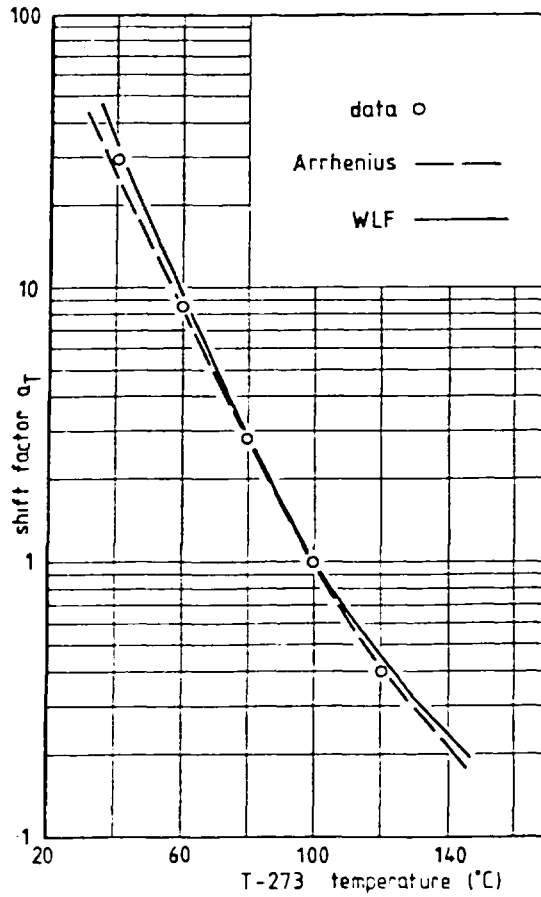(data courtesy of J. Funt) and shear stress in
steady simple shear for Butyl CI.

Fig. 2.13 Shift factor for Butyl CI, fitted to Arrhenius
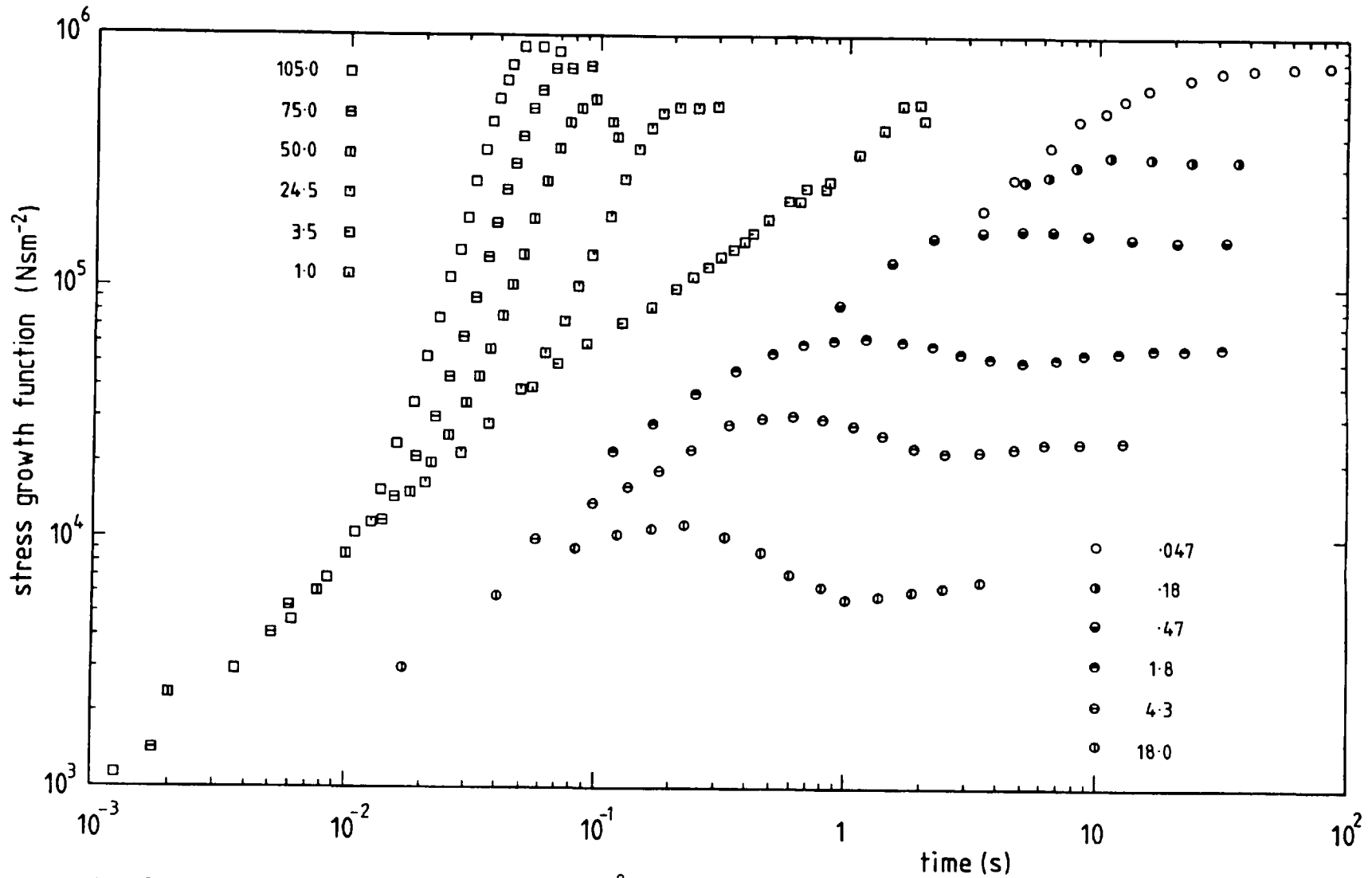and WLF equations

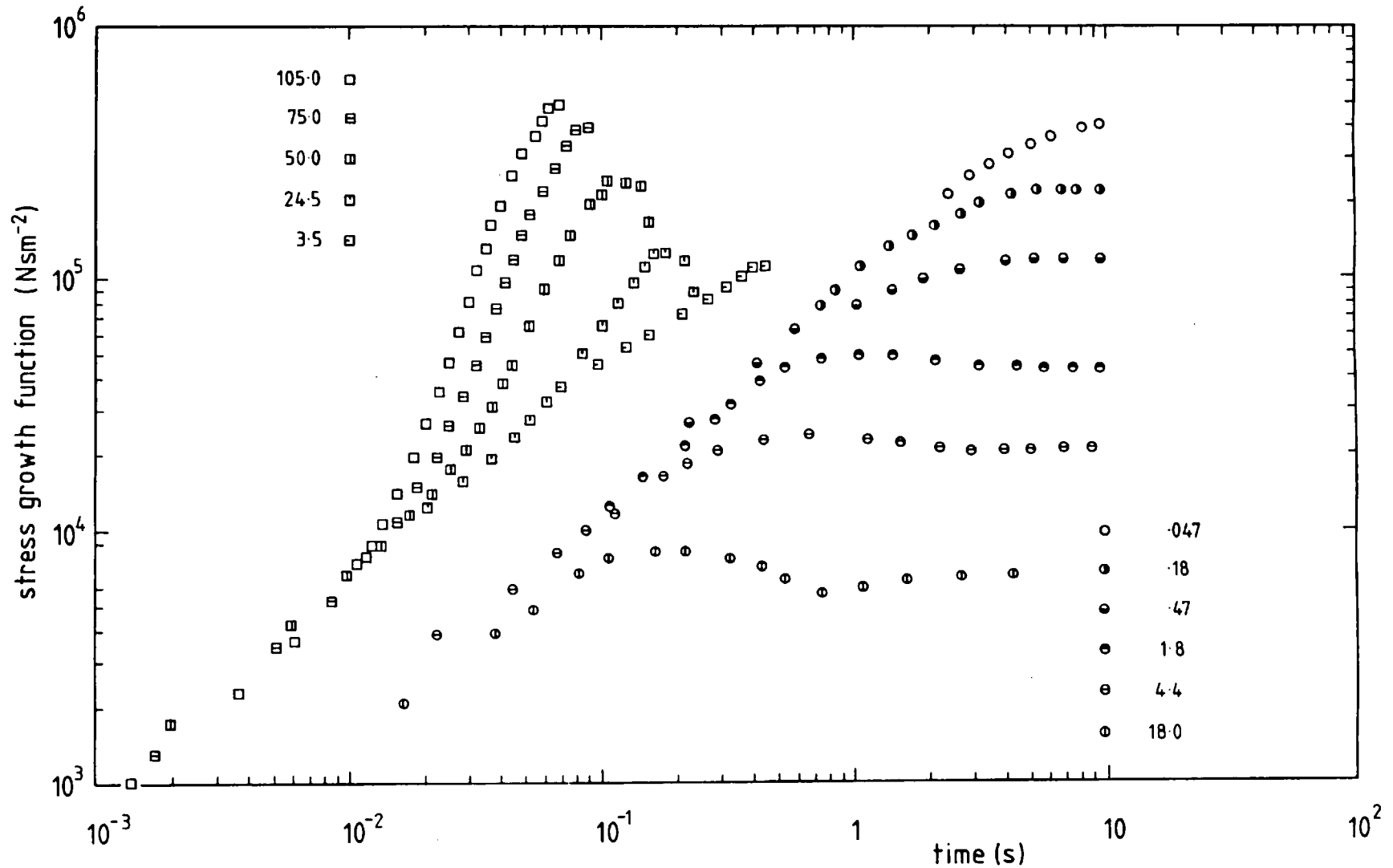Fig. 2.14 Start-up data for Butyl CI at 60°C: □ uniaxial extension, O simple shear, rates indicated in (s⁻¹)

Fig. 2.15 Start-up data for Butyl CI at 80°C; □ uniaxial extension, O simple shear rates indicated in (s^{-1})

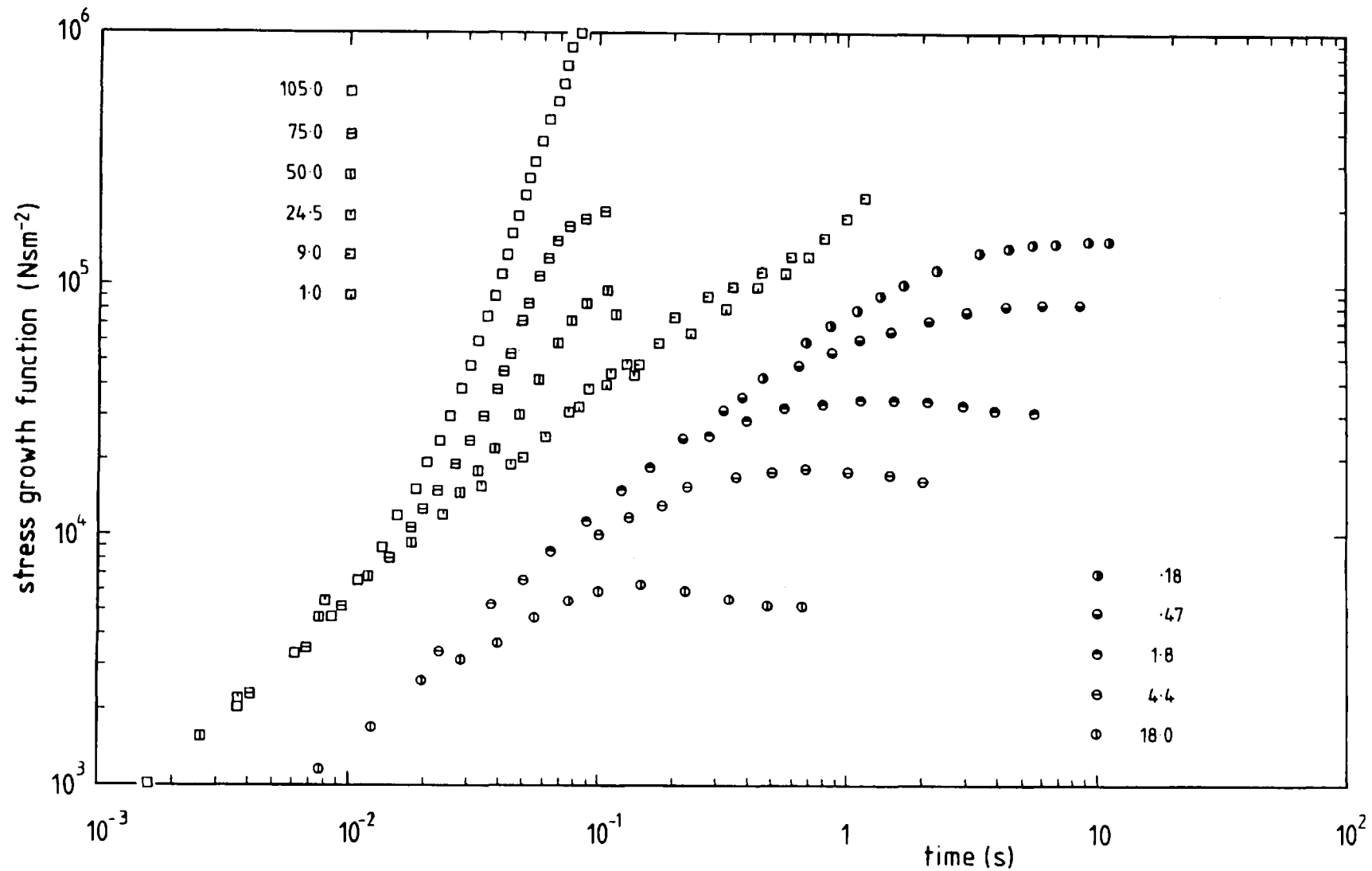Fig. 2.16 Start-up data for Butyl CI at 100°C; □ uniaxial extension, O simple shear rates indicated in (s⁻¹)

The obvious dependence on temperature has been suppressed amongst the list of variables.

The start-up curves in elongation occupy the upper portion of each graph and the data points are designated by squares, whereas the shear curves are denoted by circles. The elongation results are averaged values over a series of up to 8 separate samples. The standard deviation was small, implying an excellent reproducibility, and, in terms of a percentage of the actual values of η^+, rarely exceeded 1%. At the highest elongation rates, Hencky strains in excess of 8 were often obtained but no true steady state was achieved; though in some cases, most notably at $60^\circ C$, relatively long plateaus appeared. After reaching a maximum the stress decreased with time until failure occurred. This behaviour is reminiscent of the recent results obtained by Raible & Meissner [51] with LDPE where again steady state conditions do not appear, but only a maximum in the stress. At the lower rates such large strains of 8 were not achieved because the filaments were more susceptible to ductile failure. This could probably be improved with a higher quality of sample preparation by injection moulding rather than extrusion, but such a development does not seem presently to be justified, quite apart from the difficulty of moulding long (up to 45 cm) thin filaments.

The measurements of stress in simple shear start-up were also highly reproducible. The curves show the usual characteristics of polymer melts. As the temperature is decreased and the rate increases a local maximum appears in the curves before finally approaching the steady state. However, at still lower temperatures or higher rates a second local extremum appears, which although not particularly pronounced, is clearly evident. The phenomenon of stress undershoot

has been observed for polymer solutions [48] but not previously

for melts.

Both sets of curves, in elongation and in shear, exhibit

a linear viscoelastic envelope, see in particular fig. 2.14.

From linear viscoelastic theory, it is expected that the

envelopes are simply related, but from a theoretical point of view,

it is not yet clear whether the linear viscoelastic behaviour is

reached in the limit of small deformations or small deformation

rates or both. The experimental work of Phillipoff [52] however,

resolves the question. He conducted large amplitude oscillatory

simple shear flow experiments to determine whether linear visco-

elasticity was approached in the limit of small amplitudes or small

oscillatory frequencies. He determined that small amplitudes are

the essential requirement for linearity. Referring now to start-up

experiments,this corresponds to small values of strain $\dot{\epsilon}t$ or $\dot{\gamma}t$.

Thus even at the highest rates, the curves should form part of the

linear viscoelastic envelope at small enough times. It is a simple

result from linear viscoelastic theory to show that

$$\eta^+_{el} = 3\eta^+_{sh} \qquad \begin{array}{l} \dot{\gamma}t \rightarrow 0 \\[2mm] \dot{\epsilon}t \rightarrow 0 \end{array} \qquad (2.47)$$

The results in Figs. 2.14-16 confirm this relation very well, except

for the upper part of the envelopes at 80°C and 100°C. Here the

elongation curves corresponding to the lowest strain rates 'dip'

a little towards the shear curves. However, as will be demonstrated

in section 2.5, at the higher temperatures and lower rates slip does

occur to a small, though not negligible, extent. This would account

for lower stress values being recorded.

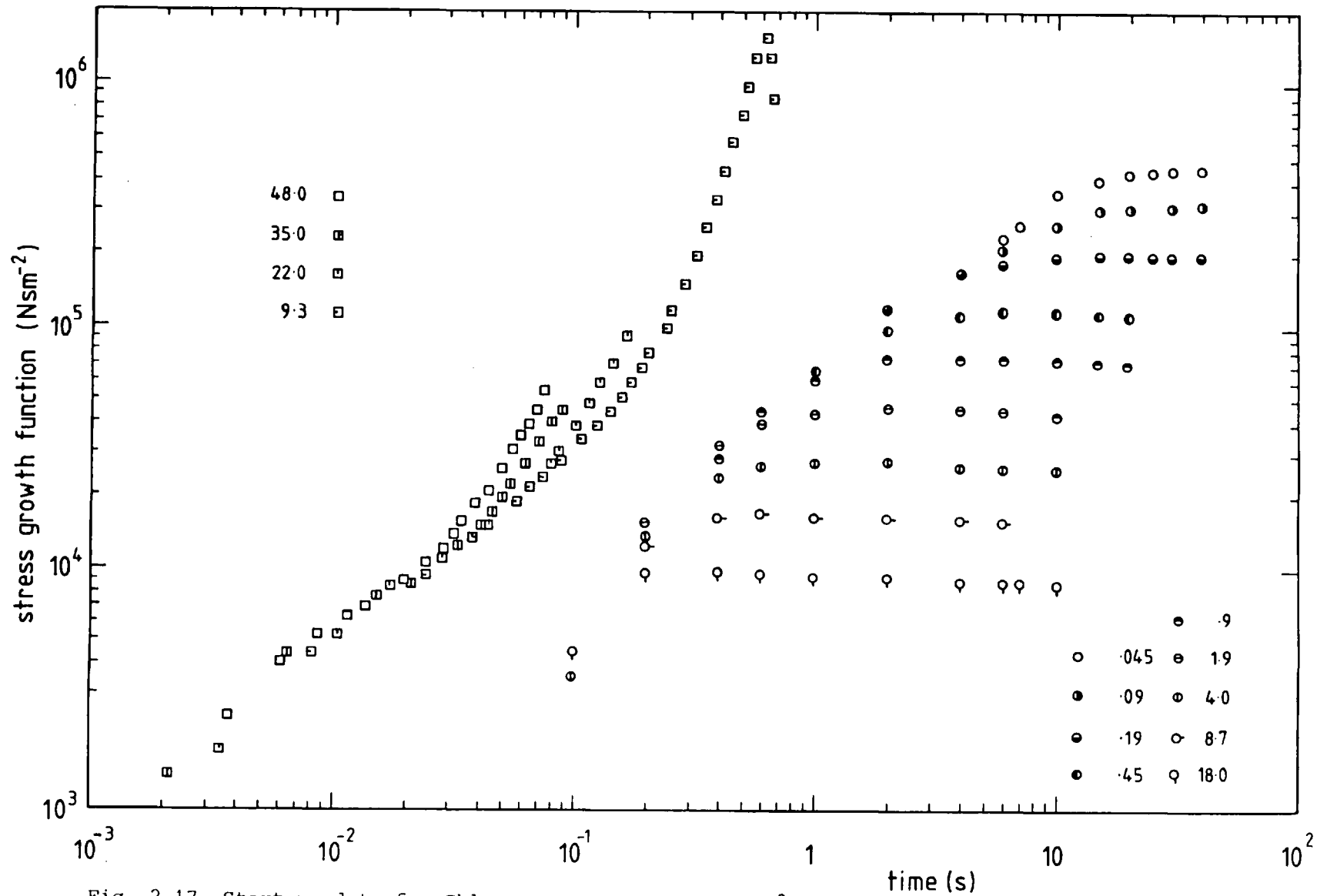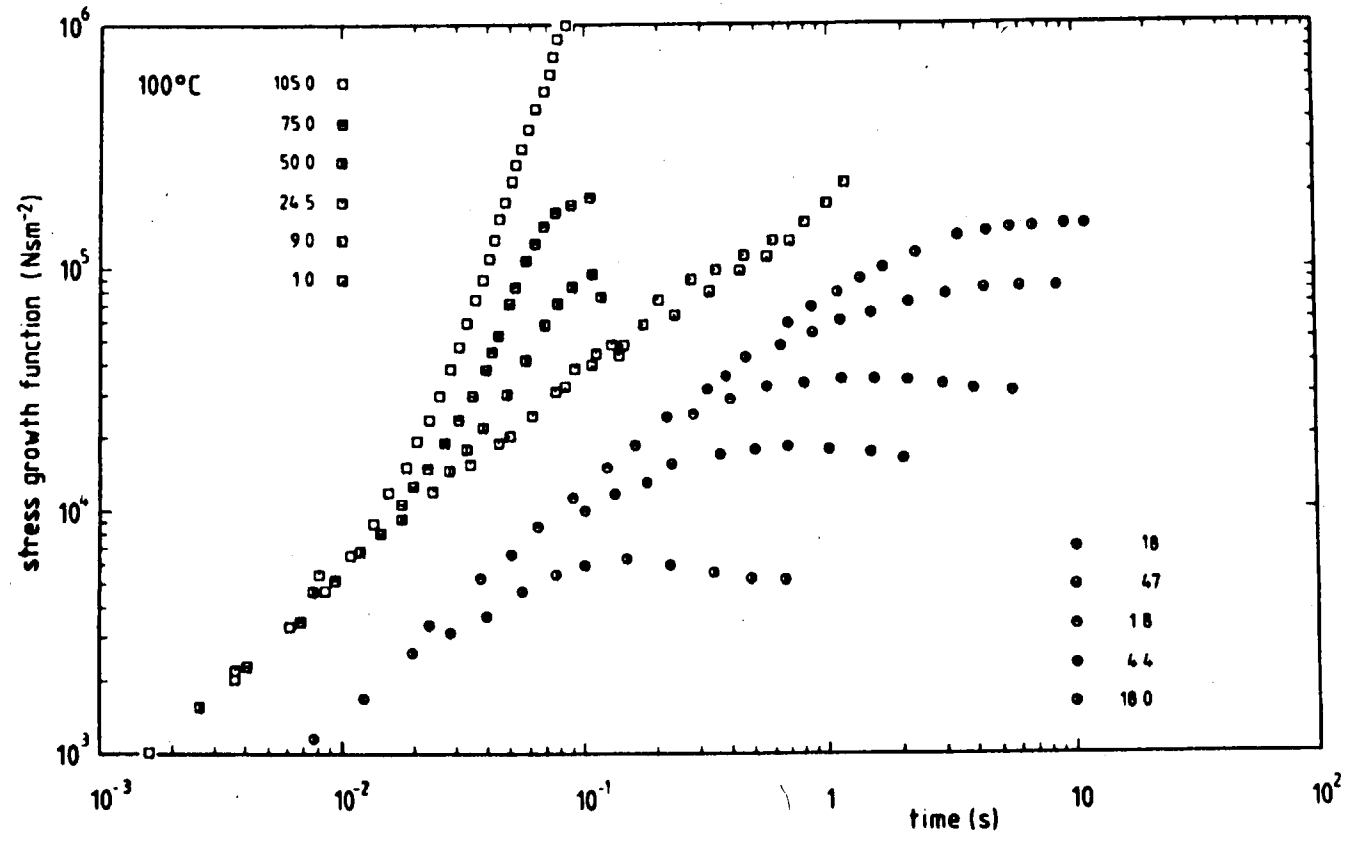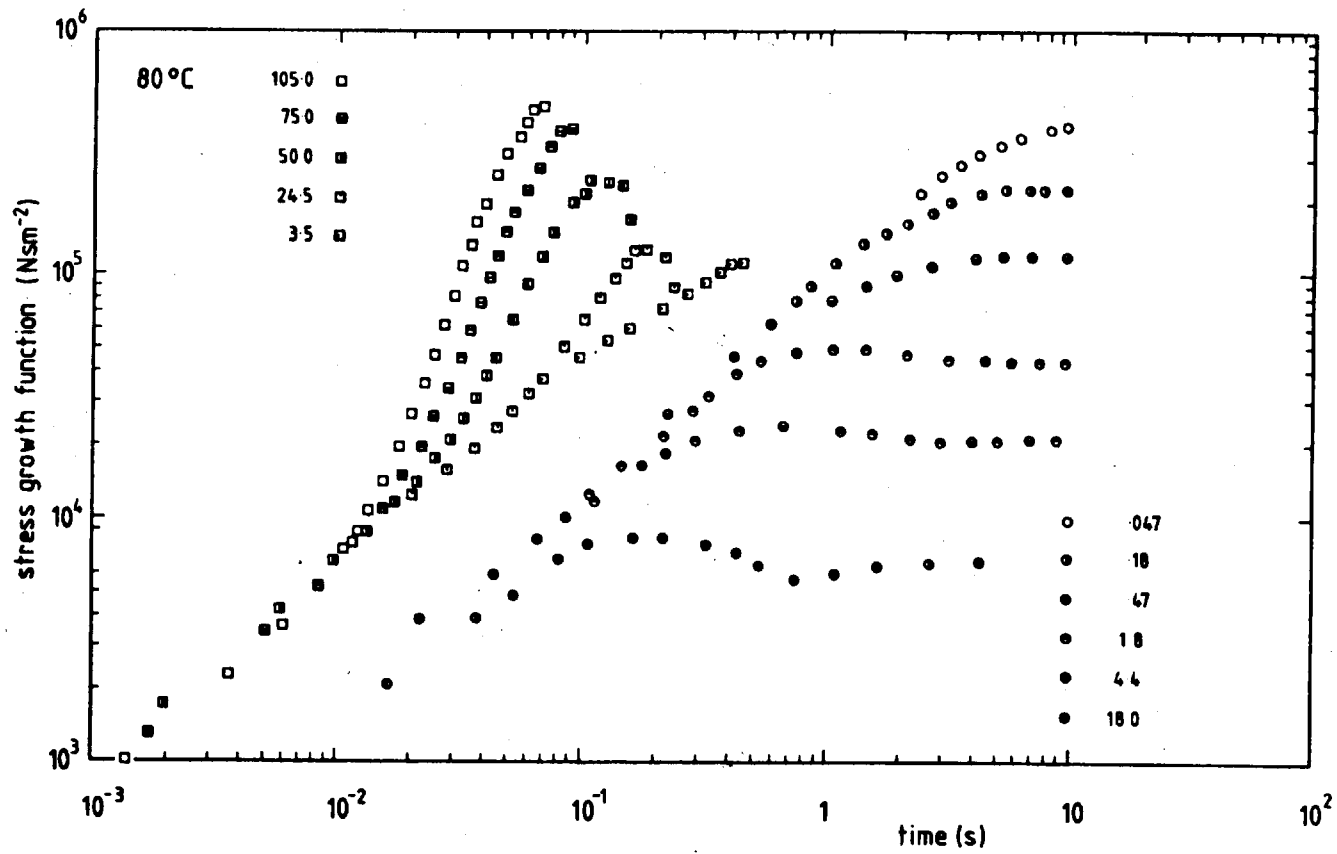Similar results have been obtained at one temperature of

Fig. 2.17   Start-up data for Chloroprene compound at 100°C;□ uniaxial extension,   O simple shear,rates indicated in (s⁻¹)

$100°C$ for the Chloroprene rubber, fig. 2.17. All previous remarks

carry over to this rubber with one exception. Even at the highest

shear rates there is hardly any perceptible stress overshoot. There

seems to be a much greater contrast in the shear as opposed to

the elongation start-up behaviour of the two rubbers.

The time-temperature superposition principle has already

been used in the construction of the viscosity curves and is a

well-used technique for other properties such as relaxation

behaviour or the shear modulus. However, each of these applications

results in a single master curve. The T-T.S.P. should also apply

to start-up behaviour, but a whole family of master curves would

be the result. The principle is basically a transform applied to

the time scale and therefore to any parameter which explicitly involves

either a time or a strain rate. So the three parameters involved

in start-up flows $\eta^+, \dot{\gamma}$ or $\dot{\epsilon}$, and t are transformed as follows:

$$\eta^+ \rightarrow \eta^+/a_T$$

$$\dot{\gamma} \rightarrow a_T\dot{\gamma}$$

$$t \rightarrow t/a_T$$

where a_T is the shift factor with values as in Fig. 2.13 for the

Butyl CI compound.

The transform may be applied to figs. 2.14-2.16 by shifting

the axes relative to each other by the amount $a_T(T)$ provided that it

is also realised that the values of the rates change by the same

factor. This process is shown in fig.2.18 where the graphs have

been photocopied onto transparencies and then displaced relative

to each other by the required amount. As can be seen this

works excellently, with a highly consistent family of curves produced.
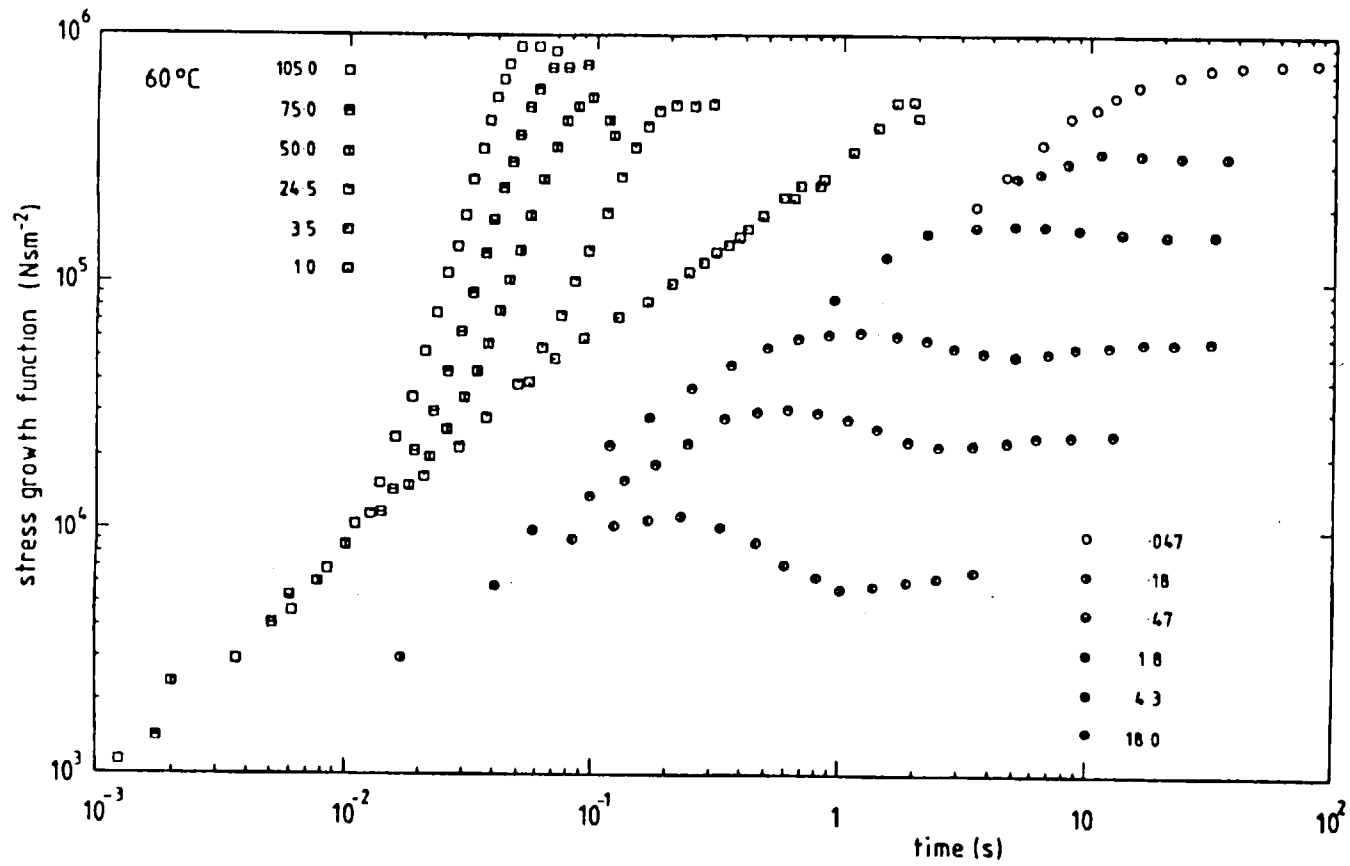
Fig. 2.18   Demonstration of T-T.S.P. in start-up, using Butyl CI

The viscoelastic envelopes are maintained and in a number of instances, corresponding curves overlap very closely.

This technique results in increasing the strain rate range by a factor of 10 at any one particular temperature, so that if the reference temperature is chosen as $100°C$, the strain rate ranges are 1-1000 s^{-1} in elongation and 0.15-180 s^{-1} in shear.

2.5 Modifications to the Elongation Rheometer for an Experimental Study of Slip

In section 2.3 an attempt was made to deal with the problem of slip of the rubber filament over the take-up wheel from a theoretical point of view. A more direct answer to the problem may lie in an experimental study. The idea is to increase the frictional force between the take-up wheel and the filament by constructing a take-up wheel with a deeply grooved rim of half angle $\alpha = 12°$ as shown in fig. 2.19. The sample rests in the groove and the coefficient of friction is increased by a factor of $1/\sin\alpha \simeq 5$. Ideally, the depth of the groove should vary with angular position so that as the filament is wound up its distance from the axis of rotation of the take-up wheel is constant. However, this would introduce severe machining problems and a small correction is made to the data instead. The distance, or effective radius R_{eff}, depends on the filament thickness at any position and the extent to which the filament has been deformed by the shape of the groove. Fig. 2.20 shows the geometry of a cross-section of the filament and groove.
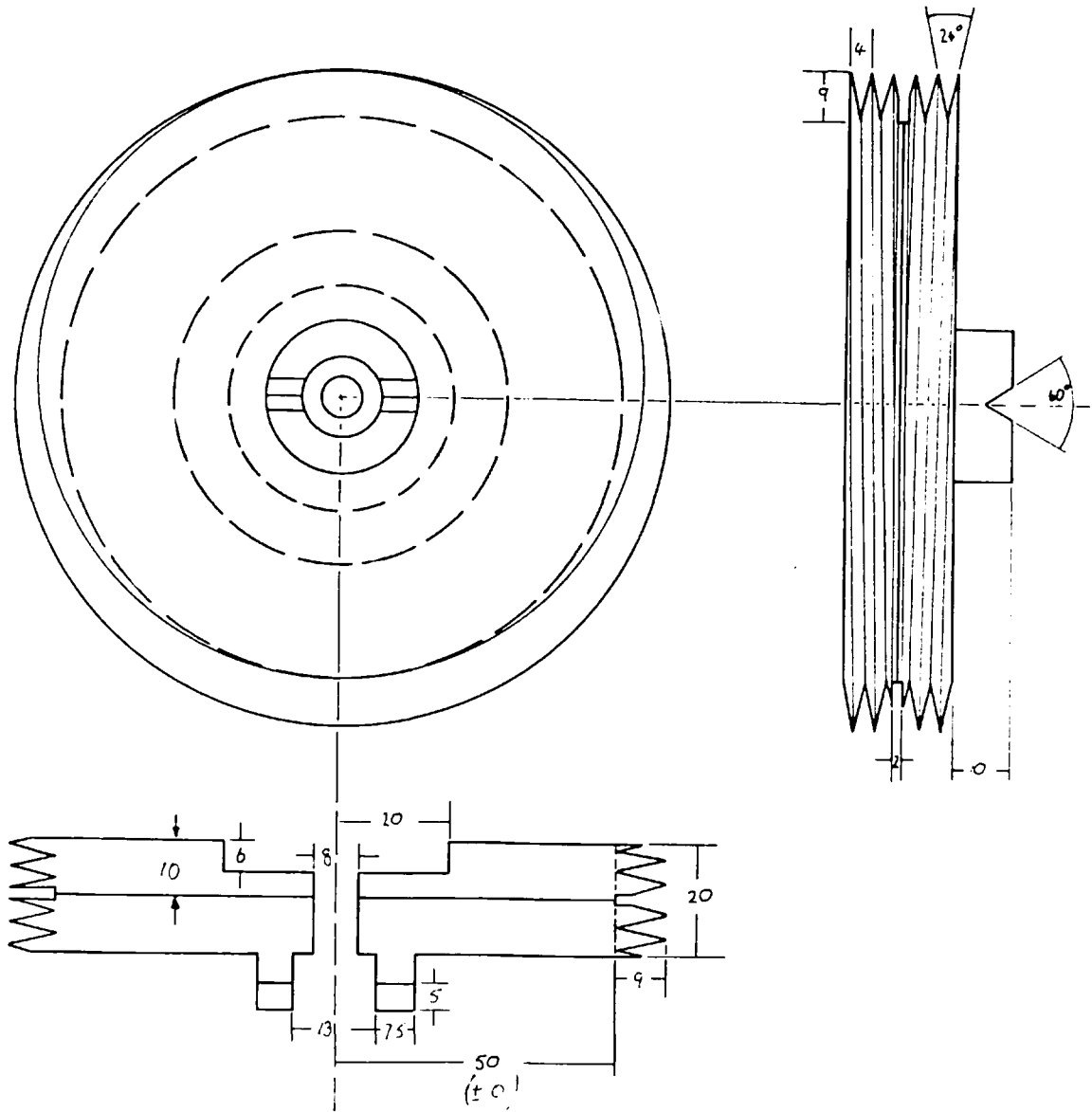
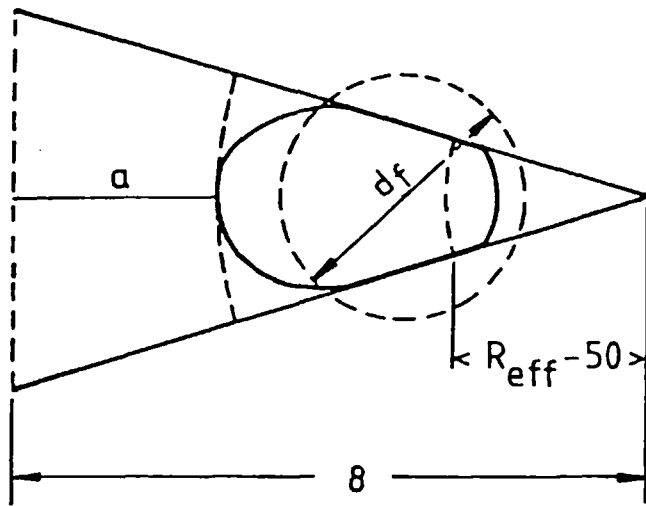Fig. 2.19 Design drawing of grooved take-up wheel. Dimensions in (mm)

Fig. 2.20 Cross-section of geometry of filament in
groove of take-up wheel.

When the filament is removed from the groove after extension at

some particular temperature and rate, it recovers to a circular

cross-section. R_{eff} is taken as the lowest point of contact of the

filament and the groove. By conducting a number of filament

extensions at two temperatures, 60°C and 100°C and various strain

rates and subsequently measuring the distance, a, (see fig. 2.20)

and the recovered filament diameter d_f, it is possible to estimate

R_{eff}. In fact, a and d_f did not vary within experimental accuracy

either with temperature or strain rate. Table 2.1 presents

average results of a, d_f, the expected value of d_f based on the

assumption of no slip, and the estimate of R_{eff} at various angular

positions on the take-up wheel. The contact point at time t = 0

is designated 0°.

Angle ($^\circ$)	0	45	90	135	180	225	270
Depth of top or rubber, a(mm)	0	1.45	3.1	4.2	5.1	5.85	7.5
Filament diameter, d_f (mm)	3.25	2.75	2.1	1.8	1.55	1.2	1.0
No slip filament diameter, $d_f = d_o e^{-\theta/4}$	3.25	2.7	2.2	1.8	1.5	1.2	1.0
Effective Radius, R_{eff} (mm)	54.9	54.0	52.7	51.5	50	50	50

Table 2.1: Data for parameters in figure 2.20, both
measured and calculated, the factor 1/4
in the fourth line arises from geometrical
arguments.

The manner of calculating R_{eff} is indicated in fig. 2.20.
The deformed filament has a cross-sectional area, a_1, known from d_f

$$a_1 = \frac{\pi}{4} d_f^2 \qquad (2.48)$$

An upper bound for the area a_2, available for the filament is the
area of the sector of radius 8.0-a

$$a_2 = \frac{\pi}{15} (8.0-a)^2 \qquad (2.49)$$

The unoccupied area is $a_2 - a_1$ which can be given as the area of the
segment of radius R_{eff} - 50. Thus

$$R_{eff} = 50 + \{\frac{15}{\pi} (a_2-a_1)\}^{\frac{1}{2}} \qquad (2.50)$$

The values of R_{eff} as a function of θ are plotted in fig. 2.21.

Using linear regression, the angle corresponding to $R_{eff} = R = 50$ mm

is calculated to be $170°$ or 3.0 radians. The approximate

functional form of R_{eff} is

$$R_{eff} \approx 50 + (5.2-1.73\theta) \qquad \theta < 3 \text{ radians} \qquad (2.51)$$

$$= R \qquad \theta \geq 3 \text{ radians}$$
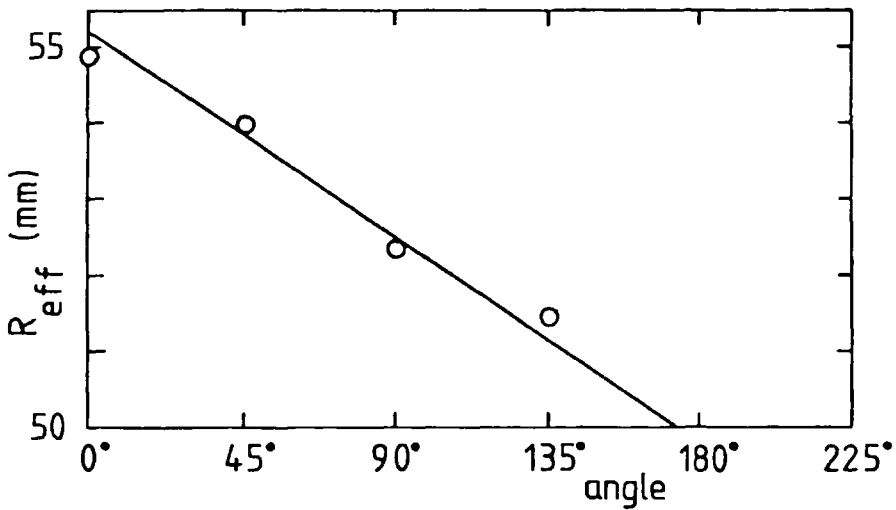
Fig. 2.21 Effective radius R_{eff} as a function of angle θ. Linear regression used to fit curve.

If the apparent strain rate $\dot{\epsilon}_A$ and stress $\sigma_A = -(\tau_{zz}-\tau_{rr})_A$

are calculated on the normal basis using equations (2.3) and (2.5)

then two corrections should be made to obtain the actual values $\dot{\epsilon}$ and

σ. These are

$$(i) \quad \dot{\epsilon} = \dot{\epsilon}_A \frac{R_{eff}}{R} , \quad \text{at} \quad \theta = 2\dot{\epsilon}_A t \qquad (2.52)$$

$$(ii) \quad \sigma(\dot{\epsilon},t) = \sigma_A(\dot{\epsilon}_A,t) \exp\{\dot{\epsilon}_A \int_o^t (\frac{R_{eff}}{R} - 1)dt\} \qquad (2.53)$$

in which the term inside the exponential function is a correction to

the Hencky strain. To obtain the actual stress at the apparent

strain rate, a necessary adjustment to enable a direct comparison with

data from the flat take-up wheel, a third correction is made by

expanding σ in a Taylor series

$$\text{(iii)} \quad \sigma(\dot{\epsilon}_A, t) = \sigma(\dot{\epsilon}, t) - \dot{\epsilon}_A \frac{\partial\sigma}{\partial\dot{\epsilon}} \left(\frac{R_{eff}}{R} - 1\right) \qquad \text{(2.54)}$$

Throughout (i)-(iii), $R_{eff}(\theta) = R_{eff}(2\dot{\epsilon}_A t)$.

Using the expression obtained for R_{eff} (2.51), the error

in the strain rate has a maximum of about 10% at t = 0, and $\dot{\epsilon}$

linearly approaches the measured value $\dot{\epsilon}_A$ as the strain tends to

1.5. For strains greater than 1.5, $\dot{\epsilon} = \dot{\epsilon}_A$. The situation is a

little more complicated for $\sigma(\dot{\epsilon}_A, t)$. The derivative in (2.54)

can be calculated from the data once it is represented in a form

similar to that in fig. 2.10.   Otherwise a simple integration gives the

result

$$\sigma(\dot{\epsilon}_A, t) = \sigma_A(\dot{\epsilon}_A, t) \, \exp(\dot{\epsilon}_A t(5.2 - 1.73\dot{\epsilon}_A t)/50) - \dot{\epsilon}_A \frac{\partial\sigma}{\partial\dot{\epsilon}} \left(\frac{5.2 - 3.46\dot{\epsilon}_A t}{50}\right)$$

$$\dot{\epsilon}_A t < 1.5$$

$$= \sigma_A(\dot{\epsilon}_A, t) \exp(0.078) \qquad\qquad \dot{\epsilon}_A t \geq 1.5$$

$$\text{(2.55)}$$

The experimental results of a comparison of the grooved

and flat take-up wheels at 60°C and 100°C, and at various strain rates,

using the Butyl CII compound, are shown in Fig. 2.22. The corrections

(i)-(iii) have been made to the grooved data, and in the main, only

the corrected data are shown in the figure.   However at the lowest

rates of each temperature the original data are indicated, except

where their inclusion would confuse the graph.   The strain axis of

the graph is the actual value of the strain in each experiment if

no slip occurs. For the flat take-up wheel the strain is $\dot{\epsilon} t$
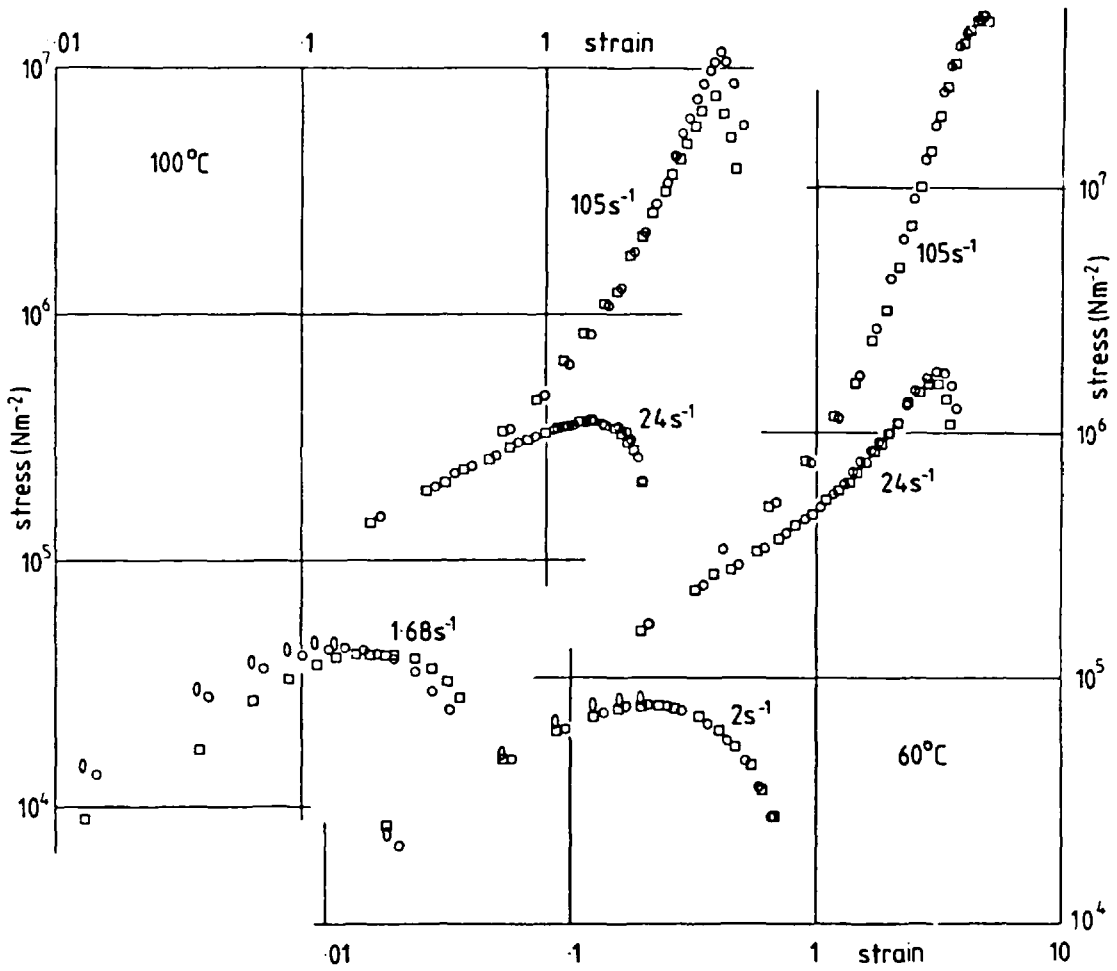
Fig. 2.22 Comparison of start-up data from flat and grooved
take-up wheels, material Butyl CII: □ flat;
O original, o corrected grooved take-up wheel data

and for the grooved take-up wheel it is $\dot{\epsilon}_A t (55.2 - 1.73 \dot{\epsilon}_A t)/50$ $\dot{\epsilon}_A t < 1.5$

and $\dot{\epsilon}_A t (1.078)$ $\dot{\epsilon}_A t \geq 1.5$

As can be seen in fig. 2.22 the differences between the two types

of data are negligible except at the lowest rate of 1.68 s^{-1}, at

the lower temperature.   Therefore, slip is practically non-existent

in the experiment, since a significant increase in the factor

controlling slip,the friction factor, causes no difference in the

results.   The one exception can be explained in terms of it representing

a tendency to less elastic behaviour and consequently a lower

interfacial shear strength.

The reason for the slip in the linear viscoelastic envelope,

mentioned in section 2.4, is now clear and is justifiably attributed

to a slight slippage.   A correction to the data of figs.2.15

and 2.16 could be made on the basis of the results here.   However,

at this stage little would be gained.

2.6   Data Fitting to a Naive Rheological Model

A large number of rheological models have been proposed

in the literature, many of which are exceedingly complex.   However,

because it is desired to achieve analytic solutions to flow problems,

a naive model is used, which contains only a few unknown constants.

The term naive was coined by Petrie [53] when he carefully considered

the problem of which model to choose for dynamical calculations.

Clearly the model should describe some of the main features of visco-

elastic behaviour yet simultaneously be mathematically tractable.

Petrie's choices for a naive model containing three parameters are

(i) Jeffreys model, either in corotational or upper

convected formalism, with constants $\eta_0, \lambda_1, \lambda_2$;

(ii) Non-affine Maxwell model,which incorporates

both the corotational and upper-convected derivatives,

with constants η_0, λ_1, a.

It is necessary to make qualifications about (i) and (ii)

as there are certain common kinematics for which the naive models are

unsuitable . Choice (i) in the corotational formalism is inadequate

for extensional deformations because in the start-up of uniaxial

extension the model does not exhibit strain hardening. In the upper

convected formalism the Jeffreys model has a constant viscosity in

steady simple shear and is therefore unsuitable for shearing flows.

Choice (ii) has the well-known defect that in steady

simple shear and at sufficiently high shear rates (and a $\neq$ 1), the

shear stress decreases with increasing shear rate, [53]. This

effectively rules out its use in shear.

It is possible to obtain a naive model which is suitable

both in the start-up of uniaxial extension and at high shear rates

by modifying (ii) to include an infinite discrete relaxation

spectrum. The model is defined in (2.56-2.60).

In an integral reprsentation the stress τ is given by

$$\tau = \frac{1}{a} \int_{-\infty}^{t} M(t-t')(I-EE^T)dt' \qquad (2.56)$$

where E is a strain tensor which is the solution to

$$\frac{\partial E}{\partial t} = AE, \qquad E(t',t') = I \qquad (2.57)$$

with $\quad A = \dfrac{a+1}{2} \; (\nabla u) + \dfrac{a-1}{2} \; (\nabla u)^T$ $\hfill$ (2.58)

The non-affine parameter a is such that a=1 corresponds to the Upper Convected and a=0 to the Corotational formalism.

The definition, so far, is similar to that in a number of recent papers [54-56] except that in these publications an error has been made, in defining τ, by an omission of the factor 1/a in (2.56). This leads to the curious, false result that in simple shear flow, all stress components vanish identically when a=0.

The Memory Function, M, is taken to have the form

$$M(t-t') = \sum_k \frac{\eta_k}{\lambda_k^2} \exp[-(t-t')/\lambda_k] \hfill (2.59)$$

and the parameters η_k, λ_k are related by the empirical equations

$$\eta_k = \frac{\eta_o \lambda_k}{\sum_k \lambda_k} \; , \quad \lambda_k = \frac{\lambda}{k^\alpha} \; , \quad k = 1,2,3,\ldots \hfill (2.60)$$

which were first given in Spriggs [57].

Thus the total number of unknown parameters $\eta_o, \lambda, a, \alpha$ is four.

It can now be shown that in the start-up of uniaxial extension the stress growth function η^+ is given by

$$\eta^+_{elon} = \sum_{k=1}^{\infty} \frac{\eta_o}{Z(\alpha)} \left\{ \frac{3k^\alpha}{(k^\alpha - 2a\dot\epsilon\lambda)(k^\alpha + a\dot\epsilon\lambda)} - \frac{2e^{-(k^\alpha - 2a\dot\epsilon\lambda)t/\lambda}}{k^\alpha - 2a\dot\epsilon\lambda} - \frac{e^{-(k^\alpha + a\dot\epsilon\lambda)t/\lambda}}{k^\alpha + a\dot\epsilon\lambda} \right\}$$

$\hfill$ (2.61)

and in start-up of simple shear

$$\eta^+_{sh} = \frac{\eta_o}{Z(\alpha)} \sum_{k=1}^{\infty} \left\{ \frac{k^\alpha}{k^{2\alpha}+(1-a^2)\lambda^2\dot\gamma^2} \left\{ 1 + e^{-\frac{tk^\alpha}{\lambda}} \left[\frac{\beta\lambda\dot\gamma}{k^\alpha} \sin\beta\dot\gamma t - \cos\beta\dot\gamma t \right] \right\} \right\}$$

(2.62)

with

$$\beta = (1-a^2)^{\frac{1}{2}} \quad \text{and} \quad Z(\alpha) = \sum_{k-1}^{\infty} \frac{1}{k^\alpha}$$

(2.63)

The linear viscoelastic behaviour, or limit, η^+_{lim} is given in shear by

$$\eta^+_{lin,sh} = \frac{\eta_o}{Z(\alpha)} \sum_{k=1}^{\infty} k^{-\alpha}(1-e^{-\frac{tk^\alpha}{\lambda}})$$

(2.64)

Finally the viscosity in simple shear is

$$\eta = \frac{\eta_o}{Z(\alpha)} \sum_{k-1}^{\infty} \frac{k^\alpha}{k^{2\alpha}+(\beta\lambda\dot\gamma)^2}$$

(2.65)

It can be shown further that a rapidly converging expansion for small $\beta\lambda\dot\gamma$ is given by

$$\frac{\eta}{\eta_o} = 1 - \frac{(\beta\lambda\dot\gamma)^2}{Z(\alpha)} \sum_{k=1}^{\infty} \frac{1}{k^\alpha(k^{2\alpha}+(\beta\lambda\dot\gamma)^2)}$$

(2.66)

and an asymptotic expansion for large $\beta\lambda\dot\gamma$ by

$$\frac{\eta}{\eta_o} \cong \frac{1}{Z(\alpha)} \left[\frac{\pi(\beta\lambda\dot\gamma)^{(1/\alpha)-1}}{2\alpha \sin((\alpha+1)\pi/2\alpha)} \right]$$

(2.67)

Equation (2.67) shows the model has a power-law behaviour in steady simple shear with a slope $1/\alpha$ -1 at large shear rates.

Turning now to the fitting of the data, equation (2.64) is used to determine η_o and λ whilst (2.67) is used for α and $\beta = (1-a)^{\frac{1}{2}}$. This ensures that linear viscoelastic behaviour is well described and that at high shear rates the model gives the correct power-law
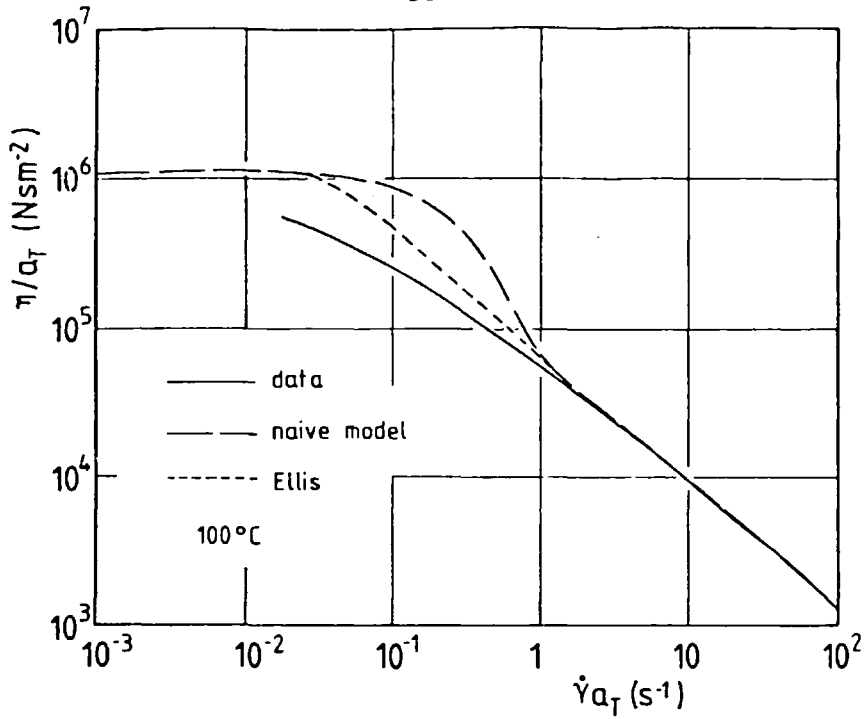
Fig. 2.23 Reduced viscosity vs. reduced shear rate for Butyl CI
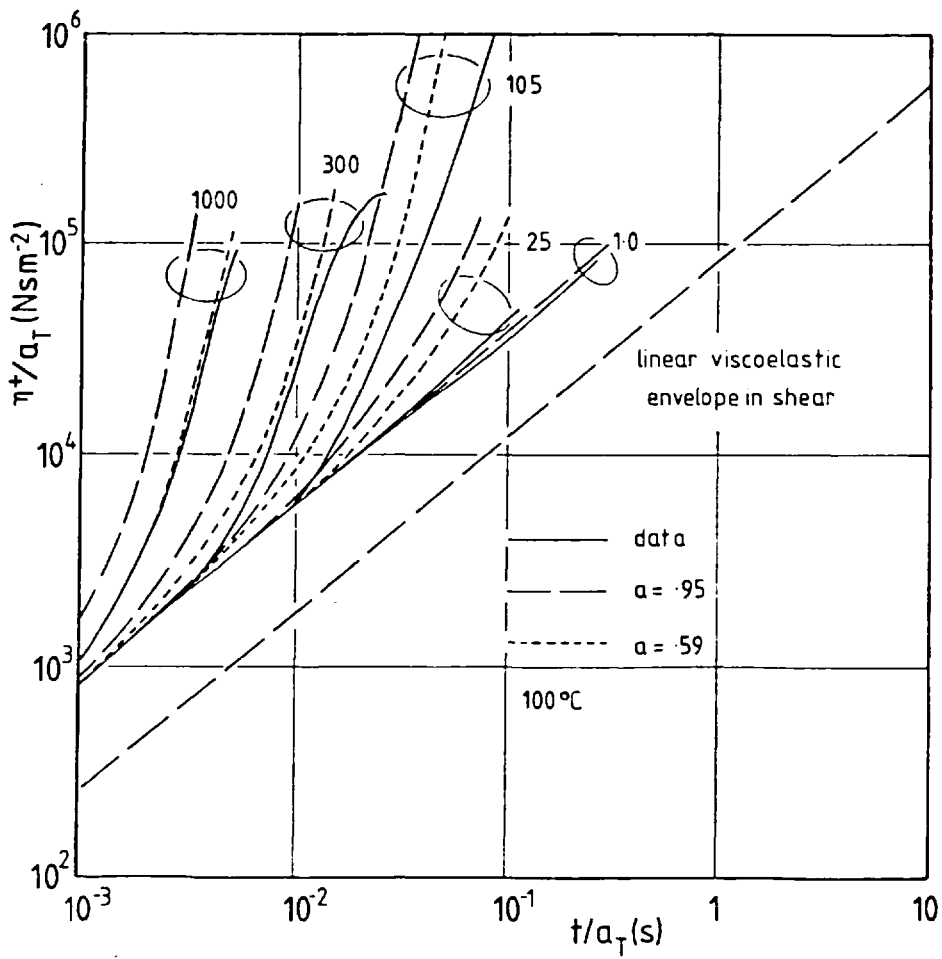and data fitting

Fig. 2.24 Recuced stress growth function vs. reduced time
for Butyl CI and data fitting

dependence in simple shear. The parameters for the Butyl CI and

Chloroprene compounds are in Table 2.2.

Rubber	Butyl CI	Chloroprene
Parameter η_o	$1.05 \times 10^6 \text{N sm}^{-2}$	$2.0 \times 10^6 \text{N sm}^{-2}$
λ	12.5s	60s
a	.95	.98
α	7.7	5.0

Table 2.2: Parameters for the generalised non-affine
Maxwell model

NB: α - very large.

The results from the model and experiment for Butyl CI are

compared in fig. 2.23 which shows viscosity curves and in fig. 2.24

which shows the stress growth functions at selected rates from those

available in figs. 2.14-2.16. The T-T.S.P. has been used with

reference temperature 100°C. From these figures it can be seen that

(i) the power-law region is well described but the

transition to low shear rates is not.

(ii) the linear viscoelastic envelopes coincide.

(iii) the model stress growth function values in uniaxial

extension lie considerably above the experimental

results.

Further to (i) it must be noted that the Careau and Ellis

viscosity equations [48] do not describe the viscosity of Butyl CI

much better than equation (2.65), they all suffer the same deficiency

of too rapid a transition from the flat 'zero shear rate' plateau

to the 'power-law region'. The model does not describe the

start-up of simple shear very well. Although it has stress-overshoot,

there are also many subsequent oscillations which are too severe,

even giving rise to negative values of the stress growth function.

A closer fit to the extension data in fig. 2.24 at the

expense of a worse fit to the viscosity in fig. 2.23, can be achieved

by a different choice of the non-affine paramter a. By taking

a=0.59 the model generates the second set of curves in fig.2.24.

The data is fitted well at high rates but rather poorly at the lower

rates.

CHAPTER 3

AN EXACT SOLUTION
FOR WEDGE FLOW

[†]General solutions are known for the slow flow of a

Newtonian and a "power-law" fluid in a wedge of arbitrary half-angle

α ($\alpha \leq \pi/2$) which involve radial streamlines [8,21]. The velocity

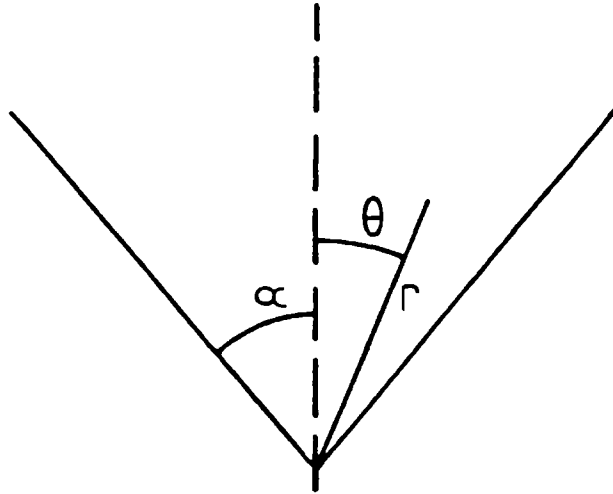field is given in cylindrical coordinates by (see Fig. 3.1)

Fig. 3.1 Geometry and coordinate system of the
flow problem.

$$v_r = - \frac{f(\theta)}{r} \quad , \qquad v_\theta = v_z = 0 \qquad (3.1)$$

for an calculable function, f, satisfying the boundary conditions.

An exact solution for the wedge flow of a Upper Convected General

_____

[†] Part of this Chapter has recently been published, see Appendix 4

Linear Viscoelastic Fluid (UCGLV-EF) involving the kinematics

(3.1) is obtained for $\alpha = \pi/2$ but not otherwise. This solution is

given below together with a discussion of its characteristics and

a comparison with the experimental data of Han [7].

3.1   The Exact Solution

At the outset no restriction is placed on the wedge

half-angle, α.   Stress and velocity fields are required which

satisfy the equations of mass conservation (3.2) and stress

equilibrium (3.3, 3.4) the relevant constitutive equation (3.5)

and the boundary conditions (3.6) for incompressible, steady slow

flow.

$$\nabla . v = 0 \qquad\qquad (3.2)$$

$$\nabla . \pi = 0 \qquad\qquad (3.3)$$

$$\pi = p\delta + \tau \qquad\qquad (3.4)$$

$$\tau = \int_0^\infty M(s) \gamma_{[0]}(s)\, ds \qquad\qquad (3.5)$$

$$v \equiv 0 \text{ on solid boundaries, i.e. } \theta = \pm\alpha \qquad (3.6)$$

Equation (3.5) is the constitutive equation for the UCGLV-EF [48].

A cylindrical coordinate system (r,θ,z) is chosen as in Fig. 3.1

with the z-axis coincident with the slit at the apex of the wedge.

The assumed kinematics satisfying the mass conservation (3.2) are

as in (3.1).

The strain tensor, $\gamma_{[0]}$, is readily calculated to be

$$\gamma_{[0]}(s) = \begin{pmatrix} -\dfrac{2fs}{r^2} - \dfrac{f'^2 s^2}{r^2(r^2+2fs)} & \dfrac{f's}{r^2+2fs} & 0 \\[3ex] \dfrac{f's}{r^2+2fs} & \dfrac{2fs}{r^2+2fs} & 0 \\[3ex] 0 & 0 & 0 \end{pmatrix}$$

$$(3.7)$$

Combining equations (3.3-3.5) yields

$$\nabla p = - \int_0^\infty M(s)\nabla\cdot\gamma_{[0]}(s)\,ds \qquad (3.8)$$

which upon substitution of $\gamma_{[0]}$ gives two partial differential equations for the isotropic stress, p;

$$\frac{\partial p}{\partial r} = - \int_0^\infty M(s)\left\{\frac{4f^2 s^2 + f'^2 s^2 + r^2 f''s}{r^3(r^2+2fs)}\right\}ds \qquad (3.9)$$

$$\frac{\partial p}{\partial \theta} = - \int_0^\infty M(s)\,\frac{2f's}{r^2+2fs}\,ds \qquad (3.10)$$

These are integrated to obtain

$$p = - \int_0^\infty M(s)\left\{\ell n\left(1+\frac{2fs}{r^2}\right)\left[\tfrac{1}{2}+\tfrac{1}{8}\left(\frac{f'}{f}\right)^2 - \frac{f''}{4f}\right] - \frac{1}{2r^2}\left(2fs + \frac{sf'^2}{2f}\right)\right\}ds + f_1(\theta)$$

$$(3.11)$$

$$p = - \int_0^\infty M(s)\ell n(r^2+2fs)\,ds + f_2(r) \qquad (3.12)$$

where f_1 and f_2 are arbitrary functions of their arguments. For the two expressions for p to be identical the following must be satisfied

$$f_1(\theta) = p_\infty \qquad (3.13)$$

$$f_2(r) = \int_0^\infty M(s)\,\ell n\, r^2\,ds + \int_0^\infty M(s)\,\frac{sK}{r^2}\,ds + p_\infty \qquad (3.14)$$

$$4f^2 + f'^2 = 4Kf \tag{3.15}$$

$$\tfrac{1}{2} + \tfrac{1}{8} \left(\frac{f'}{f}\right)^2 - \frac{f''}{4f} = 1 \tag{3.16}$$

for some constants K, p_∞. The general solution of (3.15, 3.16) is

$$f(\theta) = K \cos^2(\theta + K_1) \tag{3.17}$$

where K_1 is an arbitrary constant which, because of symmetry, may be set to zero. To satisfy the boundary conditions f must be zero for some values of θ. Clearly the only possibility is $\theta = \pm\pi/2$. Thus a solution is obtained for a $180°$ wedge and no other. The pressure distribution and the stress tensor, τ, are given by

$$p = - \int_0^\infty M(s) \left[\ell n \left(1 + \frac{2Ks \cos^2\theta}{r^2}\right) - \frac{Ks}{r^2} \right] ds + p_\infty \tag{3.18}$$

$$\tau = 2K \int_0^\infty \frac{M(s)\,s}{r^2 + 2Ks\cos^2\theta} \begin{pmatrix} -\cos^2\theta \cdot \left(1 + \frac{2Ks}{r^2}\right) & -\sin\theta\cos\theta & 0 \\ -\sin\theta\cos\theta & \cos^2\theta & 0 \\ 0 & 0 & 0 \end{pmatrix} ds$$

$$\tag{3.19}$$

A *local* Deborah Number can be defined for this flow as

$$De = \frac{2\lambda\, K\cos^2\theta}{r^2} = \xi^{-1}, \quad \text{say.} \tag{3.20}$$

Fig. 3.2 shows streamlines and lines of constant De for this flow. Notice that

θ=0

θ= π/2
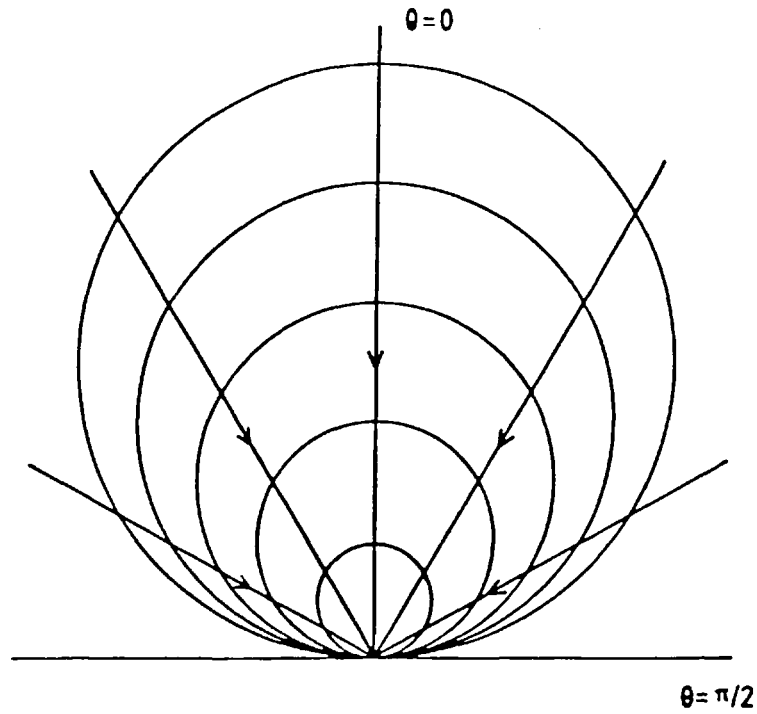
Fig. 3.2 Sketch of lines of constant local Deborah
Number (————) and streamines (——→——).
Deborah Number increases as the origin is
approached.

(i)   the kinematics of the flow are identical to those of the

corresponding flow of a Newtonian fluid;

(ii)   the value of De on the solid boundaries is 0;

(iii)   the stress and strain tensors, τ and $\gamma_{[0]}$, vanish

identically on the boundaries.

By taking a particular form of the Memory Function, M,

explicit values of τ and p can be calculated. As an illustration, let

$$M(s) = \frac{\eta}{\lambda^2} \exp(-\frac{s}{\lambda})$$ (3.21)

which represents a Maxwell fluid. The stress tensor and pressure

become

$$\tau = \frac{2\eta K}{r^2} \begin{pmatrix} -1+\sin^2\theta H(\xi) & -\sin\theta\cos\theta H(\xi) & 0 \\ -\sin\theta\cos\theta H(\xi) & \cos^2\theta H(\xi) & 0 \\ 0 & 0 & 0 \end{pmatrix}$$

(3.22)

$$p = \frac{n}{\lambda}[\frac{\lambda K}{r^2} - e^\xi E_1(\xi)] + p_\infty$$ (3.23)

where p_∞ is an arbitrary constant, and E_1 is the exponential integral function [58]. The function $H(\xi)$ is given by

$$H(\xi) = \xi(1- e^\xi E_1(\xi))$$ (3.24)

and is shown in Fig. 3.3. The stress tensor τ_N for the Newtonian
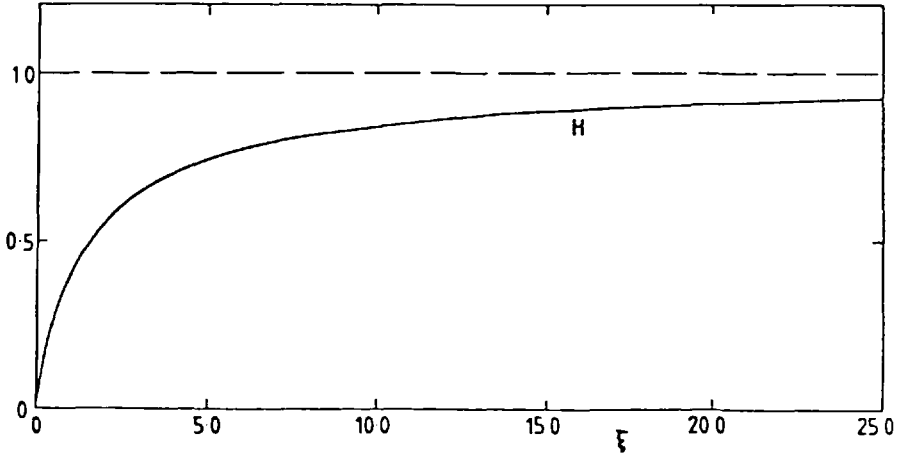
Fig. 3.3 Graph of the function $H(\xi)$ showing the asymptotic limit of 1 as $\xi \rightarrow \infty$

solution is obtained in the limit as De $\rightarrow$ 0, or $\xi \rightarrow \infty$, in which case, $H \rightarrow 1$. If ratios are taken between corresponding components of τ and τ_N for the normal stress difference and the shear stress the following are obtained:

$$\frac{\tau_{rr}-\tau_{\theta\theta}}{\tau_{N_{rr}}-\tau_{N_{\theta\theta}}} = (1-H(\xi)(\sin^2\theta-\cos^2\theta))/2\cos^2\theta$$ (3.25)

$$\frac{\tau_{r\theta}}{\tau_{N_{r\theta}}} = H(\xi), \quad \theta \neq 0, \quad \pm\pi/2 \qquad (3.26)$$

Clearly, on any streamline apart from the solid boundary the shear stress tends to 0 as the origin is approached and the normal stress difference ratio tends to a range of values in [½,1] depending on the angle of approach. The values of ½ and 1 correspond to the centre line and solid boundary, respectively.

The Power Requirement Pr necessary to pump the Maxwell fluid from an infinite sink to some finite sized exit at $r=r_0$ is [24]

$$Pr = 2 \int_0^{\pi/2} (p+\tau_{rr})v_r \, r \Big|_{r=r_0} d\theta \qquad (3.27)$$

An evaluation of this integral for an arbitrary r_0 can only be achieved numerically. However, two asymptotic relations as $r_0 \to \infty$ and $r_0 \to 0$ can readily be obtained. The prime interest in using these relations is the relative magnitudes of the power requirement for a Newtonian fluid Pr_N and a Maxwell fluid Pr_M.

As $r_0 \to \infty$ it is immediately clear from the fact that the Maxwell solution tends to the Newtonian solution as $De \to 0$, that

$$Pr_M \to Pr_N.$$

At the other extreme a simple calculation reveals that

$$\lim_{r_0 \to 0} \frac{r_0^2}{\eta K^2} Pr_M = \frac{\pi}{2} \qquad (3.28)$$

$$\lim_{r_0 \to 0} \frac{r_0^2}{\eta K^2} Pr_N = \pi \qquad (3.29)$$

Thus $Pr_M \rightarrow Pr_N/2$ as $r_0 \rightarrow 0$. Further to this, numerical

calculation of the integral in (3.27) for various values of $r_0 \neq 0$

suggest that $Pr_M \leq Pr_N$ for all r_0. Such a result was already

suspected by Black and Denn [24] from calculations on their

perturbation solution. As they also remark, the effect of elasticity

on the flow does not conform to the usual interpretation. Instead

of an increase, there is a decrease in the power requirement for a

Maxwell fluid.

An analytic solution has also been obtained for the Oldroyd

Fluid B. This fluid has a memory function representation given

by

$$M(s) = \frac{\eta}{\lambda_1^2} \left\{ (1- \frac{\lambda_2}{\lambda_1}) e^{-s/\lambda_1} + 2\lambda_1\lambda_2 \frac{\partial}{\partial t'} \delta(t-t') \right\} \qquad (3.30)$$

as defined in [48] which when substituted into (3.5) leads to

a stress tensor of the form

$$\tau = -\eta \frac{\lambda_2}{\lambda_1} \gamma_{(1)} + \frac{\eta}{\lambda_1^2} (1- \frac{\lambda_2}{\lambda_1}) \int_0^\infty e^{-s/\lambda_1} \gamma_{[0]} \, ds \qquad (3.31)$$

For the flow considered here the rate of strain tensor $\dot{\gamma}_{(1)}$ is

$$\dot{\gamma}_{(1)} = \frac{2}{r^2} \begin{pmatrix} \cos^2\theta & \cos\theta\sin\theta \\ \cos\theta\sin\theta & -\cos^2\theta \end{pmatrix} \qquad (3.32)$$

After a simple calculation the stress tensor is obtained as

$$\tau = \frac{2\eta K}{r^2} \left(-\frac{\lambda_2}{\lambda_1} \begin{pmatrix} \cos^2\theta & \cos\theta\sin\theta \\ \cos\theta\sin\theta & -\cos^2\theta \end{pmatrix} - (1- \frac{\lambda_2}{\lambda_1}) \begin{pmatrix} 1-\sin^2\theta H & \sin\theta\cos\theta H \\ \sin\theta\cos\theta H & -\cos^2\theta H \end{pmatrix} \right)$$

$$(3.33)$$

and the pressure

$$p = -\frac{\lambda_2}{\lambda_1}\frac{\cos 2\theta}{r^2}\eta K + \left(1 - \frac{\lambda_2}{\lambda_1}\right)\left[\frac{\eta K}{r^2} - \frac{\eta}{\lambda_1}e^{\xi}E_1(\xi)\right]$$

(3.34)

From these expressions it can be seen that the Newtonian solution is retrieved when

(i) $\quad \dfrac{\lambda_2}{\lambda_1} = 1$

(ii) $\quad$ De $\to 0$

and that as De $\to \infty$ the expressions become

$$\tau \to -\frac{2\eta K}{r^2}\begin{pmatrix} +1 - \dfrac{\lambda_2}{\lambda_1}\sin^2\theta & + \dfrac{\lambda_2}{\lambda_1}\cos\theta\sin\theta \\[2ex] \dfrac{\lambda_2}{\lambda_1}\cos\theta\sin\theta & \dfrac{\lambda_2}{\lambda_1}\cos^2\theta \end{pmatrix}$$

(3.35)

$$p \to \frac{\eta K}{r^2} - \frac{\lambda_2}{\lambda_1}\frac{2\eta K}{r^2}\cos^2\theta$$

(3.36)

The interesting point in the high Deborah number limit for the Oldroyd B fluid is that close to the origin the flow does not become solely a second Newtonian flow. There is also a contribution to the stress and pressure fields from the Maxwell element, indicated by the presence of terms not involving λ_2/λ_1. This belies the normally accepted behaviour of the Oldroyd B fluid, also known as the Upper Convected Jeffreys Fluid, as given, for example by Petrie [59]; the 'initial response' or high Deborah limit may not be just that of a 'liquid' it may also include elements of 'solid' behaviour.

3.2 Brief Investigation of the Possibility of Further Solutions

Having obtained a solution for the flow in a converging

channel of such a simple kinematic nature, an attempt was made to obtain

further solutions by changing the geometry of the flow to a cone

or by changing the type of viscoelastic fluid. Two examples are

given below of the failure to obtain such solutions for the wedge

flow of a corotational GLV-EF defined on page 339 of [48] and the

convergent cone flow of an upper convected GLV-EF. These negative

results suggest that the solution of section 3.1 is isolated and does

not belong to a family of such solutions with simple kinematics.

Corotational GLV-EF in wedge

Assuming the kinematics are given by (2.6) the corotating

strain rate tensor is calculated as

$$
\dot{\Gamma} = \frac{1}{r^2(1+ \frac{2fs}{r^2})}
\begin{pmatrix}
f\cos\beta(s) + f'\sin\beta(s) & f\sin\beta(s) - f'\cos\beta(s) & 0 \\
f\sin\beta(s) - f'\cos\beta(s) & -f\cos\beta(s) - f'\sin\beta(s) & 0 \\
0 & 0 & 0
\end{pmatrix}
$$

$$(3.37)$$

where $\quad \beta(s) = \frac{f'}{2f} \ell n(1 + \frac{2fs}{r^2})$.

After substitution of $\dot{\Gamma}$ in the stress equilibrium equation

(3.3) the resulting expressions are not integrable in a closed form.

However, if $\frac{\partial^2 p}{\partial r \partial \theta}$ is calculated from the r and θ components of

(3.3) the resulting expressions should be identical. As can be

verified after a lengthy calculation they are not equal for any

function, f, except trivially for f a constant.

Upper convected GLV-EF in converging cone

Let the kinematics be given by a non-zero radial component of the velocity

$$v_r = - \frac{f(\theta)}{r^2} \qquad v_\theta = v_\phi = 0 \qquad (3.38)$$

which satisfies the mass conservation equation (3.2). It is readily shown that the strain tensor is given by

$$\gamma_{[0]} = \begin{pmatrix} 1-(1 + \frac{3fs}{r^3})^{4/3} - (1 + \frac{3fs}{r^3})^{-2/3} \frac{f'^2 s^2}{r^6} & (1 + \frac{3fs}{r^3})^{-2/3} \frac{f'}{r^3} & 0 \\ (1 + \frac{3fs}{r^3})^{-2/3} \frac{f's}{r^3} & 1-(1 + \frac{3fs}{r^3})^{-2/3} & 0 \\ 0 & 0 & 1-(1+ \frac{3fs}{r^3})^{-2/3} \end{pmatrix}$$

$$(3.39)$$

Substitution of (3.39) into the momentum conservation equation produces three expressions for the derivatives of the pressure, which upon integration results in three expressions for p to be satisfied simultaneously

$$p = - \int_0^\infty M(s) \{2(\frac{f'}{3f})^2 + 2- \frac{f''}{3f} - \frac{f'}{3f} \cot\theta - (1 + \frac{3fs}{r^3})(1 +(\frac{f'}{3f})^2) \} (1 + \frac{3fs}{r^3})^{1/3} ds + f_1(\theta) \qquad (3.40)$$

$$p = - 2\int_0^\infty M(s) (1 + \frac{3fs}{r^3})^{1/3} ds + f_2(r) \qquad (3.41)$$

$$p = f_3(r,\theta) \qquad (3.42)$$

where f_1, f_2, f_3 are arbitrary functions of their arguments.

However, these equations are incompatible and because of the term involving

$$(1 + \frac{3fs}{r^3})^{4/3}$$

in (3.40), no such p exists except trivially for f a constant.

3.3   Comparison with Experiment

Han and Drexler have published results of experimental measurements of stress in a $180°$ wedge using a birefringence technique. They consider the shear stress and normal stress difference in a rectangular Cartesian co-ordinate system. Hence the results of section 3.1   must be converted to $\tau_{xx} - \tau_{yy}$ and τ_{xy} from $\tau_{rr} - \tau_{\theta\theta}$ and $\tau_{r\theta}$ to enable a comparison to be made. They also use a different sign convention in their definition of $\underset{\sim}{\tau}$ from that used in (3.4); therefore let $\underset{\sim}{\bar{s}} = - \underset{\sim}{\tau}$. The transformation required is readily calculated as

$$\bar{s}_{xx} - \bar{s}_{yy} = (\tau_{rr} - \tau_{\theta\theta})\cos2\theta - 2\tau_{r\theta}\sin2\theta$$

$$\bar{s}_{xy} = - \tau_{r\theta}\cos2\theta - \tfrac{1}{2}(\tau_{rr} - \tau_{\theta\theta})\sin2\theta$$

(3.43)

in which the y-axis corresponds to $\theta = 0$. For the purposes of comparison the stresses for a Maxwell Fluid are used as in (3.22). Substitution of $\tau_{rr} - \tau_{\theta\theta}$ and $\tau_{r\theta}$ in (3.43) obtains

$$\bar{s}_{xx} - \bar{s}_{yy} = - \frac{2nK}{r^2}(\cos2\theta + H(\xi)\cos4\theta)$$

(3.44)

$$\bar{s}_{xy} = \frac{nK}{r^2}(\sin2\theta + H(\xi)\sin4\theta)$$

Finally, all variables are written in a dimensionless form

$$x = X(2\lambda K)^{\frac{1}{2}} , \quad y = Y(2\lambda K)^{\frac{1}{2}}$$

<div align="right">(3.45)</div>

$$\bar{s}_{xx} - \bar{s}_{yy} = \frac{\eta}{\lambda} (S_{XX} - S_{YY}) , \quad s_{xy} = \frac{\eta}{\lambda} S_{XY}$$

Figs. 3.4 and 3.5 show curves of constant $S_{XX} - S_{YY}$ and S_{XY} respectively for half of the stress field; the line $x = 0$ is a line of symmetry, since $S_{XX} - S_{YY}$ is an even function of θ and S_{XY} is an odd function of θ. The x-axis corresponds to a solid boundary and the origin to the position of the sink. Values of the dimensionless stresses are indicated alongside each curve. Also shown in figs. 3.4 and 3.5 are the corresponding constant stress curves for a Newtonian fluid obtained by setting H identically unity in equations (3.44). The main features of the two sets of curves are similar. The greatest differences occur near the origin and close to the Y axis or the centreline of the flow field. Figs. 3.6 and 3.7 show replotted versions of figs. 13 and 14 of Han and Drexler [7] for a polystyrene melt, Dow Chemical Styron 686. In Figs. 3.6 and 3.7 the fluid exits via a parallel-sided channel as indicated by the line drawn at $X = 0.192$. Again only half the stress field is shown. In order to draw these curves in the dimensionless variables of (3.45) values of η and λ were estimated from viscometric flow data for the melt Styron 686 as reported in [60]. Both parameters were taken as the limiting values at vanishing shear rate:

$$\eta = \eta_0 = 3 \times 10^5 \text{ poise}$$

$$\lambda = \lim_{\dot{\gamma} \to 0} \frac{N_1(\dot{\gamma})}{2\dot{\gamma}^2 \eta_0} = 2.5 \text{ secs}$$

where N_1 is the normal stress difference in steady shear flow.
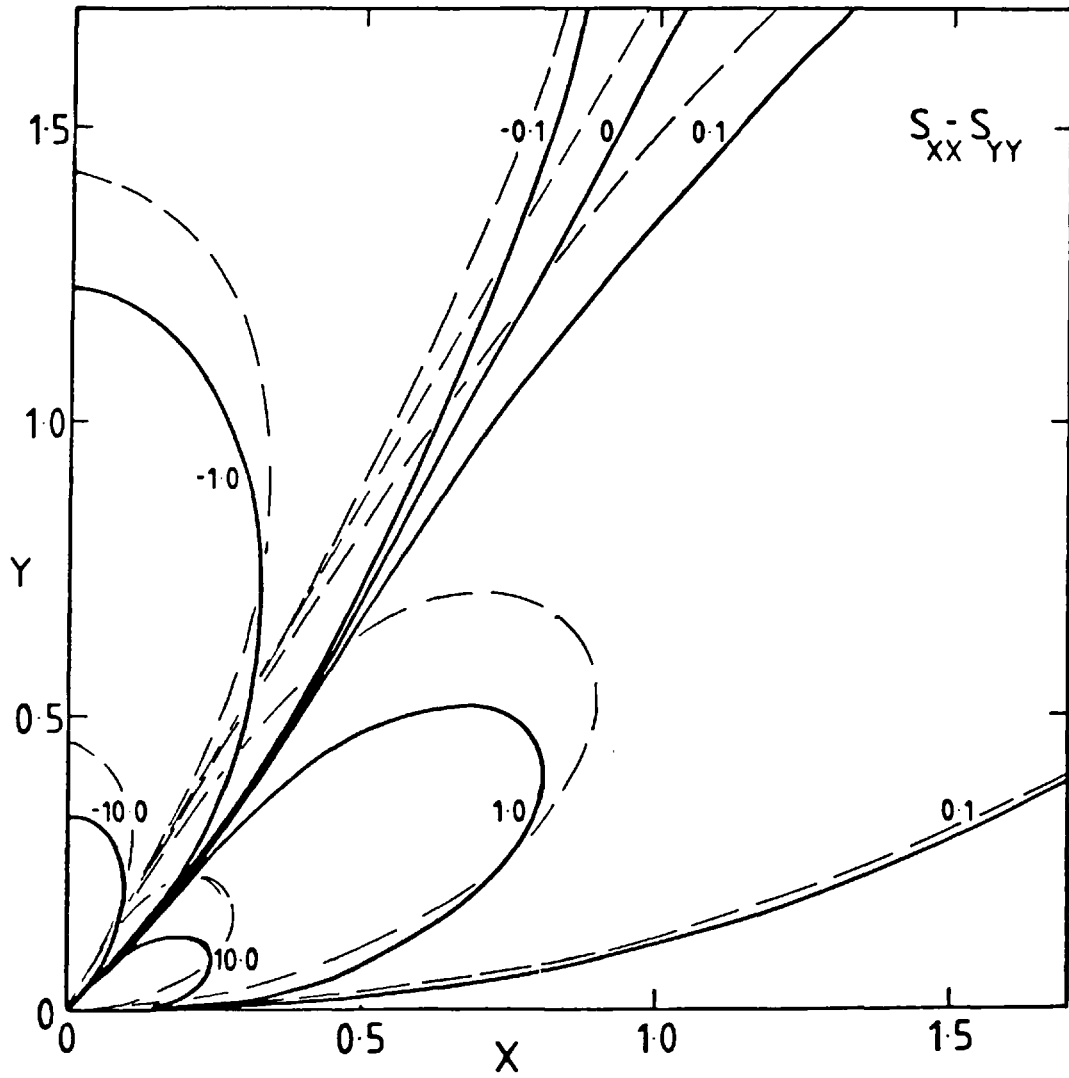
Fig. 3.4 Graph of curves of constant $S_{XX}-S_{YY}$, theoretical
values
(———) Maxwell Fluid
(- - - - -) Newtonian Fluid
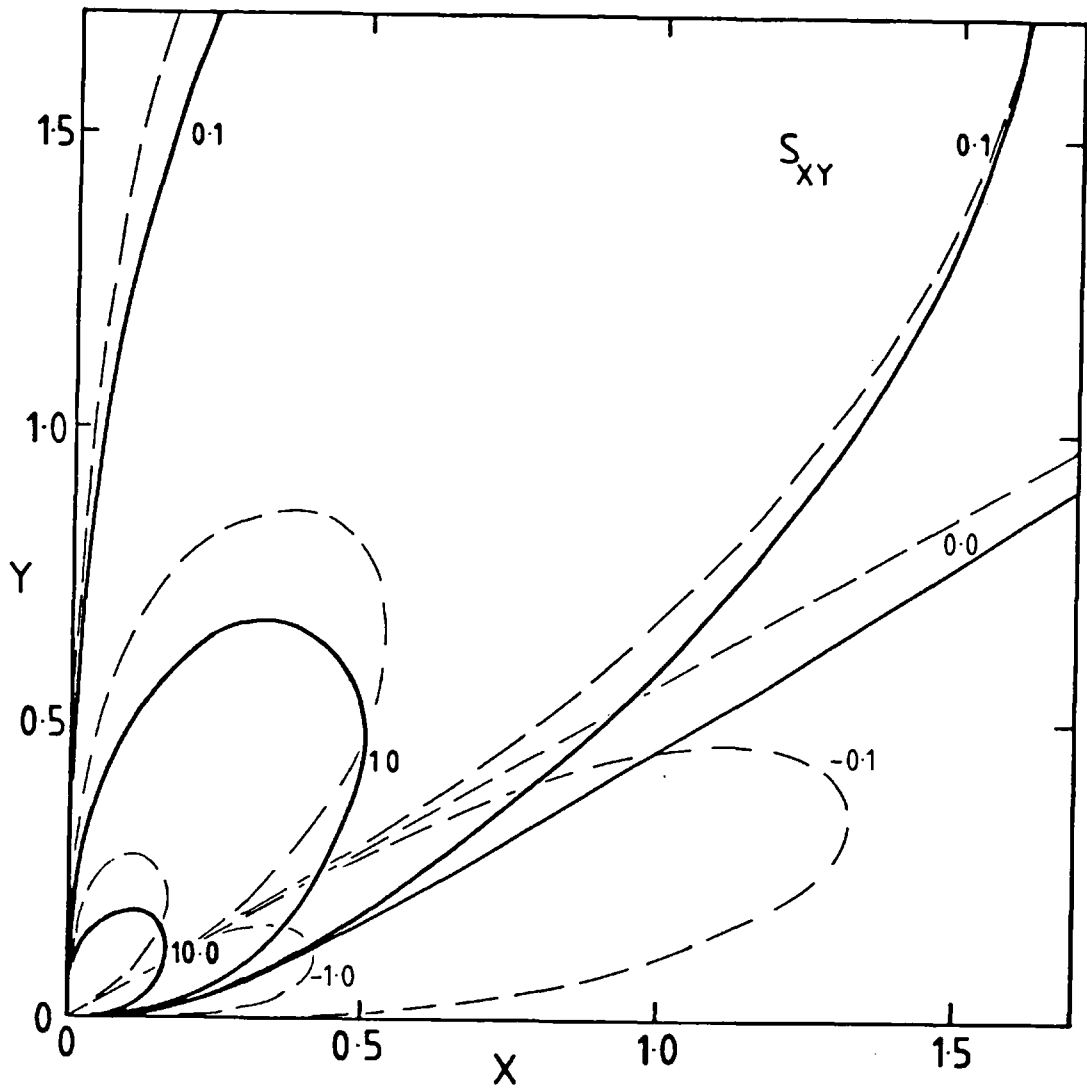
Fig. 3.5 Graph of curves of constant S_{XY}, theoretical values

(———) Maxwell Fluid

(–––––) Newtonian Fluid

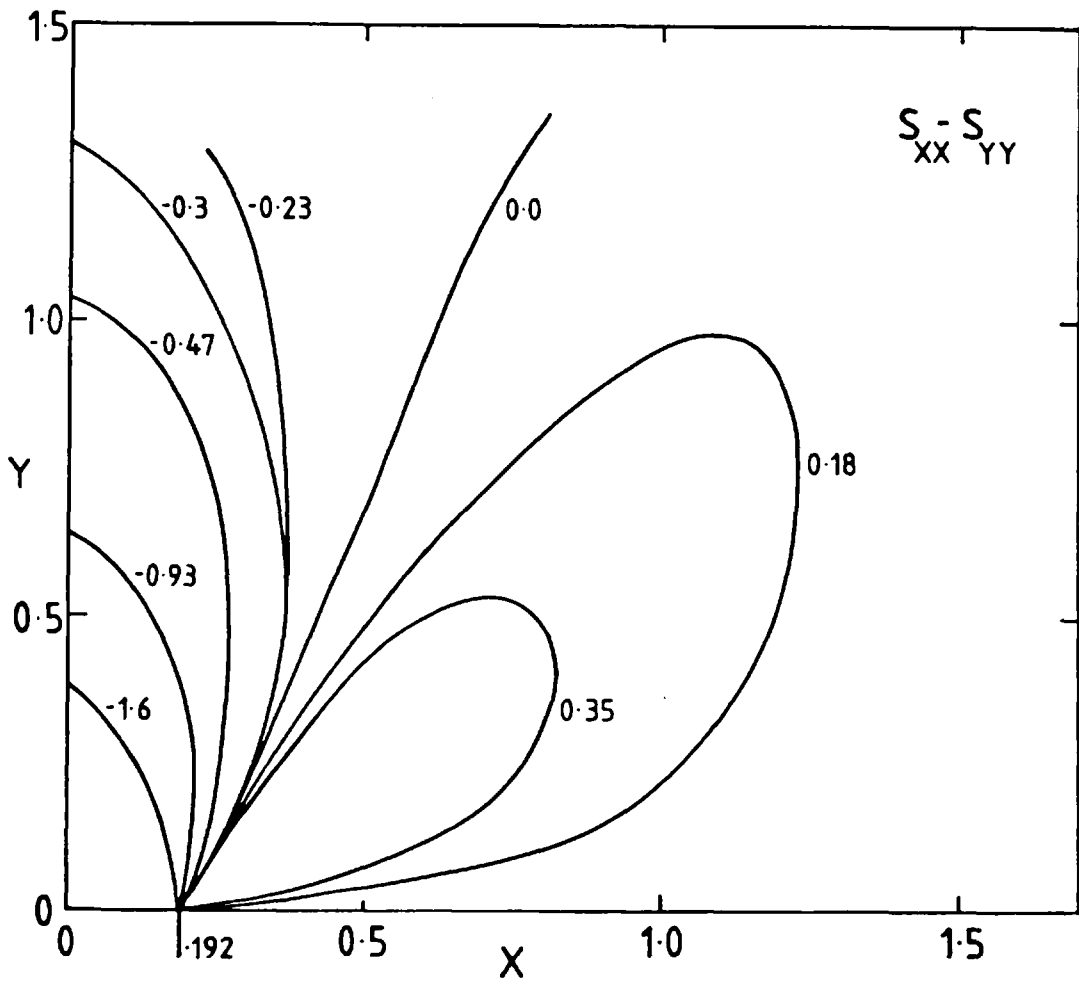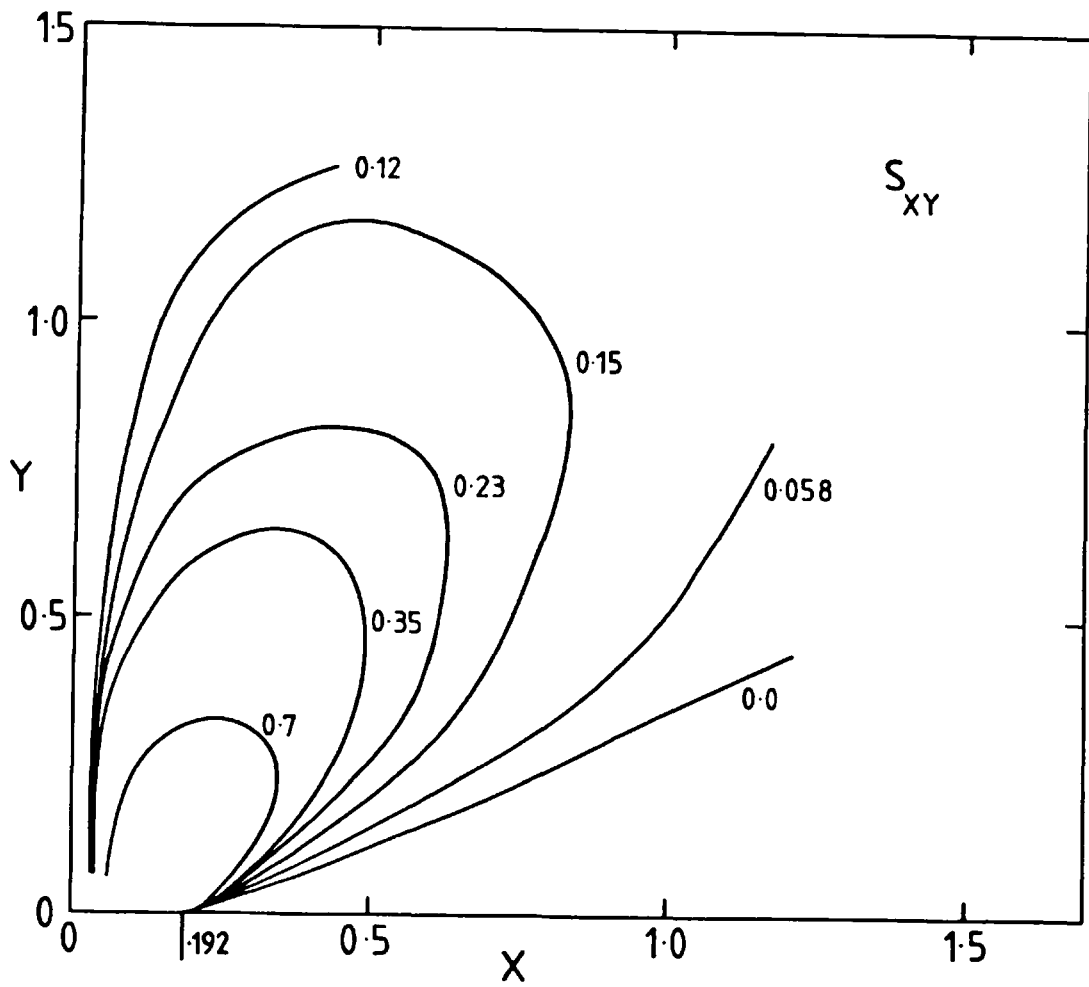Fig. 3.6 Graph of curves of constant $S_{XX}-S_{YY}$, experimental values for a polystyrene melt.

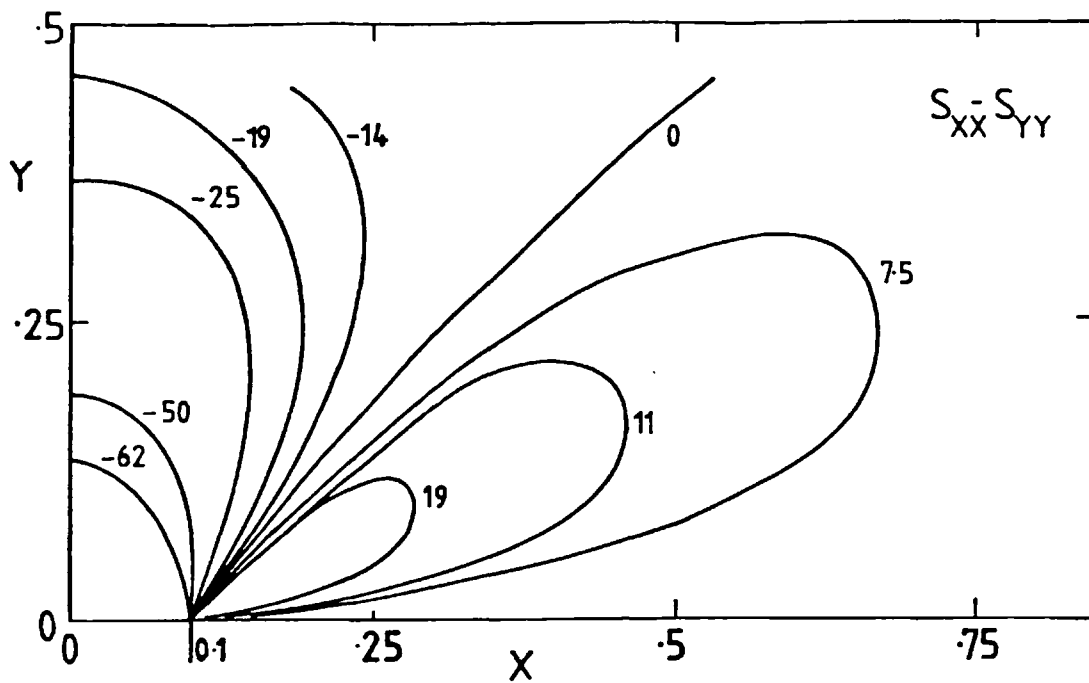Fig. 3.7 Graph of curves of constant S_{XY}, experimental values
for a polystyrene melt.

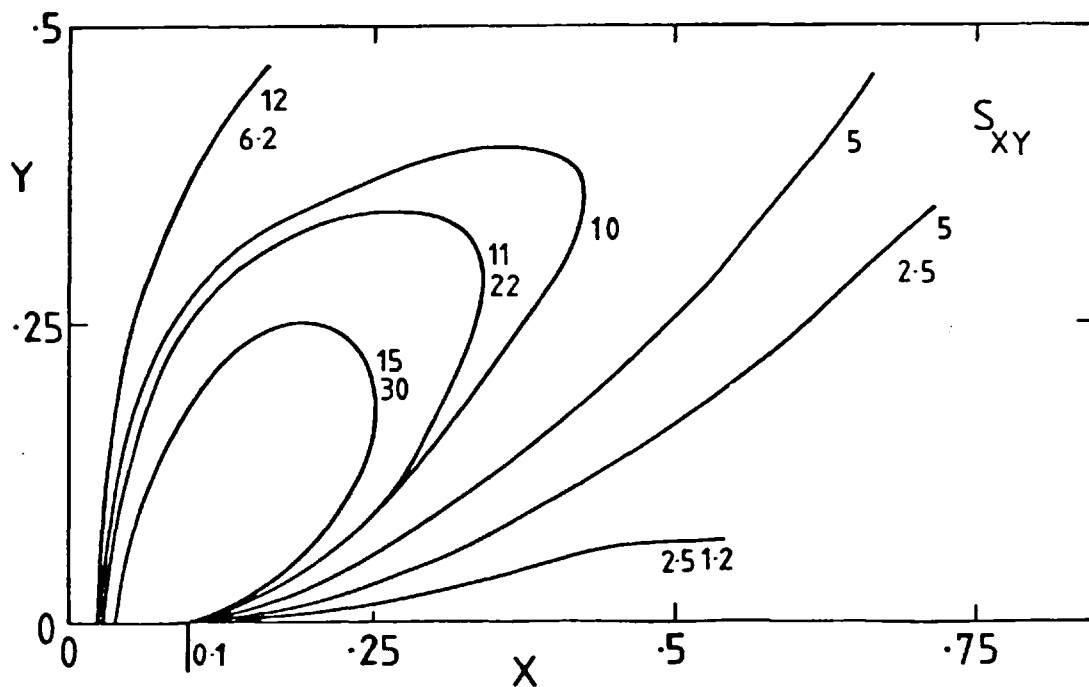Fig. 3.8 Graph of curves of constant $S_{XX}-S_{YY}$, experimental values for a HDPE melt.

Fig. 3.9 Graph of curves of constant S_{XY}, experimental values for a HDPE melt.

Qualitatively, the agreement between the theoretical and experimental curves in Figs. 3.4-3.7 is good and the values of the stresses are of the same order of magnitude. In fact, the theoretical results predict stresses approximately a factor of 3 larger than the reported experimental values. A quantitative comparison, however, is of limited value primarily because of the finite width of the exit used for the experimental results and the inadequacy of any model of the UCGLV-EF type in describing observed melt behaviour. Good qualitative agreement is also achieved with the experimental results for two other melts, high density polyethylene and polypropylene, as reported in Han and Drexler [7]. Figs. 3.8 and 3.9 show replotted versions of their figs. 11 and 12 for a HDPE melt with $\eta_0 = 2 \times 10^6$ poise and $\lambda = 50$ secs. The scaling on the axes is different from that of figs. 3.4-3.7 but a comparison is not difficult. Clearly the dimensionless stresses involved in the flow of HDPE are an order of magnitude greater than those for PS and the experimental stresses for HDPE are a factor of about 3 larger than the theoretical predictions.

3.4   Discussion

The exact solution obtained in section 3.1 can be used to study the convergence or otherwise of the series solution obtained by Strauss [25] and the equivalent perturbation solution of Black [24], as discussed in Chapter 1. These solutions are inverse coordinate or indirect expansions which, according to Van Dyke [61] are usually asymptotic diverging series. To facilitate further discussion, the dimensionless variables of section 3.3 are introduced;

$$S = \frac{\lambda}{\eta} \tau \qquad \overline{r} = (2\lambda K)^{-\frac{1}{2}} r \qquad \overline{t} = t/\lambda$$

$$P = \frac{\lambda}{\eta} P \qquad \overline{v} = (\frac{\lambda}{2K})^{\frac{1}{2}} v \qquad . \quad \overline{\nabla} = (2\lambda K)^{\frac{1}{2}} \nabla \qquad (3.46)$$

where $-K/r$ is the centreline velocity as $r \to \infty$.

Using the new variables, the set of equations governing the motion become

$$\overline{\nabla}.\overline{v} = 0 \qquad (3.47)$$

$$\overline{\nabla}.\overline{\pi} = 0 \qquad (3.48)$$

$$\overline{\pi} = P\delta + S \qquad (3.49)$$

$$S + S_{(1)} = -[\overline{\nabla}\ \overline{v} + (\overline{\nabla}\ \overline{v})^{T}] = -\gamma_{(1)} \qquad (3.50)$$

where

$$S_{(1)} = \frac{\partial S}{\partial t}, + \overline{v}.\overline{\nabla}S - S.\overline{\nabla}\ \overline{v} - (\overline{\nabla}\overline{v})^{T}.S \qquad (3.51)$$

in which the constitutive equation for the Maxwell fluid has been written in its differential form. Because the superfix $^{-}$ is cumbersome it is omitted in what follows with the understanding that all variables are to be treated as dimensionless.

Define a stream function $\psi(r,\theta)$ identically satisfying (3.47) by

$$\psi_{\phi} = rv_{r} \qquad \psi_{r} = -v_{\theta} \qquad (3.52)$$

Because of the symmetry and the normalisation of the velocity field the boundary conditions on ψ are

$$\psi(r,\alpha) = (-\psi(r,-\alpha)=) = \frac{Q}{4K}$$

$$\psi(r,\theta) = -\psi(r,-\theta)$$

$$\psi_\theta(r,\alpha) = \psi_\theta(r,-\alpha) = 0 \qquad (3.53)$$

By expanding the exact solution (3.22,3.23) in powers of $1/r$, Strauss' result for the special case of $\alpha = \pi/2$ is retrieved for slow flow. However this necessarily involves expanding the term $\xi e^\xi E_1(\xi)$ as $\xi \to \infty$. This is given in [58] as

$$\xi e^\xi E_1(\xi) \sim 1 - 1/\xi + 2/\xi^2 - \dots + \frac{(-1)^i i!}{\xi^i} + \dots \qquad (3.54)$$

which clearly diverges as $i \to \infty$ given any value of ξ. This means that (1.14) which is the form of Strauss' solution is an asymptotic diverging series and is valid only far from the origin or close to the solid boundaries. In fact the error after n terms in the expansion (1.14) can be shown to be

$$0 \left(\frac{\psi_0{}'(\theta)\psi_{n-1}{}'(\theta)}{r^{2n+2}} \right)$$

an expression similar in form to the local Deborah number defined in (3.20). Therefore, serious doubt is cast on the meaning of fig.1.4 and Strauss' figs. 7-10 [25] which show recirculating streamlines not far from the origin and in the centre of the flow field where, it has just been shown, an indirect expansion is invalid.

A direct expansion may be the solution to this difficulty. The direct expansion for $\alpha = \pi/2$ is available from the exact solution. The stream function has only the first order term

$$\psi = \psi_0(\theta) \qquad (3.55)$$

whilst the stress depends upon the expansion of the function $H(\xi)$

for small ξ; H defined in (3.24)

$$H = \xi + \xi^2(\gamma_e + \ell n\xi) + \xi^3(\gamma_e - 1 + \ell n\xi) + O(\xi^4 \ell n\xi, \xi^4)$$

$$(3.56)$$

where $\gamma_e \approx 0.577$ is Eulers constant [58].

In terms of the dimensionless variables, $\xi = r^2/\cos^2\theta$. Using (3.56) the direct expansion of the stress tensor in (3.22) suitably non-dimensionalised is

$$S_{rr} = -1/r^2 + \tan^2\theta + r^2\tan^2\theta\sec^2\theta(\gamma_e + \ell nr^2 - \ell n\cos^2\theta) + \ldots$$

$$S_{r\theta} = -\tan\theta - r^2\tan\theta\sec^2\theta(\gamma_e + \ell nr^2 - \ell n\cos^2\theta) + \ldots$$

$$S_{\theta\theta} = 1 + r^2\sec^2\theta(\gamma_e + \ell nr^2 - \ell n\cos^2\theta) + \ldots$$

$$(3.57)$$

These expansions suggest that for $\alpha \neq \pi/2$ and $2\alpha < 257.5°$ a series solution is attempted with the form

$$\psi = \psi_0 + r^2\psi_1 + r^4(\psi_2\ell nr + \psi_3) + \ldots$$

$$S_{rr} = a_0/r^2 + a_1 + r^2(a_2\ell nr + a_3) + \ldots$$

$$S_{r\theta} = b_0/r^2 + b_1 + r^2(b_2\ell nr + b_3) + \ldots$$

$$S_{\theta\theta} = c_0/r^2 + c_1 + r^2(c_2\ell nr + c_3) + \ldots$$

$$(3.58)$$

where the coefficients ψ_i, a_i, b_i, c_i are functions of θ only. The series is substituted into (3.51) and the curl of (3.48) i.e. $\nabla \times \nabla.S = 0$ with the sole boundary condition that $\psi_i(\theta)$ are odd functions. The solutions for the coefficients are obtained by equating like powers of r, and are given below up to the third term.

$$a_0 = \text{constant} \qquad (3.59)$$

$$b_0 = c_0 = 0 \qquad (3.60)$$

ψ_0 is undetermined.

$$a_1 = -q - b_1' \qquad q \text{ a constant} \qquad (3.61)$$

$$b_1 = [\theta a_0 - 4a_0\psi_1 - 2\psi_0(q+1)]/(2\psi_0') \qquad (3.62)$$

$$c_1 = +1 \qquad (3.63)$$

ψ_1 is undetermined.

$$a_2 = \frac{2a_0\psi_2'}{\psi_0'} - \frac{2\psi_0''a_0\psi_2}{\psi_0'^2} - \frac{\psi_0''^2}{4\psi_0'^3} \qquad (3.64)$$

$$b_2 = -\frac{4a_0\psi_2}{\psi_0'} - \frac{\psi_0''}{2\psi_0'^2} \qquad (3.65)$$

$$c_2 = -\frac{1}{\psi_0'} \qquad (3.66)$$

$$\psi_2 = \frac{q_1\psi_0'\sin4\theta}{8a_0} + \int^\theta \frac{\psi_0'(\theta)}{8\psi_0^3(t)} \sin4(\theta-t)\{\psi_0^{iv} - 2\psi_0'' -$$

$$\frac{3\psi_0''\psi_0'''}{\psi_0'} + \frac{3\psi_0''^3}{2\psi_0'^2}\} \, dt \quad \text{evaluated at } t$$

q_1 a constant $\qquad (3.67)$

The undetermined functions arise from degeneracies in the sets of four simultaneous equations for each order. Such a situation is completely unexpected particularly since it is known what ψ_0 and ψ_1 are from the exact solution. It would appear that the direct expansion for $\alpha = \pi/2$ as in (3.57) is not completely retrievable although as can be verified, the form is consistent with (3.59-3.67). The reason for this arbitrariness is not clear, though it may have something to do with the differential formulation of the constitutive equation.

The direct expansion, although it may have an infinite radius of convergence, becomes increasingly inaccurate as the wall is approached since $b_1, a_2, b_2, c_2, \psi_2$ etc. involve inverse powers of ψ_0'. If ψ_0' satisfies the no-slip boundary condition then $\psi_0'(\alpha) = 0$, otherwise the solution is inaccurate close to the wall even for ψ_0'.

However assuming that the first order terms have the correct

r dependence (they have for $\alpha = \pi/2$ and there is no reason to assume

otherwise for $\alpha = \pi/2$) then $\psi_0(\theta)$ must be accurate as the first term

for most of the flow field, because it determines the flux, which

must be independent of r. It is not essential that ψ_0 satisfies

the no-slip boundary condition but it should be valid within a

region bounded by

$$\frac{r^2}{\psi_0{}'} = 1/D \qquad D \text{ a constant.} \qquad (3.68)$$

Again this has a form similar to the local Deborah Number of (3.20).

Also, consideration of the exact solution shows that along the centre-

line ($\theta = 0$) $\tau_{rr} \alpha \ 1/r^2$ for all values of r. These two observations

are the basis of the following conjecture.

Conjecture

Part I. The first terms of the direct and indirect

expansions of stream functions ψ_0, Ψ_0 respectively

are to be matched on the curve of minimum error

of the indirect expansion. Thus

$$\psi_0(\theta) = \Psi_0(\theta) \text{ on } \frac{\Psi_0(\theta)}{r^2} = D \to 0 \qquad (3.69)$$

Part II. The stress component τ_{rr} along the

centreline is proportional to $1/r^2$ for all $r \epsilon [0, \infty)$

A sketch of the curve in Part I is shown in Fig. 3.10
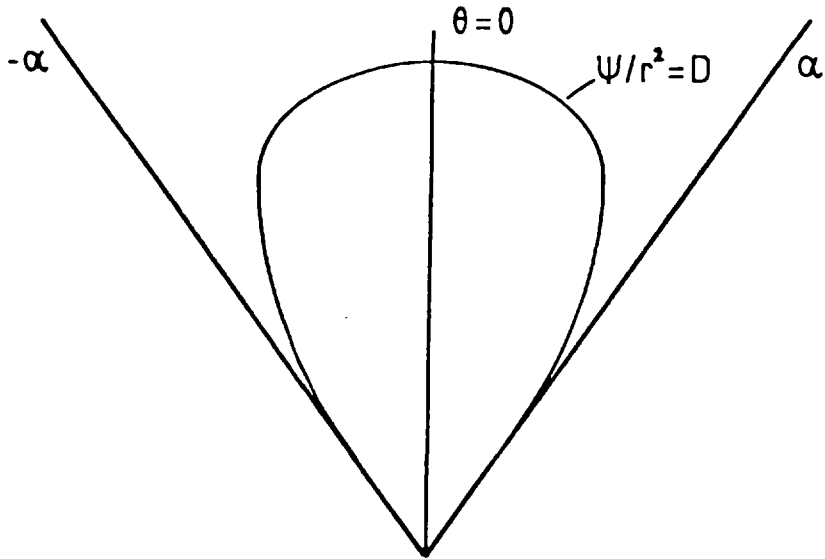
Fig. 3.10 Sketch of the matching region.

Since the curve passes through all values of θ between $\pm\alpha$, Part I implies that

$$\psi_0(\theta) = \Psi_0(\theta) \tag{3.70}$$

Part II will enable some of the arbitrary constants a_0, q and q_1 to be determined.

In fact the additional information from the conjecture gives a_0 and ψ_0

$$a_0 = \frac{2Q}{K} \frac{\sin^2\alpha}{\sin 2\alpha - 2\alpha\cos 2\alpha} \tag{3.72}$$

$$\psi_0 = \frac{Q}{4K} \frac{\sin 2\theta - 2\theta\cos 2\alpha}{\sin 2\alpha - 2\alpha\cos 2\alpha} \tag{3.72}$$

Also using (3.61) evaluated on the centreline and Part II it is found that $\psi_1'(0) = 0$ but otherwise ψ_1 remains undetermined. Of course explicit formulas for a_2, b_2, c_2, ψ_2 could be worked out but it would not achieve much until the second order terms are determined.

CHAPTER 4

APPROXIMATION METHOD FOR CONE & WEDGE FLOW

The limitations of indirect (coordinate) expansions for the

solution of flows through converging wedges have been discussed in

Chapter 3. The situation for flow in cones will be similar. There

is a considerable difference in the flow field obtained from an

indirect expansion of a Maxwell fluid and a third of fourth order fluid

(see section 1.2). In addition to this, there seem to be subtle

mathematical difficulties to be overcome before direct expansions

become useful (see section 3.4). For these reasons a different

approach is explored in this Chapter which uses the Extensional Primary

Field approximation as a starting point. In fact, it turns out

that the EPF is a type of direct expansion in which only the first

term is used but which is specified beforehand.

The kinematical justification for the EPF is from experimental

observation of die-entry flows, the main features of which are

described in section 1.2. Provided that the flow remains slow,

a condition satisfied except for high fluxes of polymer solutions,

then most of the flow field in the converging region has radial

streamlines, i.e. $v_\theta \ll v_r$ almost everywhere. More important, most

of the outflow comes from the central portion of the flow whether

recirculating vortices are formed or not. This means that the

velocity field is proportional to $1/r$ or $1/r^2$ for a wedge or cone,

in which the coordinate systems are polar or spherical, respectively.

Furthermore, there is considerable evidence that over most of a

central cone region there is little variation in the magnitude of

the velocity across the cone region.

Consider now the whole flow field which is illustrated

schematically in fig. 4.1, Part a) shows flow towards the apex of

a cone or wedge with half angle Θ . If the radial velocity component

is smooth as in part b) (i), then $r^{-1}\partial v_r/\partial\theta$ is of the same order of

magnitude as $\partial v_r/\partial r$ over most of the flow region, and so neither

simple shear flow, nor irrotational flow are suitable approximations.

If however, a cone region, where there is little radial variation in

v_r, is assumed to arise so that $\partial v_r/\partial r \gg r^{-1}\partial v_r/\partial\theta$, then there must

also be a strongly sheared self-lubricating layer close to the wall

with $r^{-1}\partial v_r/\partial\theta \gg \partial v_r/\partial r$, as in part (b) (ii). Thus the flow

may be approximated by a simple shear flow within $\theta_I \leq |\theta| \leq \Theta$, and

an irrotational, sink flow within $0 \leq |\theta| \leq \theta_I$. (The velocity

profile in part (b) (ii) should not be taken as invariable, as it

is possible that recirculation occurs in the layer implying a positive

radial velocity in the neighbourhood of the wall). In this manner,

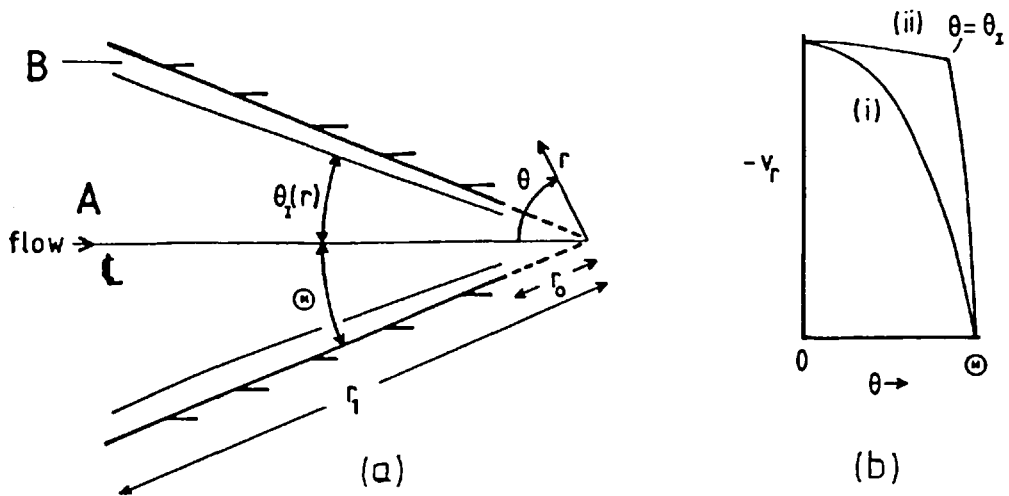the no-slip boundary condition at the wall can be satisfied.

Fig. 4.1 (a) Geometry of converging wedge or cone of half
angle Θ with polar coordinates (r,θ). A - core
region; B - self-lubricating region. $\theta_I(r)$ refers
to position of interface between lubricating and
core regions. (b) Radial velocity component profiles
as functions of θ (at some given r) : (i) smooth
profile with no lubrication; (ii) kinked profile
with sharp change in shear rate $\dfrac{1}{r}\dfrac{\partial v_r}{\partial \theta}$ at $\theta=\theta_I(r)$,
indicating lubrication effect.

The dynamic justification for the EPF, or equivalently, for the core region,

has been discussed in section 1.3 in terms of the Trouton ratio, $N_{T_r} \gg 1$.

The assumed kinematics for the extended model require a stronger

condition for dynamic consistency. Roughly, it is required that the

extensional stresses at a particular strain rate are much greater than

the shear stresses at a shear rate possibly an order of magnitude

greater than the strain rate. In crude terms this is

$$N_{T_r} \gg 1/(\Theta-\theta_I) \gg 2/\pi \qquad (4.1)$$

Data for the stresses in uniaxial extension of two rubber compounds

have been given in Chapter 2. Although extremely high strains were

recorded, no steady state was reached, which means that a viscosity

in uniaxial extension cannot be measured and the Trouton ratio intrin-

sically has no meaning. However, a measure of the stress likely in

extensional flow is given by the maximum stress achieved in the experiment. In turn, this will be taken as a measure of the stresses achieved in the sink flows occurring in the cone region.

For the shear layer, the stress involved either in the start-up of simple shear, or at steady values, can be taken as representative. From the experimental data shown in figs. 2.14-2.17 and particularly fig. 2.18, it can be seen that the extensional stresses are one or two orders of magnitude greater than the shear stresses at comparable deformation rates. This represents sufficient dynamical justification.

To a first approximation the interface θ_I separating the flow field will be treated as a streamline, i.e. there is no inter-change between fluid undergoing simple shear and fluid undergoing sink flow. In sections 4.1 and 4.2 explicit calculations are presented in which the fluid in the cone is described by a UCMF (Upper Convected Maxwell Fluid) and the fluid in the shear layer by the Ellis Viscosity Equation. Such a model where the two regions are not linked by the same constitutive equation will be termed a Two-Fluid Model (2FM). In section 4.3, the same calculations are done this time for the naive rheological model of section 2.6. Here the two regions are linked by the same constitutive equation. Such a model will be termed a Two-Zone Model (2ZM). The 2ZM does not rely upon θ_I being a streamline and so should open up possibilities of calculating higher order terms in the approximation method. The term 2FM, is only meant to imply that different rheological aspects of what may well be one single fluid are being considered.

4.1   Wedge Flow

The equations of continuity and stress equilibrium with respect to a polar coordinate system for steady, planar flow in a wedge (r,θ), with corresponding velocity components (u,v) are

$$\frac{1}{r}\frac{\partial}{\partial r}(ru) + \frac{1}{r}\frac{\partial v}{\partial \theta} = 0 \tag{4.2}$$

$$\frac{1}{r}\frac{\partial}{\partial r}[r(\tau_{rr}-\tau_{\theta\theta})] + \frac{1}{r}\frac{\partial}{\partial \theta}\tau_{r\theta} + \frac{\partial}{\partial r}(p+\tau_{\theta\theta}) = 0 \tag{4.3}$$

$$\frac{1}{r^2}\frac{\partial}{\partial r}(r^2\tau_{r\theta}) + \frac{1}{r}\frac{\partial}{\partial \theta}(p+\tau_{\theta\theta}) = 0 \tag{4.4}$$

The boundary conditions for no slip at the wall, i.e. at $\theta = \pm\Theta$ require

$$u(r,\pm\Theta) = v(r,\pm\Theta) = 0 \tag{4.5}$$

In the steady state, the flux per unit width $2\bar{Q}$, of fluid crossing every section of the wedge must be the same, namely

$$\bar{Q} = \int_0^\Theta rudr \tag{4.6}$$

The convention chosen is that the flux in the converging direction is negative.

The flow is now separated by an interface θ_I defined at $\theta=\theta_I$. At this stage of the approximation θ_I is considered to be constant, locally and at most slowly varying with radial distance; thus it is required that

$$r\frac{\partial \theta_I}{\partial r} \ll 1 \tag{4.7}$$

The flow within the region $|\theta| \leq \theta_I$ is assumed to be a sink flow, locally, with a velocity field satisfying the continuity equation (4.2)

given by

$$\hat{u} = -\frac{K}{r}, \quad \hat{v} = 0 \qquad K \text{ a constant} \qquad (4.8)$$

Quantitites designated by '$\hat{}$' refer to the cone but will only be used where possible confusion with the shear layer may arise. The formal boundary conditions at the interface are the continuity of velocity and the normal and tangential tractions. Neglecting the possible slight curvature of θ_I, these are

$$\hat{u} = u, \quad (\hat{v} = v) \qquad (4.9)$$

$$\hat{p} + \hat{\tau}_{\theta\theta} = p + \tau_{\theta\theta} \qquad (4.10)$$

$$\hat{\tau}_{r\theta} = \tau_{r\theta} \qquad (4.11)$$

all evaluated at $\theta = \theta_I$. Because the core is a sink flow, $\hat{\tau}_{r\theta}$ will vanish identically. However, it is to be expected that $\tau_{r\theta} \neq 0$. So to the first approximation (4.11) will not be satisfied. However, a measure of the accuracy of the method is provided by the ratio of the tractions in (4.10) and (4.11). Thus it will be desirable for

$$C = \left.\frac{|\tau_{r\theta}|}{|\hat{p} + \hat{\tau}_{\theta\theta}|}\right|_{\theta=\theta_I} = \left.\frac{|\tau_{r\theta}|}{|p + \tau_{\theta\theta}|}\right|_{\theta=\theta_I} \ll 1 \qquad (4.12)$$

Since θ_I is a streamline there is an extra kinematic condition on the flux which is sufficient to determine a unique solution. If the flux in the cone is $2\hat{Q}$ and the flux in the shear layer is $2Q$, then

$$\bar{Q} = \hat{Q} + Q, \qquad \hat{Q}, Q \text{ are constant} \qquad (4.13)$$

$$\hat{Q} = -K\theta_I \qquad (4.14)$$

$$Q = \int_{\theta_I}^{\Theta} = ru \, dr \qquad (4.15)$$

The effect of the cone flow on the shear layer will be shown to be through $\partial(\hat{p}+\hat{\tau}_{\theta\theta})/\partial r$ determined at the interface from (4.10), and also through the radial velocity of the interface, $-K/r$.

The expression $\partial(\hat{p}+\hat{\tau}_{\theta\theta})/\partial r$ for the UCMF, equations (3.5) and (3.21) can be calculated, first by evaluating the strain tensor for the line sink kinematics of (4.8):

$$\hat{\gamma}_{[0]} = \begin{pmatrix} -\dfrac{2Ks}{r^2} & 0 & 0 \\[3mm] 0 & (1+\dfrac{2Ks}{r^2})^{-1} & 0 \\[3mm] 0 & 0 & 0 \end{pmatrix}, \quad s = t=t' \tag{4.16}$$

The stress tensor follows by integration of (3.5)

$$\hat{\tau}_{rr} = -\frac{\hat{\mu}}{\lambda\xi}$$

$$\hat{\tau}_{\theta\theta} = \frac{\hat{\mu}}{\lambda}(1-\xi e^{\xi}E_1(\xi)) \tag{4.17}$$

in which all other stress tensor components vanish, $\xi = r^2/(2\lambda K)$ is a dimensionless *local* Deborah Number and $\hat{\mu}$ is the viscosity constant equivalent to η in (3.21). The required expression is

$$\frac{\partial}{\partial r}(\hat{p}+\hat{\tau}_{\theta\theta}) = -\frac{2\hat{\mu}K\Delta p^*}{r^3} = \Delta p \tag{4.18}$$

where $\quad \Delta p^* = 1-\xi-2\xi^2 + (3+2\xi)\xi^2 e^{\xi}E_1(\xi) \tag{4.19}$

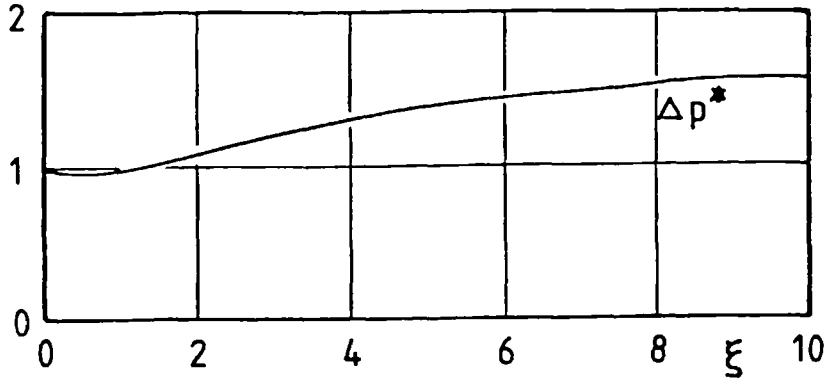A graph of Δp^* as a function of ξ

Fig. 4.2 Graph Δp^* defined in (4.19) as a function of ξ

is shown in fig. 4.2 with the asymptotes, $\Delta p^* \sim 2.0$, 1.0 for large, small ξ. Since Δp^* does not vary substantially with ξ, a suitable order of magnitude for Δp defined in (4.18) is

$$\Delta p = \partial/\partial r \ (p + \tau_{\theta\theta}) \Big|_{\theta=\theta_I} = 0\left(\frac{\hat{\mu K}}{r^3}\right) \tag{4.20}$$

The shear layer equations may be found from the continuity and stress equilibrium equations (4.2-4.4) once a new variable $\beta = \Theta - \theta$ (which measures the angle from the wall to a variable point) is introduced. The transformed equations are

$$\frac{1}{r} \frac{\partial}{\partial r} (ru) - \frac{1}{r} \frac{\partial v}{\partial \beta} = 0 \tag{4.21}$$

$$\frac{1}{r} \frac{\partial}{\partial r} [r(\tau_{rr} - \tau_{\theta\theta})] - \frac{1}{r} \frac{\partial}{\partial \beta} \tau_{r\theta} + \frac{\partial}{\partial r} (p + \tau_{\theta\theta}) = 0 \tag{4.22}$$

$$\frac{1}{r^2} \frac{\partial}{\partial r} (r^2 \tau_{r\theta}) - \frac{1}{r} \frac{\partial}{\partial \beta} (p + \tau_{\theta\theta}) = 0 \tag{4.23}$$

Let $x = \Theta - \theta_I$, so that rx is the thickness of the shear layer and assume the usual order of magnitude for lubrication theory, i.e.

$$x \ll 1$$

$$ru/K = 0(1), \quad r^{-1}\partial/\partial\beta = 0(1/rx) \quad \text{and} \quad \partial/\partial r = 0(1/r)$$

According to the usual theory it is expected that $v=0(Kx/r)$. If v is larger than this, then retaining the dominant term in the continuity equation (4.21) gives $\partial v/\partial\beta = 0$ and the boundary conditions at the wall cannot be satisfied except trivially for $v \equiv 0$ (in which case $\partial v/\partial\beta$ is not the dominant term.)

The largest term in the strain rate tensor $\dot{\gamma}$ is

$$\dot{\gamma}_{r\theta} = \frac{1}{r}\frac{\partial u}{\partial\theta} = 0(\frac{K}{xr^2}) \tag{4.24}$$

It is now appropriate to specify a constitutive equation for the stress τ. Assume a power-law type dependence with

$$\tau_{r\theta} = -q|\dot{\gamma}_{r\theta}|^n, \qquad \tau_{rr}-\tau_{\theta\theta} = -p|\dot{\gamma}_{r\theta}|^m \tag{4.25}$$

Using (4.24) to give an order of magnitude of (4.25), the order of the terms in equations (4.22-4.23) in order of appearance are

$$\frac{p}{r}(\frac{K}{r^2x})^m, \quad \frac{q}{rx}(\frac{K}{r^2x})^n, \quad \frac{\hat{\mu}K}{r^3} \qquad \text{equation (4.22)}$$

and

$$\frac{q}{r}(\frac{K}{xr^2})^n, \quad \frac{\hat{\mu}K}{xr^3} \qquad \text{equation (4.23)}$$

The shear stress term dominates the normal stress term in (4.22) provided

$$\frac{q}{xp}(\frac{K}{xr^2})^{n-m} \gg 1 \tag{4.26}$$

For the Butyl CI rubber $n \approx m$ and $q/p = 0(1)$. This is also the case for a number of melts including HDPE, PP and PS [60].

In addition n=m at high shear rates is a feature of the White-Metzner

Model which was developed specifically to model the shear stress and

the normal stress difference in simple shear flow [3]. Their model

is confirmed by data for LDPE and HDPE.

In any case, provide m-n<1 it will always be possible to

choose x small enough so that (4.26) is satisfied in some region not

including the origin. As the origin is approached, the normal

stress difference may have to be taken into consideration. However, in

what follows it will be assumed that the shear stress terms

dominate. Written in terms of (r, θ), (4.22) becomes upon retaining

the largest terms:

$$\frac{\partial}{\partial r} (p + \tau_{\theta\theta}) + \frac{1}{r} \frac{\partial}{\partial \theta} \tau_{r\theta} = 0 \qquad (4.27)$$

Of the terms in (4.23), only tne normal stress term is significant

when n < 1. Therefore in the variables (r, θ),

$$\frac{1}{r} \frac{\partial}{\partial \theta} (p + \tau_{\theta\theta}) = 0 \qquad (4.28)$$

and $p + \tau_{\theta\theta}$ does not vary across the shear layer but is determined

at the interface.

For consistency the terms in (4.27) must have the same

order of magnitude. Thus

$$x = 0 \left((\frac{q}{\mu}) (\frac{r}{K})^{2^{1-n}} \right)^{\frac{1}{1+n}} \qquad (4.29)$$

If n = 1 and writing $q = \mu$, equation (4.28) is obtained only if

$$\mu / \hat{\mu} \ll 1 \qquad (4.30)$$

and the consistency relation (4.29) is $x = 0(\hat{\mu}/\mu)^{\frac{1}{2}} \ll 1$, a stronger

requirement than (4.30). The 2FM with a Newtonian shear layer is

a possible model for wedge flow of a melt in at least two particular

cases.

(i)   The melt contains a low molecular weight phase which

is sufficiently mobile to migrate to the surface

at the wall to form a lubricating layer. Rubber

compounds exhibiting wall slip, particularly EPDM

and Nitrile compounds [36] and polymers such as

HDPE [49] and PVC are examples of such materials.

(ii) The die-entry is lubricated by an external agent of

low viscosity which is pumped into the region adjacent

to the wall. Winter et.al.[32] have used this

technique in an experiment intended to achieve pure

extensional motions in the entry region, although

Caswell [unpublished] disputes the possibility of

achieving such motions for $\Theta \nless 1$.

Otherwise if the melt is the same material in both regions then the

zero shear rate viscosities will be identical, $\mu = \hat{\mu}$. However as

discussed in the example of section 1.1 temperature rises may occur

at sufficiently high flux in the die-entry. Most of the temperature

variation occurs in a thin layer either adjacent or very close to

the wall.   In such cases, it should be possible to contain the

temperature layer within the shear layer, which would lower the

effective viscosity μ. As can be seen from fig. 2.13 for Butyl CI

a temperature rise of about $15^\circ C$ causes the viscosity μ to be halved

with a corresponding decrease in $\tau_{r\theta}$. So to this level of approximation

temperature rises increase the suitability of the 2FM. This conclusion

is valid for all values of n.

Rather than using a Power-Law model, a solution of (4.27) is obtained for the Ellis model given by [48] for the viscosity η

$$\frac{\mu}{\eta} = 1 + \left|\frac{\tau_{r\theta}}{s}\right|^{\alpha-1} \tag{4.31}$$

where s and α are constants; α is equivalent to $1/n$ in equation (4.25). This model has both a Newtonian constant viscosity region at low shear rates and a power law region at high shear rates. An expression for the shear rate $\dot{\gamma}_{r\theta}$ is obtained from (4.24) and (4.31) and (2.45)

$$\mu\dot{\gamma}_{r\theta} = \frac{\mu}{r}\frac{\partial u}{\partial\theta} = -\tau_{r\theta}\left(1+\left|\frac{\tau_{r\theta}}{s}\right|^{\alpha-1}\right) \tag{4.32}$$

The shear stress results from an integration of (4.27)

$$\tau_{r\theta} = -r\theta\Delta p - K_1(r) \tag{4.33}$$

where $K_1(r)$ is a function satisfying the boundary conditions. Let

$$\tau_I = -r\Delta p\theta_I - K_1 \tag{4.34}$$

be the shear stress at the interface and

$$\tau_w = -r\Delta p\Theta - K_1 \tag{4.35}$$

be the shear stress at the wall. Then since $\Delta p < 0$,

$$\tau_I < \tau_w, \quad \tau_I < 0 \tag{4.36}$$

Before calculating the velocity u, it is necessary to distinguish two possibilities.

Case I, backflow does not occur in the shear layer, in which case

$$\tau_w < 0$$

and $\tau_{r\theta} < 0$ everywhere within the shear layer.

Case II, backflow does occur, in which case

$$\tau_w > 0$$

and $\tau_{r\theta} = 0$ for some $\theta \in (\theta_I, \Theta]$.

For Case I, substitution of $\tau_{r\theta}$ in (4.33) into (4.32) gives

$$\frac{\partial u}{\partial \theta} = \frac{r}{\mu} (r\Delta p\theta + K_1)(1 + (r\Delta p\theta + K_1)^{\alpha-1}/s^{\alpha-1}) \qquad (4.37)$$

Integrating to obtain u satisfying the boundary condition (4.5) gives

$$u = -\frac{1}{\Delta p\mu}\{\tfrac{1}{2}[(r\Delta p\Theta + K_1)^2 - (r\Delta p\theta + K_1)^2] + \frac{1}{(\alpha+1)s^{\alpha-1}}[(r\Delta p\Theta + K_1)^{\alpha+1} - (r\Delta p\theta + K_1)^{\alpha+1}]\} \qquad (4.38)$$

Let $\quad \zeta = \tau_w - \tau_I = -r\Delta px \qquad\qquad\qquad (4.39)$

and

$$k = \frac{r\Delta p\Theta + K_1}{-r\Delta px} = \frac{\tau_w}{\tau_I - \tau_w} = -\frac{\tau_w}{\zeta} > 0 \qquad (4.40)$$

It can easily be shown that the boundary condition (4.9) requires that k satisfies

$$\frac{K\Delta p\mu}{r} = x\zeta^2\{-k-\tfrac{1}{2} + \frac{1}{\alpha+1}(\frac{\zeta}{s})^{\alpha-1}[k^{\alpha+1} - (k+1)^{\alpha+1}]\} \qquad (4.41)$$

The flux Q, is calculated from (4.15) as

$$\frac{Q\Delta p\mu}{r} = -x\zeta^2 -\{\frac{k}{2} - \frac{1}{6} + \frac{1}{\alpha+1}(\frac{\zeta}{s})^{\alpha-1}[k^{\alpha+1} + \frac{1}{\alpha+2}(k^{\alpha+2} - (k+1)^{\alpha+2})]\} \qquad (4.42)$$

and the interface shear stress τ_I is

$$\tau_I = (1+k)r\Delta px \tag{4.43}$$

In principle, it is possible to obtain x and k from (4.41, 4.42) once Q and $\hat{Q}$ are given.

The corresponding results for Case II can be shown to be

$$\frac{K\Delta p\mu}{r} = x\zeta^2\{j-\tfrac{1}{2} + \frac{1}{\alpha+1} \, (\frac{\zeta}{s})^{\alpha-1} (j^{\alpha+1}-(1-j)^{\alpha+1})\} \tag{4.44}$$

$$\frac{Q\Delta p\mu}{r} = -x\zeta^2\{j/2- \frac{1}{6} + \frac{1}{\alpha+1} \, (\frac{\zeta}{s})^{\alpha-1} (j^{\alpha+1}- \frac{1}{\alpha+2} \, (j^{\alpha+2}+(1-j)^{\alpha+2}))\} \tag{4.45}$$

$$\tau_I = (1-j)r\Delta px \tag{4.46}$$

where j is defined as

$$j = \frac{\tau_w}{\zeta} = -k = \frac{\tau_w}{\tau_w-\tau_I} \le 1 \tag{4.47}$$

since $\tau_w-\tau_I \ge \tau_w > 0.$

The asymptotic behaviour of x and k and therefore τ_I for large and small values of ζ/s is readily obtained.

For large ζ/s, corresponding either to small ξ or a Power-Law fluid, eliminating x and ζ/s from (4.41,4.42) and (4.44, 4.45)

$$\frac{Q}{K} \sim - \frac{k^{\alpha+1}+(k^{\alpha+2}-(k+1)^{\alpha+2})/(\alpha+2)}{k^{\alpha+1}-(k+1)^{\alpha+1}} \qquad \text{Case I} \tag{4.48}$$

$$\sim - \frac{j^{\alpha+1}-(j^{\alpha+2}+(1-j)^{\alpha+2})/(\alpha+2)}{j^{\alpha+1}-(1-j)^{\alpha+1}} \qquad \text{Case II} \tag{4.49}$$

$$\text{as } \zeta/s \to \infty$$

The critical value of Q/K signifying the transition between Case I and II is given when k = -j=0; thus $(Q/K)_{crit} = -1/(\alpha+2).$

A graph of k as a function of Q/K, for various values of α

is shown in fig. 4.3. The asymptote as Q/K → ∞ is clearly k=-j ~ -½,

and by using the binomial theorem it can be shown that the asymptote

as k → ∞ is Q/K ~ -½. (When Q/K < -½ no meaningful solution is

obtained since it requires x < 0). The important conclusion to be

drawn as far as the question of uniqueness is concerned is that k is

a single-valued function of Q/K.
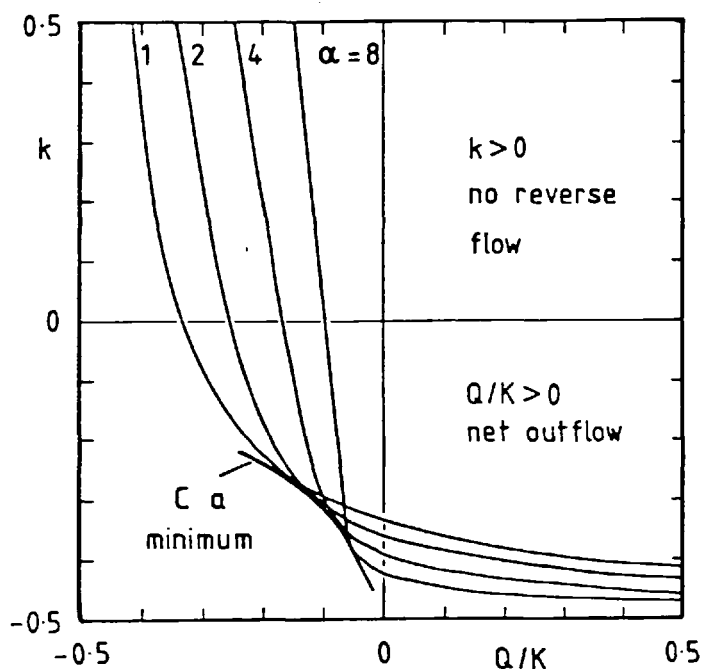
Fig. 4.3 Graph of k as a function of Q/K as given in (4.48)
and (4.49)

In terms of k, x and τ_I are given by

$$x^{2+\alpha} \sim \frac{(\alpha+1)}{(2\Delta p^*)^\alpha} \frac{\mu}{\hat{\mu}} (\frac{sr^2}{\hat{\mu}K})^{\alpha-1} (-k^{\alpha+1}+(1+k)^{\alpha+1})^{-1}$$

Case I

(4.50)

$$\sim \frac{\alpha+1}{(2\Delta p^*)^\alpha} \frac{\mu}{\hat{\mu}} (\frac{sr^2}{\hat{\mu}K})^{\alpha-1} (-j^{\alpha+1}+(1-j)^{\alpha+1})^{-1}$$

Case II

(4.51)

$$\tau_I \sim - \frac{\hat{\mu K}}{r^2} (4(\alpha+1)\Delta p^{*2} \frac{\mu}{\hat{\mu}} (\frac{sr^2}{\hat{\mu K}})^{\alpha-1})^{\frac{1}{\alpha+2}} \frac{(1+k)}{((1+k)^{\alpha+1}-k^{\alpha+1})^{1/(\alpha+2)}}$$

Case I   (4.52)

$$\sim - \frac{\hat{\mu K}}{r^2} (4(\alpha+1)\Delta p^{*2} \frac{\mu}{\hat{\mu}} (\frac{sr^2}{\hat{\mu K}})^{\alpha-1} ((1-j)^{\alpha+1}-j^{\alpha+1})^{-1})^{\frac{1}{\alpha+2}} (1-j)$$

Case II   (4.53)

as $\zeta/s \to \infty$

where the asymptote of Δp as $\xi \to 0$, which corresponds to $\zeta/s \to \infty$, has been used in place of Δp itself.

For small ζ/s, corresponding either to $\xi \to \infty$ or to a Newtonian fluid in the shear layer the equations for Case I and II are identical. So from (4.41-4.47)

$$\frac{Q}{K} \sim \frac{k/2 + 1/6}{k + \frac{1}{2}} \qquad \text{as} \quad \zeta/s \to 0 \qquad (4.54)$$

with the explicit solution for k

$$k = - (Q/K + 1/3)/(2Q/K+1) \qquad (4.55)$$

This expression for k is used to obtain x and τ_I

$$x^3 \sim \frac{3\mu}{\hat{\mu}\Delta p^*} (2Q/K + 1) \qquad (4.56)$$

$$\tau_I \sim - \frac{\hat{\mu K}}{r^2} (48\Delta p^{*2} \hat{\mu}/\mu)^{1/3} (Q/K + 2/3)(1+2Q/K)^{-2/3}$$

as $\zeta/s \to 0$ (4.57)

Because it is required that τ_I is finite, thus eliminating the possibility of $1+2Q/K \to 0$, the thickness of the shear layer being small depends essentially on $\mu/\hat{\mu}$ being small as suggested previously using order of magnitude arguments.

For reasonable internal consistency of the approximation method the expression in (4.12) is evaluated. The normal traction $p+\tau_{\theta\theta}$ at the interface is calculated from (4.18) by a straightforward integration with Δp^* replaced by its asymptotic value as $\zeta/s \to 0$. Clearly $p+\tau_{\theta\theta} \sim \hat{\mu}K/r^2$ in this limit, thus the internal consistency parameter

$$c \sim (\frac{\mu}{\hat{\mu}})^{1/3} (48)^{1/3} (\Delta p^*)^{2/3} (Q/K+2/3) (1+2Q/K)^{-2/3}$$

$$\text{as } \zeta/s \to 0 \qquad (4.58)$$

The approximation is therefore, reasonably accurate or internally consistent either for a Newtonian fluid in the shear layer or for an Ellis fluid far from the origin when $\mu/\hat{\mu} \ll 1$. This is precisely the condition for $x \ll 1$. (That Q/K should approach $-2/3$ is in admissable since then x would be negative).

From the expression (4.58) for x and the graph of Δp^* in fig. 4.2, it can be seen that if shear thinning does not occur, the relative thickness of the shear layer, x/Θ, increases as Δp^* decreases and that the maximum variation $x_{max}/x_{min} = (0.5)^{-1/3} \approx 1.3$.

It has been shown that the 2FM is a reasonable method when a true lubricating agent exists between the main body of the melt and the wall, but when this is not the case i.e. $\mu=\hat{\mu}$ the 2FM breaks down upstream $(r \to \infty)$. This means that it is not possible to determine Q and consequently x and k from the upstream conditions. So far in the analysis Q, the flux in the shear layer, has been treated as an arbitrary constant, but in view of the above remarks it might be desirable to involve some principle, preferably physical, which enables Q to be determined from the downstream flow. Returning to the original argument for the 2FM, it was stated that the elongational stress should be much greater than the shear stress, so that the interface

boundary condition on the shear stress (4.11) is insignificant

compared to that for the normal traction (4.10). This can now

be made stronger by requiring that the value of Q should be such that

the interface shear stress is a minimum. In terms of the accuracy

parameter C, C should be a minimum with respect to k in the limit

as $\zeta/s \to \infty$.

From (4.52) and (4.53) and the asymptotic value of $p+\tau_{\theta\theta}$

calculated from (4.18)

$$C \sim \left(4(\alpha+1)\Delta p^{*2} \frac{\mu}{\hat{\mu}} \left(\frac{sr^2}{\hat{\mu}K}\right)^{\alpha-1}\right)^{\frac{1}{\alpha+2}} \frac{(1+k)}{\left[(1+k)^{\alpha+1}-|k|^{\alpha+1}\right]^{\frac{1}{\alpha+2}}}$$

$$\text{as} \quad \zeta/s \to \infty \qquad (4.59)$$

for Case I and II with $k \in [-\frac{1}{2}, \infty)$. It can be shown numerically

that the minimum in C lies on the envelope of the set of curves

in fig. 4.3, as indicated. For all values of α in the range of

interest, Q/K is negative (a net inflow in the shear layer) and the

wall shear stress τ_w is positive indicating that backflow occurs with

the velocity being positive adjacent to the wall.

The upstream flow field can be calculated using an indirect

expansion by perturbing about Newtonian flow, the first term of which

determines the flux $\overline{Q}$. This is matched to the downstream 2FM

through $\overline{Q}$. Successive terms in the indirect expansion can only

be matched once higher order terms are calculated downstream. However

there is sufficient information to map out the essential features

of the whole flow field. Before doing this, further examination of

(4.54), apart from the value of k, shows that

$$C = O\left(\frac{sr^2}{\hat{\mu}K}\right)^{\frac{\alpha-1}{\alpha+2}} \quad \text{as} \quad \zeta/s \to \infty \qquad (4.60)$$

Since $\alpha > 1$ for a shear thinning fluid, (4.60) confirms the order of

magnitude arguments which suggested that the shear stresses become

negligible in their influence on the cone flow as the origin is

approached.

To give an example of the flow field expected for the 2FM,

the data of the example in Chapter 1 are used for the physical

dimensions and typical flow rates. This is supplemented with rheological

data from Chapter 2.   The parameters for the Ellis fluid are given

in Table 4.1; μ and α are the same as for the naive rheological model

of section 2.6 and s is chosen to fit the power-law region

Ellis fluid parameters	μ(Ns m^{-2})	s(Nm^{-2})	α
Butyl CI	1.05×10^6	4.4×10^4	7.7
Chloroprene	2×10^6	7×10^4	5.0

Table 4.1 Ellis fluid parameters for rubber compounds

The asymptotic form of x, $(\zeta/s)^{\alpha-1}$ and C are calculated for the mean

velocities $\bar{U}$ at the exit of the converging region.

	(i)	(ii)
$\bar{U}$	9.6m s^{-1}	0.12m s^{-1}
$K = \bar{U}_0 r_0 \cos 45°$	$1.6 \times 10^{-2} \text{m}^2 \text{s}^{-1}$	$2.0 \times 10^{-4} \text{m}^2 \text{s}^{-1}$
k	-0.41	-0.41
x	$2.2 \, r^{1.4}$	$44 r^{1.4}$
$(\zeta/s)^{\alpha-1}$	$0.33 r^{-4.1}$	$4 \times 10^{-5} r^{-4.1}$
C	$2.4 \, r^{1.4}$	$48 r^{1.4}$
Q	$-6.4 \times 10^{-4} \text{m}^2 \text{s}^{-1}$	$-8.0 \times 10^{-6} \text{m}^2 \text{s}^{-1}$
$\bar{Q}$	$-1.3 \times 10^{-2} \text{m}^2 \text{s}^{-1}$	$-1.6 \times 10^{-4} \text{m}^2 \text{s}^{-1}$

Table 4.2   2FM parameters for Butyl CI for flow in wedge
at mean velocities similar to Chapter 1: r
is measured in meters, $r_0 = 1.7 \times 10^{-3}$m.

The values of r_0 and r_1 as defined in fig. 4.1 are

$$r_0 = 1.7 \times 10^{-3} \text{m} \qquad r_1 = 1.1 \times 10^{-2} \text{m}$$

Using the expression in Table 4.2 the angle subtended by the shear

layer at r_1 is $x \approx 5°$ for flow rate (ii) and $C \approx 0.09$. So even at

the relatively low flow rate of (ii), the shear layer extends back

along the whole of the converging region. In this case the upstream

flow will be a fully developed channel flow. A sketch of the

streamlines is shown in fig. 4.4. The thickness of the shear layer
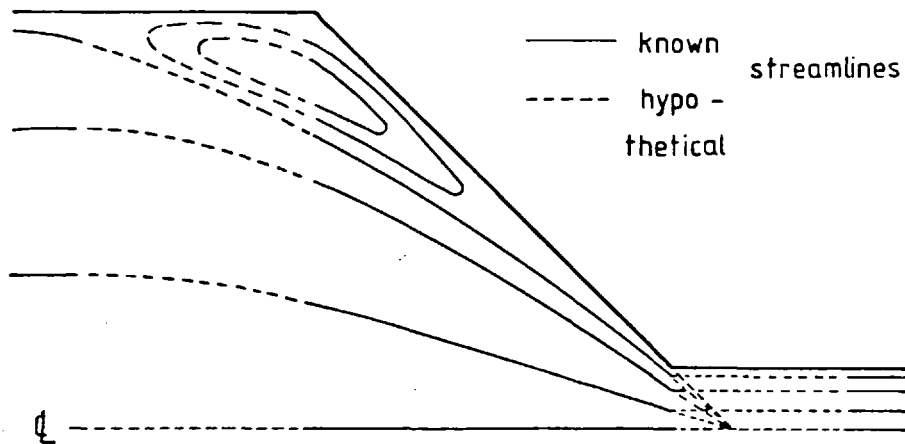
is somewhat exaggerated.

Fig. 4.4 Sketch of streamlines in converging region

The flux through the shear layer is small compared to that through

the core. Thus the interface streamline, when traced back upstream

and downstream is very close to the wall. The core streamlines show a

slight curvature due to the influence of the curvature of θ_I.

4.2 Cone Flow

The analysis for two fluid flow in a cone follows that for flow in a wedge. For this reason the method will not be described in such detail as in section 4.1 except where variations occur.

The equations of continuity and stress equilibrium with respect to a spherical coordinate system for steady axisymmetric flow (r,θ,ϕ) and velocity components (u,v,w) are

$$\frac{1}{r^2} \frac{\partial}{\partial r} (r^2 u) + \frac{1}{r} \frac{\partial v}{\partial \theta} + \frac{\cot\theta}{r} v = 0 \tag{4.61}$$

$$\frac{1}{r^2} \frac{\partial}{\partial r} [r^2(\tau_{rr} - \tau_{\theta\theta})] + \frac{\partial}{\partial r} (p + \tau_{\theta\theta}) + \frac{\cot\theta}{r} \tau_{r\theta}$$
$$+ \frac{1}{r} \frac{\partial}{\partial \theta} \tau_{r\theta} + \frac{\tau_{\theta\theta} - \tau_{\phi\phi}}{r} = 0 \tag{4.62}$$

$$\frac{1}{r^3} \frac{\partial}{\partial r} (r^3 \tau_{r\theta}) + \frac{1}{r} \frac{\partial}{\partial \theta} (p + \tau_{\theta\theta}) + \frac{\cot\theta}{r} \tau_{\theta\theta} = 0 \tag{4.63}$$

$$\frac{\partial}{\partial \phi} (p + \tau_{\phi\phi}) = 0 \tag{4.64}$$

The boundary conditions are

$$u(r, \pm\Theta) = v(r, \pm\Theta) = 0 \tag{4.65}$$

and the flux $\overline{Q}$ is given by

$$\overline{Q} = 2\pi \int_0^\Theta r^2 u \, dr \tag{4.66}$$

For an extensional flow field in the cone, the core velocity is of the form

$$\hat{u} = -\frac{K}{r^2}, \hat{v} = \hat{w} = 0 \tag{4.67}$$

Again a Maxwell Fluid is taken for the inner region with an constitutive equation in the integral upper converted formalism as

defined in (3.5) and (3.21).

The strain tensor $\gamma_{[0]}$ is calculated from the velocity field (4.67) to be

$$
\hat{\gamma}_{[0]} = \begin{pmatrix} 1-(\dfrac{3Ks}{r^3} + 1)^{4/3} & 0 & 0 \\[2em] 0 & 1-(\dfrac{3Ks}{r^3} +1)^{-2/3} & 0 \\[2em] 0 & 0 & 1-(\dfrac{3Ks}{r^3} +1)^{-2/3} \end{pmatrix}
$$

$$(4.68)$$

Evaluation of the stress tensor components follows

$$\hat{\tau}_{rr} = \frac{\mu}{\lambda}\{1-\xi^{-4/3}e^{\xi}\Gamma(7/3,\xi)\} \tag{4.69}$$

$$\hat{\tau}_{\theta\theta} = \hat{\tau}_{\phi\phi} = \frac{\mu}{\lambda}\{1-\xi^{2/3}e^{\xi}\Gamma(1/3,\xi)\} \tag{4.70}$$

$$\hat{\tau}_{r\theta} = \hat{\tau}_{r\phi} = \hat{\tau}_{\theta\phi} = 0 \tag{4.71}$$

in which $\Gamma(a,\xi)$ is the incomplete gamma function [58] and $\xi = r^3/(3\lambda K)$ is a dimensionless local Deborah Number or radial distance. In order to enable a complete order of magnitude evaluation of the shear layer equations, the normal traction gradient is calculated

$$\Delta p = \frac{\partial}{\partial r}(\hat{p}+\hat{\tau}_{\theta\theta}) = -\frac{1}{r^2}\frac{\partial}{\partial r}[r^2(\hat{\tau}_{rr}-\hat{\tau}_{\theta\theta})] = -\frac{2\mu\Delta p^*}{\lambda r\xi}$$

$$\Delta p = \frac{\mu}{\lambda r}\{(-\frac{8}{9}\xi^{-4/3}+\frac{4}{3}\xi^{-1/3} - 4\xi^{2/3}-3\xi^{5/3})e^{\xi}\Gamma(1/3,\xi)$$

$$+ 2 + 3\xi - \frac{8}{3}\xi^{-1}\}$$

$$(4.72)$$

Asymptotic expansions for large and small ξ are obtained

$$\Delta p \sim \frac{-2\hat{\mu}}{\lambda r\xi} = 0(\frac{\hat{\mu}K}{r^4}) \quad \text{as} \quad \xi \to \infty \tag{4.73}$$

and $\quad \Delta p \sim - \dfrac{8\mu\hat{\Gamma}(1/3)}{9\lambda r\xi^{4/3}} = 0(\dfrac{\hat{\mu}K^{4/3}\lambda^{1/3}}{r^5})$ $\qquad$ as $\quad \xi \rightarrow 0$ $\quad$ (4.74)

Thus Δp shows a character in conical different from that in wedge

flow. A graph of Δp^* is shown in fig. 4.5. Although far from the

origin the behaviour is similar to the wedge, i.e. it conforms

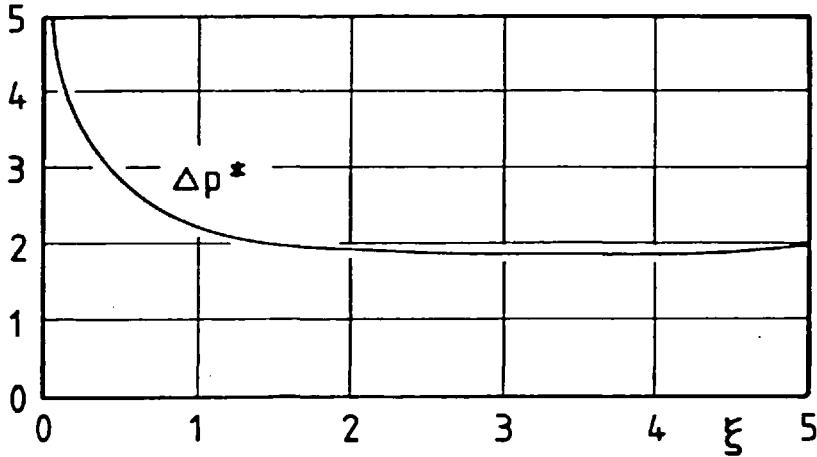to the Newtonian asymptote, at the origin it has a singularity.

Fig. 4.5 Graph of $\Delta p^*(\xi)$ defined in (4.72)

It is now shown, using an order of magnitude for a power-law

fluid similar to that in section 4.1, how to obtain the shear layer

equations. Introduce th variable $\beta = \Theta - \theta$ and transform equations

(4.61-4.63) to

$$\frac{1}{r^2} \frac{\partial}{\partial r} (r^2 u) - \frac{1}{r} \frac{\partial v}{\partial \beta} + \frac{\cot(\Theta-\beta)}{r} v = 0 \qquad (4.75)$$

$$\frac{1}{r^2} \frac{\partial}{\partial r} [r^2(\tau_{rr}-\tau_{\theta\theta})] + \frac{\partial}{\partial r} (p+\tau_{\theta\theta}) + \frac{\cot(\Theta-\beta)}{r} \tau_{r\theta} -$$

$$\frac{1}{r} \frac{\partial}{\partial \beta} \tau_{r\theta} + \frac{\tau_{\theta\theta}-\tau_{\phi\phi}}{r} = 0 \qquad (4.76)$$

$$\frac{1}{r^3} \frac{\partial}{\partial r} (r^3 \tau_{r\theta}) - \frac{1}{r} \frac{\partial}{\partial \beta} (p+\tau_{\theta\theta}) + \frac{\cot(\Theta-\beta)}{r} \tau_{\theta\theta} = 0$$

$$(4.77)$$

Assume the following orders of magnitude

$$\theta - \theta_I = x \ll 1$$

$$r^2 u/K = O(1), \qquad r^{-1}\partial/\partial\beta = O(\frac{1}{rx}), \qquad \partial/\partial r = O(1/r)$$

$$v = O(Kx/r^2), \qquad \tau_{r\theta} = O(q(\frac{K}{xr^3})^n)$$

$$\tau_{rr}-\tau_{\theta\theta} \text{ and } \tau_{\theta\theta}-\tau_{\phi\phi} = O\ (p(\frac{K}{xr^3})^m)$$

The second normal stress difference $\tau_{\theta\theta}-\tau_{\phi\phi}$, is chosen to

have the same order of magnitude as the first $\tau_{rr}-\tau_{\theta\theta}$, on the basis

of the limited experimental results available. Han [62] reports that

for a wide range of polymer melts $\tau_{\theta\theta}-\tau_{\phi\phi}$ varies between -0.1 and

-0.7 of $\tau_{rr}-\tau_{\theta\theta}$.

The shear stress term $r^{-1} \partial(\tau_{r\theta})/\partial\theta$ will dominate over the

normal stress terms in (4.76) provided

$$\frac{q}{xp} (\frac{K}{xr^3})^{n-m} \gg 1 \tag{4.78}$$

which is similar to the condition (4.26) and will be assumed to be

valid. The normal stress term $r^{-1} \partial(p+\tau_{\theta\theta})/\partial\theta$ will dominate the other

terms provided

$$\frac{\hat{\mu}}{q} (\frac{K}{xr^3})^{1-n} \gg 1 \qquad \text{as} \qquad r \to \infty \tag{4.79}$$

and $\qquad \frac{\hat{\mu}}{q} (\frac{K}{r^3})^{4/3-n} \lambda^{1/3} x^{-1+n} \gg \qquad \text{as} \quad r \to 0 \tag{4.80}$

Thus, far from the origin where the flow field must be

Newtonian, the 2FM is valid if $\hat{\mu}/\mu \gg 1$; the same condition as for

the wedge. At the other extreme, close to the origin the 2FM is valid

at least for all values of $n \le 1$ which is slightly different from the

wedge result.

So to first order the pressure does not vary across the

shear layer. For consistency it is expected that x will have

the order of magnitude

$$x = 0\left(\frac{q}{\hat{\mu}} \left(\frac{r^3}{K}\right)^{1-n}\right)^{\frac{1}{1+n}} \qquad \text{as } r \to \infty \qquad (4.81)$$

$$x = 0\left(\frac{q}{\hat{\mu}\lambda^{1/3}} \left(\frac{r^3}{K}\right)^{4/3-n}\right)^{\frac{1}{n+1}} \qquad \text{as } r \to 0 \qquad (4.82)$$

Retaining the largest terms the shear layer equations become

when written in terms of (r, θ)

$$\frac{\partial}{\partial r}(p + \tau_{\theta\theta}) + \frac{1}{r}\frac{\partial}{\partial\theta}\tau_{r\theta} \approx 0 \qquad (4.83)$$

The shear stress $\tau_{r\theta}$, is to be determined using the Ellis model (4.31)

and a shear rate $\dot{\gamma}_{r\theta}$ given by

$$\dot{\gamma}_{r\theta} = \frac{1}{r}\frac{\partial u}{\partial\theta} \qquad (4.84)$$

The boundary conditions at the interface $\theta = \theta_I$ are

$$\hat{u} = u \qquad (4.85)$$

$$\hat{p} + \hat{\tau}_{\theta\theta} = p + \tau_{\theta\theta} \qquad (4.86)$$

and the fluxes $\hat{Q}, Q$ in the cone and shear layer are

$$Q = 2\pi r^2 \int_\theta^\Theta u \, d\theta \qquad (4.87)$$

$$\hat{Q} = -2\pi K\theta_I \qquad (4.88)$$

Noting the strong similarity between the equations for cone

and wedge flow the equations for the flux and the shear stress at

the boundary of the shear layer are readily obtained for both Case I

and II corresponding to negative and positive τ_w. They are given by,

$$\frac{Q\Delta p\mu}{2\pi r^2} = - x\zeta^2 \left\{ -\frac{k}{2} - \frac{1}{6} + \frac{1}{\alpha+1}(\frac{\zeta}{s})^{\alpha-1} [k^{\alpha+1} + \frac{1}{\alpha+2} (k^{\alpha+2} - (k+1)^{\alpha+2})] \right\}$$

Case I   (4.89)

$$= - x\zeta^2 \left\{ j/2 - 1/6 + \frac{1}{\alpha+1}(\frac{\zeta}{s})^{\alpha-1} [j^{\alpha+1} - \frac{1}{\alpha+2} (j^{\alpha+2} + (1-j)^{\alpha+2})] \right\}$$

Case II   (4.90)

where k is a solution of

$$\frac{K\Delta p\mu}{r^2} = x\zeta^2 \left\{ -k-1/2 + \frac{1}{\alpha+1} (\frac{\zeta}{s})^{\alpha-1} [k^{\alpha+1} - (k+1)^{\alpha+1}] \right\} \quad (4.91)$$

Case I

$$= x\zeta^2 \left\{ j-1/2 + \frac{1}{\alpha+1} (\frac{\zeta}{s})^{\alpha-1} [j^{\alpha+1} - (1-j)^{\alpha+1}] \right\} \quad (4.92)$$

Case II

and $\tau_I = (1+k)r\Delta px$ Case I   (4.93)

$= (1-j)r\Delta px$ Case II   (4.94)

in which τ_I, ζ, k, j have the same meaning as in section 4.1.

The asymptote for small ζ/s is identical to the wedge but

with Q/K in (4.54-4.57) replaced by $Q/(2\pi K)$ (once Δp^* has been defined

for the cone). However the asymptote may correspond either to $\xi \rightarrow \infty$,

or to a Newtonian fluid throughout the shear layer ($s \rightarrow \infty$). As for

the wedge, as $\xi \rightarrow \infty$, the 2FM is valid only when $\hat{\mu}/\mu \gg 1$. But for

$s \rightarrow \infty$ and close to the origin Δp^* has a singularity according to ξ^{-1}.

Using the asymptote of Δp (4.74) and the definition of Δp^* (4.72)

the equations for x and τ_I corresponding to (4.56) and (4.57) are

$$x^3 \sim \frac{4\Gamma(1/3)(3\lambda K)^{1/3}}{3r} \frac{\mu}{\hat{\mu}} (\frac{Q}{\pi K} + 1) \quad (4.95)$$

$$\tau_I \sim - \frac{\hat{\mu}K}{r^2} [\frac{4}{9r} \Gamma(1/3)(3\lambda K)^{1/3}]^{2/3} (48 \frac{\mu}{\hat{\mu}})^{1/3} (\frac{Q}{2\pi K} + 2/3)(1 + \frac{Q}{\pi K})^{-2/3}$$

(4.96)

as $\zeta/s \to 0$

but with $s \to \infty$

and $\zeta \to \infty$

The interface angle θ_I approaches Θ as $r \to 0$. The accuracy parameter C can be evaluated once $p + \tau_{\theta\theta}$ is calculated from (4.74). Close to the origin

$$p + \tau_{\theta\theta} \sim \frac{2\mu\Gamma(1/3)(3\lambda K)^{4/3}}{9\lambda r^4} \qquad \text{as } r \to 0 \qquad (4.97)$$

and

$$C = O(r^{4/3}) \qquad \text{as } r \to 0 \qquad (4.98)$$

This confirms the validity of the 2FM for a Newtonian shear layer sufficiently close to the origin.

The asymptote for large ζ/s, corresponding to a Power-Law fluid, is similar to the wedge provided the correct asymptotic value of Δp^* is used. Figure 4.3 with Q/K replaced by $Q/(2\pi K)$ is the graph of the parameter k. Again the value of $Q/(2\pi K)$ minimising the interface shear stress τ_I lies on the envelope in fig. 4.3. The asymptotic results corresponding to (4.50-4.53) for x and τ_I are

$$x^{2+\alpha} \sim \frac{\alpha+1}{(2\Delta p^*)^\alpha} \frac{\mu}{\hat{\mu}} (\frac{sr^3}{\hat{\mu}K})^{\alpha-1} ((1+k)^{\alpha+1} - |k|^{\alpha+1})^{-1} \qquad \text{Case I \& II}$$

$$(4.99)$$

$$\tau_I \sim \frac{-\hat{\mu}K}{r^3} (4(\alpha+1)\Delta p^*)^2 \frac{\mu}{\hat{\mu}} (\frac{sr^3}{\hat{\mu}K})^{\alpha-1} ((1+k)^{\alpha+1} - |k|^{\alpha+1}))^{\frac{1}{\alpha+2}}$$

$$\text{Case I\&II} \qquad (4.100)$$

with $\qquad \Delta p^* \sim \frac{4\Gamma(1/3)(3\lambda K)^{1/3}}{9r}$

$$\text{as } \zeta/s \to \infty$$

and the accuracy or internal consistency parameter

$$C = \left(\frac{sr}{\hat{\mu}K}\right)^{3\frac{\alpha-1}{\alpha+2}} \left(\frac{r}{3\lambda K}\right)^{3\frac{\alpha}{3(\alpha+2)}} \qquad (4.101)$$

The calculations for the example flow field of section 4.1 are repeated for the cone. The parameters are given below in Table 4.3 for the rubber compound Butyl CI. The flows

	(i)	(ii)
$\overline{U}$	9.6 m s^{-1}	0.12 m s^{-1}
$K = \overline{U}(r_0\cos 45°)^2$	$1.4 \times 10^{-5} \text{m}^3\text{s}^{-1}$	$1.7 \times 10^{-7}\text{m}^3\text{s}^{-1}$
k	-0.41	-0.41
x	$1.9 \times 10^3 r^{2.9}$	$1.3 \times 10^5 r^{2.9}$
$(\zeta/s)^{\alpha-1}$	$1.2 \times 10^{-3} r^{-14}$	$1.2 \times 10^{27} r^{-14}$
c	$4.4 \times 10^3 r^{2.9}$	$3.1 \times 10^5 r^{2.9}$
Q	$-3.5 \times 10^{-6}\text{m}^3\text{s}^{-1}$	$-4.3 \times 10^{-8}\text{m}^3\text{s}^{-1}$
$\hat{Q}$	$-6.9 \times 10^{-5}\text{m}^3\text{s}^{-1}$	$-8.4 \times 10^{-7}\text{m}^3\text{s}^{-1}$

Table 4.3 2FM parameters for Butyl CI, for flow in an injection
nozzle at mean velocities similar to those
in example of section 1.1; r is measured in
meters, $r_0 = 1.7 \times 10^{-3}$ m

in a wedge and the cone are not completely similar; the large ζ/s asymptote depends on the fluid relaxation time λ, in the case of the cone flow, whereas the wedge flow is independent of λ. Because the relaxation time calculated from experimental data in section 2.6 was determined through the linear viscoelastic behaviour of Butyl CI, it is valid to use that value here; i.e. take $\lambda = 12.5$s. As in section 4.1 consider the size of x which is a maximum at $r = r_1 = 1.1 \times 10^{-2}$ m. Using the expression in table 4.3 for the flow (ii) $x \approx 16°$

The corresponding value of the accuracy or internal consistency

parameter is C ~ .65. So the shear layer is considerably thicker,

for cone flow as opposed to wedge flow, and C is somewhat larger

too.

The value of $(\zeta/s)^{\alpha-1}$ at $r=r_1$ is 3×10^{54} so that the shear

layer is essentially a power-law fluid extending the length of

the converging region. The streamlines for the flow field are

similar to those sketched in fig. 4.4 and in this case the thickness

of the shear layer is not exaggerated.

4.3   Towards a Two Zone Model

It has been shown in the previous two sections that the

Two Fluid Model is mathematically consistent. A modification can be

made to the physical conception of the problem by considering

the flow field to consist of only one fluid, but which exists in

two distinct deformation regions or zones. Part of the fluid

undergoes an irrotational deformation the other part a shearing

deformation as in the 2FM. The one fluid model is termed a Two Zone

Model(2ZM). Of course, if the flow field actually contains a second

distinct phase as in forced lubrication, wall slip, and the situation

of a relatively cool cone being lubricated by a hot shear layer,

then a 2ZM is inappropriate.

Since there is only one fluid present, the 2ZM requires

only one constitutive equation to be specified. If the method of

sections 4.1 and 4.2 is to be applicable then the constitutive

equation must be highly shear-thinning and exhibit high stresses in

extensional flows. The naive rheological model of section 2.6 satisfies

these requirements provided the non-affine parameter a $\neq$ 1.

To a first approximation, the interface between the two

zones is treated as a streamline.

The upstream behaviour of the converging flow field will

be similar to that of the 2FM and can be determined by perturbing

around the Newtonian solution. The aim of the analysis in this

section is to determine the asymptotic downstream behaviour, i.e.

close to the origin.

Flow in the Shear Zone

The naive rheological model possesses a power-law region

at high shear rates. The shear stress is determined using the

asymptotic expansion (2.67) and is given for both cone and wedge

flows (provided the coordinate system is suitably identified) by

$$\tau_{r\theta} \cong - \frac{\eta_0 \pi (\beta\lambda)^{1/\alpha - 1} |\dot{\gamma}_{r\theta}|^{1/\alpha}}{2\alpha Z(\alpha) \sin((\alpha+1)\pi/2\alpha)} \qquad (4.102)$$

A similar expression can be obtained for the first normal stress

difference for simple shear flow valid at high shear rates

$$\tau_{rr} - \tau_{\theta\theta} \cong - \frac{\eta_0 \lambda}{Z(\alpha)} \left\{ \frac{\pi (\beta\lambda)^{1/\alpha - 1} |\dot{\gamma}_{r\theta}|^{1/\alpha}}{\alpha \sin(\pi/2\alpha)} - \frac{\beta\lambda}{2} \right\} \qquad (4.103)$$

Clearly $\tau_{r\theta}$ and $\tau_{rr} - \tau_{\theta\theta}$ have the same dependence on the shear

rate. The order of magnitude inequalities (4.26) and (4.78) are

satisfied, ensuring that the shear stress terms dominate the normal stress

difference terms in the shear layer equations.

The Ellis model and the naive rheological model have the

same high shear rate, power-law region if

$$s = \frac{\eta_0}{\beta\lambda} \left[\frac{\pi}{2 \, z(\alpha)\sin((\alpha+1)\pi/2\alpha)} \right]^{\frac{\alpha}{\alpha-1}} \tag{4.104}$$

$$\mu = \eta_0 \tag{4.105}$$

With these assignations the shear layer parameters x, τ_I, Q/K, are

given by equations identical to the corresponding equations in

sections 4.1 and 4.2 for large $\zeta/2$.

For a complete evaluation of the shear layer it only remains

to determine Δp^* from the core zone.

Flow in a Core Zone - Wedge

In wedge flow the core zone is a line sink with the kinematics

of (4.8), for which the rate of strain tensor defined in (2.58)

is in 2-D

$$A = \frac{K}{r^2} \begin{pmatrix} a & 0 \\ 0 & -a \end{pmatrix} \tag{4.106}$$

The solution of (2.57) for the strain tensor E is

$$E_{rr} = (1 + \frac{2Ks}{r^2})^{a/2}$$

$$E_{\theta\theta} = (1 + \frac{2Ks}{r^2})^{-a/2} \quad , \quad s = t-t' \tag{4.107}$$

with all other components of E being zero. The stress tensor

defined by (2.56) is given as an integral by

$$\tau_{rr} = \frac{1}{a} \int_0^\infty M(s)[1-(1+\frac{2Ks}{r^2})^a]ds$$

$$\tau_{\theta\theta} = \frac{1}{a} \int_0^\infty M(s)[1-(1+\frac{2Ks}{r^2})^{-a}]ds \tag{4.108}$$

All other components of τ vanish identically.

The stress at small values of r depends strongly on the value of a, and so therefore do Δp and Δp^*. (At this stage the analysis could be continued in the style of a 2FM by leaving $M(s)$ unspecified as there should be enough information in (4.108) to determine the asymptotic dependence of Δp for small r.) With M given by (2.59) the non-zero stress tensor components become

$$\tau_{rr} = \frac{1}{a} \sum_{a=i}^{\infty} \frac{\eta_i}{\lambda_i} (1-\xi_i^{-a} e^{\xi_i} \Gamma(1+a,\xi_i)) \tag{4.109}$$

$$\tau_{\theta\theta} = \frac{1}{a} \sum_{i=1}^{\infty} \frac{\eta_i}{\lambda_i} (1-\xi_i^{a} e^{\xi_i} \Gamma(1-a,\xi_i))$$

in which the η_i and λ_i are given by (2.50) and $\xi_i = \dfrac{r^2}{2\lambda_i K}$. The quantity Δp is obtained from (4.109) as

$$\Delta p = -\frac{1}{r} \frac{\partial}{\partial r} r(\tau_{rr} - \tau_{\theta\theta}) = -\frac{2\eta_0 K \Delta p^*}{r^3} \tag{4.110}$$

$$= -\frac{1}{ar} \sum_i \frac{\eta_i}{\lambda_i} [G(a,\xi_i) - G(-a,\xi_i)] \tag{4.111}$$

where $\quad G(a,\xi_i) = [(2a-1)\xi_i^{-a} - 2\xi_i^{1-a}]e^{\xi_i} \Gamma(1+a,\xi_i)$ (4.112)

Unfortunately, it does not seem possible to express the infinite summation in (4.111) in terms of a finite number of known functions. So Δp would have to be evaluated numerically to obtain an estimate of the asymptotic behaviour of Δp^* the summation is truncated to include only the first term. It can be shown that as $\xi \to 0$

$$\Delta p^* \sim (2-1/a)\xi^{1-a} \qquad a \neq \tfrac{1}{2},0$$

$$\sim 2\Gamma(3/2)\xi^{3/2} \qquad a = \tfrac{1}{2} \tag{4.113}$$

$$\sim 2\xi \ln\xi \qquad a = 0$$

in which $\xi = r^2/2\lambda K$.

For the rubber compounds in Chapter 2, $1 > a > \frac{1}{2}$ and

so the first of the asymptotes applies (Should values of $a < \frac{1}{2}$

arise, then $\Delta p^* < 0$ which would necessitate a change in the

analysis in the shear layer.)

Calculations can be carried out for the cone and for different

rheological models but it is probably more important at this stage

to investigate how higher terms in the approximation method for the

2FM and 2ZM might be generated.

CHAPTER 5

CONCLUSION

The work presented in Chapters 2 to 4 covers a wide
range of subject matter, from experimental rheology to non-Newtonian
fluid mechanics, in an attempt to achieve a better understanding
of die-entry flow. Progress has been made in certain areas and the
main conclusions are drawn in this Chapter. It will also be
appropriate to make a number of pertinent comments here.

Great care has been taken to ensure that the rheological
measuring devices, the T.M.S. Rheometer and the Elongation Rheometer,
give accurate information about shear stress in simple shear
and the first normal stress difference in uniaxial extension.
The machines are eminently suitable for stiff polymers, such as
filled rubber compounds, it has been shown that unintentional slip
between the rubber and the solid walls can be prevented, by suitable
design of the bounding surfaces. The T.M.S. Rheometer appears to
be the first adequately designed machine of its kind available for
commercial use. The Elongation Rheometer allows experimentation
at substantially greater extension rates than was previously
possible.

The experimental results show that two highly filled rubber
compounds, Butyl and Chloroprene, exhibit an extensional stress in
uniaxial extension one or two orders of magnitude greater than the

shear stress and the first normal stress difference (the latter has

been established for Butyl rubber only) in simple shear at corresponding

rates of deformation. By performing the start-up of uniaxial

extension and simple shear over a range of temperatures it has been

demonstrated that the Time-Temperature Superposition Principle applies

to these flows producing a family of master curves. Application

of the T-T.S.P. provides a means of extending the deformation rate

range of available apparatus. At certain rates of extension, Hencky

strains in excess of 8 have been achieved with the Butyl CI compound.

In general, a state of steady stress is not attained: the stress

reaches a maximum then declines.

An exact solution for the slow flow of a general linear

viscoelastic fluid with radial streamlines through a $180°$ wedge

has been obtained. Attempts to achieve solutions with the same

radial streamlines but in a cone, or with a different constitutive

equation in a wedge, proved unsuccessful. It is suspected therefore,

that the exact solution is unique amongst fluids with memory integral

constitutive equations. However, examination of the perturbation

solutions of Schümmer [27] for the wedge flow of 3rd and 4th order

fluids shows that radial streamlines are obtained for a $180°$ wedge.

In the light of the discovery of Chapter 3, this suggests that an

exact solution with radial streamlines may exist for such fluids,

though this has not been obtained.

By an investigation of the convergence properties of the

asymptotic expansion of the exact solution, it was shown that the

existing perturbation and series solutions are invalid close to the

origin. The same is likely to be true for axisymmetric converging

flows. Direct expansions are necessary in the neighbourhood of the

origin, though the result of such an exercise in section 3.4 indicates

that the task is a complex one. If the arbitrary functions arising

in the direct expansion for a UCMF result from stating the constitutive

equation in a differential rather than an integral form, then it

is possible that a solution to the problem may be achieved by

evaluating the strain tensor $\gamma_{[0]}$, for an arbitrary velocity field,

as a Taylor Series about a position fixed in space. However, this

is a difficult problem, unlike the evaluation of $\gamma_{[0]}$ about present

time which happens to result in a series of Rivlin-Erickson tensors

[48].

A Conjecture has been advanced in order to determine the

first arbitrary function which occurs in the direct expansion of

the stream function. If the Conjecture is correct, then there

are no substantial vortices in the wedge flow of an UCMF for any wedge

angle. This would substantiate the observation of Boger [9] quoted

in section 1.2, that vortices will not occur for a UCMF because its

normal stresses in simple shear are quadratic at all shear rates.

An approximation method, the Two Fluid or Two Zone Model,

for the solution of flows in converging wedges and cones has been

put forward. The Model is mathematically consistent and a number of

solutions have been obtained. Dynamical consistency for two rubber

compounds was established using the experimental results of Chapter 2.

There are a number of points in relation to the Model which require

further investigation. One of these which was not discussed in

Chapter 4 is how the downstream boundary conditions may be satisfied.

The manner in which this could be done is described in Pearson and

Trottnow [33] for die-entry flow into a short capillary. Their entry-

flow is that of a sink $(u_\theta = u_\phi = 0)$ which undergoes a sudden velocity

rearrangement at the capillary entrance. The extension of this idea to

the 2FM is straightfoward.

The 2FM and 2ZM are applicable to a wide variety of possible die-entry flows, including the situations where lubricating agents are present or where a thermal boundary layer arises. The Models can easily be extended to flow in a converging annulus. The philosophy of the Models should also be suitable for other flows in which high extensions occur, as in callendering, for example. A wide range of polymers not just the two rubbers investigated in Chapter 2 is acceptable for the Model.

Although recirculating vortices arise in the Model shear layer next to the walls and extend throughout the length of the die-entry, they are not of the 'thickness' observed in the experimental flows of certain polymers such as LDPE. Indeed the assumptions of the Model rely on the shear layer being thin. Velocity measurements of the recirculating regions indicate that the deformation rates are small except in the neighbourhood of the core [9]. So, most of the vortex could be modelled as a Newtonian fluid. An improvement to the Model for fluids which exhibit large entrance vortices could be achieved by splitting the flow field into three regions: a core and a shear layer as presently and thirdly a Newtonian vortex. The shear layer would act as a thin transition layer from the core to the vortex.

Finally, a comment about the physical stability of the 2FM. It is well known that a number of polymers exhibit a critical shear rate above which the flow may become unstable (see for example [49,63]); though there is some dependence on the flow geometry. In particular, Vinogradov et. al. [63] showed experimentally that the instabilities in entrance flow occur at points of highest stress concentration; for example, at the join between an entrance region and a parallel

duct such as a capillary. The shearing deformation in the 2FM

occurs in a thin region and not across the whole field and is therefore

concentrated there. Thus if a critical shear rate is exceeded, it

will occur at the thinnest point of the shear layer which happens

to be at the downstream exit. It could easily arise that a critical

shear rate is exceeded in the entrance region but simultaneously

(and after substantial stress relaxation) not be attained far downstream

in a capillary or other parallel-sided duct.

REFERENCES

1.   R.T. Fenner, Principles of Polymer Processing,
          Macmillan Press Ltd., 1979, pp.147-148.

2.   J.R.A. Pearson, Polym. Eng. Sci., 18 (1978), 222-229.

3.   Y. Ide, J.L. White, J. Non-Newtonian Fluid Mech.,
          2 (1977) 281-298.

4.   A.B. Metzner, E.A. Uebler, C.F. Chan Man Fong, A.I.Ch. E.
          Journal, 15 (1969) 750-758.

5.   J.L. White, A. Kondo, J. Non-Newtonian Fluid Mech.,
          3 (1977) 41-64.

6.   E.B. Bagley, H.P. Scheiber, Trans. Soc. Rheol.,
          5 (1961) 341-353.

7.   C.D. Han, L.H. Drexler, J. Appl. Polym. Sci., 17
          (1973) 2329-2354.

8.   C.D. Han, L.H. Drexler, J. Appl. Polym. Sci., 17
          (1973) 2369-2393.

9.   T.J.F. Pickup, Ph.D. Thesis,Cambridge University (1970).

10.   K. Strauss, R. Kinast, Colloid Polym. Sci., 252 (1974)
          753-758.

11.   A.B. Metzner, A.P. Metzner, Rheol. Acta, 9 (1970) 174-181.

12.   J.R.A. Pearson, T.J.F. Pickup, Polymer, 14 (1973) 209-214.

13.   F.N. Cogswell, Polym. Eng. Sci., 12 (1972) 64-73.

14.   F.N. Cogswell, J. Non-Newtonian Fluid Mech., 4 (1978) 23-38.

15.   A.V. Ramamurthy, J.C.H. McAdam, J. Rheol., 24 (1980)
          167-188.

16.   P.J. Cable, D.V. Boger, A.I.Ch.E. Journal, 24 (1978) 869-879.

17.   P.J. Cable, D.V. Boger, A.I.Ch.E. Journal, 24 (1978) 992-999.

18.   P.J.Cable, D.V. Boger, A.I.Ch.E. Journal, 25 (1979) 152-159.

19   K.L. Tan, C. Tiu, J. Non-Newtonian Fluid Mech., 6 (1979)
          21-45.

20.   D.V. Boger, Proc. Intern. Cong. Rheol. VIII, Vol.1 (1980)
      195-218.

21.   L. Rosenhead, Proc. Roy. Soc. A175 (1940) 436-467.

22.   H.K. Moffatt, B.R. Duffy, J. Fluid Mech., 96 (1980) 299-313.

23.   J.L. Duda, J.S. Vrentas, Trans. Soc. Rheol., 17 (1973) 89-108.

24.   J.R. Black, M.D. Denn, J. Non-Newtonian Fluid Mech., 1
      (1976) 83-92.

25.   K. Strauss, Acta Mechanica, 20 (1974) 233-246.

26.   J.R. Black, Ph.D. Dissertation, University of Delaware,
      Newark (1974).

27.   P. Schümmer, Rheol. Acta, 7 (1968) 271-277.

28.   W.J. Harrison, Proc. Camb. Phil. Soc., 19 (1919) 307-312.

29.   R.C. Ackerberg, J. Fluid Mech., 21 (1965) 47-81.

30.   A.B. Metzner, Rheol. Acta, 10 (1971) 434-444.

31.   H.M. Laun, H. Münstedt, Rheol. Acta, 17 (1978) 415-425.

32.   H. Winter, C. Macosko, K. Bennett, Rheol. Acta, 18 (1979)
      323-334.

33.   J.R.A. Pearson, R. Trottnow, J. Non-Newtonian Fluid Mech.,
      4 (1978) 195-215.

34.   Y. Ide, J.L. White, J. Appl. Polym. Sci., 22 (1978) 1061-1079.

35.   J.F. Stevenson, A.I.Ch.E. Journal, 18 (1972) 540-547.

36.   D.M. Turner, M.D. Moore, Plastics and Rubber: Processing,
      5 (1980) 81-84.

37.   K. Walters, Rheometry, Chapman and Hall, 1975, p.60.

38.   R.W. Connelly, L.J. Garfield, G.H. Pearson, J. Rheol.,
      23 (1979) 651-662.

39.   M. Mooney in Rheology, Theory and Applications, F.R. Eirich (ed.)
      Academic Press Inc., 1958, Vol. 2, Ch.5.

40.   G.A.D. Briggs, B.J. Briscoe, Phil. Mag., A38 (1978) 387-399.

41.   K.A. Grosch, Proc. Roy. Soc., A274 (1963) 21-39.

42.   F.P. Bowden, D. Tabor, Friction and Lubrication of Solids,
      Oxford University Press, 1964, Vol. 2, p.296.

43. J. Brandrup, E.H. Immergut, (eds.), Polymer Handbook, 2nd ed., Wiley Interscience, 1975.

44. S. Timoshenko, D.H. Young, Engineering Mechanics, 4th ed., McGraw-Hill Kogakusha Ltd., 1956, p.157.

45. W.F. Ames, Nonlinear Partial Differential Equations in Engineering, Academic Press, 1972, Vol.2, p.5.

46. L.R.G. Treloar, The Physics of Rubber Elasticity 3rd ed., Clarendon Press, 1975, p.67.

47. J.M. Dealy, J.Non-Newtonian Fluid Mech., 4 (1978) 9-21.

48. R.B. Bird, R.C. Armstrong, O. Hassager, Dynamics of Polymeric Liquids, John Wiley & Sons, 1977, Vol.1.

49. E. Uhland, Rheol. Acta, 18 (1979) 1-24.

50. G.V. Vinogradov, A.Ya. Malkin, V.F. Shumsky, Rheol. Acta, 9 (1970) 155-163.

51. T. Raible, J. Meissner, Proc. Intern. Cong. Rheol. XIII, Vol.2, (1980) 425-430.

52. W. Philippoff, Trans. Soc. Rheol., 10 (1966) 317-334.

53. C.J.S. Petrie, J. Non-Newtonian Fluid Mech., 2 (1977) 221-253.

54. O. Hassager, S. Pedersen, J. Non-Newtonian Fluid Mech., 4 (1978) 261-268.

55. M.W. Johnson, Jr., D. Segalman, J. Non-Newtonian Fluid Mech., 2 (1977) 255-270.

56. H.C. Lau, W.R. Schowalter, J. Rheol., 24 (1980) 507-516.

57. T.W. Spriggs, Chem. Eng. Sci., 20 (1965) 931-940.

58. M. Abramowitz, I. A.Stegun, (eds.), Handbook of Mathematical Functions, Applied Maths Series No.55, U.S. Nat. Bureau of Standards, Washington D.C., 1964 pp228-263.

59. C.J.S. Petrie, Elongational Flows, Pitman, 1979, p.21.

60. C.D. Han, K.U. Kim, N. Siskovic, C.R. Huang, J. Appl. Polym. Sci., 17 (1973) 95-103.

61. M. Van Dyke, Perturbation Methods in Fluid Mechanics, Parabolic Press, 1975, p.41.

62. C.D. Han, Rheology in Polymer Processing, Academic Press, 3rd ed., 1976, p.55.

63. G.V. Vinogradov, N.I. Insarova, B.B. Boiko, E.K. Borisenkova, Polym. Eng. Sci., 12 (1972) 323-334.

64. A.M. Hull, J. Non-Newtonian Fluid Mech., 8 (1981) 327-336.

APPENDICES

A1.   Calculation of shear stress on rotor surface

Let the applied torque be T.

Since the shear stress is effectively constant over the whole rotor surface it is readily integrated.   Separating the integration into the three surfaces of the rotor

(i)   top cone

$$T_1 = 2\pi \int_0^R (r\tau_{r\theta}) r\, dr$$

$$= \frac{2\pi}{3} \tau_{r\theta} R^3$$

(A1.1)

(ii)   middle cylinder

$$T_2 = 2\tau_{r\theta} \, \pi R^2 h$$

(A1.2)

(iii)   bottom frustrum

$$T_3 = \tau_{r\theta} \int_{R_1}^R 2\pi r^2 dr$$

$$= \frac{2\pi}{3} \tau_{r\theta} (R^3 - R_1^3)$$

(A1.3)

Thus with $T = \sum_1^3 T_i$, equation (2.1) is obtained, i.e.

$$\tau_{r\theta} = \frac{3T}{2\pi (2R^3 - R_1^3 + 3R^2 h)}$$

(A1.4)

A2.   Miscellaneous calculations in the analysis of slip on take-up wheel

Complete solution for a linear elastic solid

The constitutive equation for a linear elastic solid is

$$\sigma = G(\gamma - 1), \qquad G \text{ a constant} \qquad (A2.1)$$

Let $\underline{\sigma} = \sigma/G$, then eliminating γ from (2.31) using (A2.1) gives

$$\frac{\dot{\underline{\sigma}}_0}{\underline{\sigma}_0 + 1} = \frac{R\dot{\underline{\sigma}}_0}{\mu L\underline{\sigma}_0} + \frac{\underline{\sigma}_0 + 1}{\underline{\sigma}_0 \exp(-\mu(\omega t + \phi)) + 1}\left[\dot{\epsilon} - \frac{R\dot{\underline{\sigma}}_0}{\mu L\underline{\sigma}_0}\right] \qquad (A2.2)$$

Write $s = \exp[-\mu(\omega t + \phi)]$, $y = \underline{\sigma}_0$, $\kappa = \dfrac{R}{\mu L}$

then $\dot{} = \dfrac{d}{dt} = -\mu s \omega \dfrac{d}{ds}$

Thus (A2.2) becomes

$$\mu\omega s\dot{y}\{ys + 1 + \kappa(y+1)(1-s)\} + (y+1)^2 \dot{\epsilon} = 0 \qquad (A2.3)$$

which is of the form of Abel's equation of the second kind.
Integration follows after inversion considering y as the independent variable and s the dependent variable (the equation becomes a Bernoulli equation

$$\frac{ds}{dy} = -2\mu s^2 \frac{(y - y\kappa - \kappa)}{(y+1)^2} - 2\mu s \frac{(1 + \kappa + y\kappa)}{(y+1)^2} \qquad (A2.4)$$

The solution of (A2.4) satisfying the initial condition (2.24), which is equivalent to $\underline{\sigma}_0(0) = 0$, is written in the variables $\underline{\sigma}_0$ and t as

$$\exp[\mu(\omega t + \phi)] = \exp[\mu(\phi + L\underline{\sigma}_0/((\underline{\sigma}_0 + 1)R))](\underline{\sigma}_0 + 1) - \underline{\sigma}_0 \qquad (A2.5)$$

Equation (A2.5) is an implicit equation for $\underline{\sigma}_0(t)$.

Slip ceases when (2.34) holds, so the quantity $\dfrac{\dot{\sigma}_0}{2\mu\dot{\sigma}_0 t}$ is evaluated from (A2.5)

$$\frac{\dot{\sigma}_0}{2\epsilon\mu\dot{\sigma}_0} = \frac{\exp[\mu(\phi+(L/R)\sigma_0/(\sigma_0+1))](\sigma_0+1)-\sigma_0}{\exp[\mu(\phi+(L/R)\sigma_0/(\sigma_0+1))](\sigma_0+\mu(L/R)\sigma_0/(\sigma_0+1))-\sigma_0}$$

(A2.6)

$$= 1 \quad \text{if and only if} \quad \frac{\mu L \sigma_0}{R(\sigma_0+1)} = 1$$

(A2.7)

Solving (A2.7) for σ_0

$$\sigma_0 = (\frac{\mu L}{R} - 1)^{-1}, \quad \frac{\mu L}{R} \neq 1$$

(A2.8)

Since $\sigma_0 \geq 0$ for a physically meaningful situation, (A2.8) implies

that slip ceases if and only if $\mu > R/L$ ($R/L = \frac{1}{2}$ for the take-up

wheel.)

Admissability of the no-slip initial condition

The no-slip initial condition (2.25) is physically realistic

but it is possibly mathematically inadmissable because of the

approximation to slow flow and the implicit assumption of the motion

starting impulsively.

Consider equation (2.30) which is the solution for the

velocity u of the filament on the take-up wheel in terms of the

strain $\gamma(\theta,t)$ and the time-dependent component of the engineering

stress $\sigma_0(t)$. Taking the limit of u as $t \to 0$ and using the initial

condition (2.24)

$$\lim_{t \to 0} u(\theta,t) = \omega R$$

(A2.9)

as required.

However, consider the solution (A2.5) obtained for

a linear elastic solid. The solution was chosen to satisfy

the initial condition (2.24). The velocity at $\theta = 0$ can be calculated

from (A2.5) by evaluating $(L\gamma_t/\gamma)_{\theta=0}$ or equivalently for a linear

elastic solid $L\dot{\sigma}_0/(\sigma_0+1)$. The resulting expression is complicated

and as only the limit as $t \to 0$ is required intermediatory results

are not stated. It can be shown that

$$\lim_{t \to 0} \frac{L\dot{\sigma}_0}{\sigma_0+1} = \frac{\mu\omega L e^\phi}{(1+2\mu)e^\phi-1} \qquad (A2.10)$$

which equals ωR only when $\phi = 0$ (ϕ is given by the initial position

of the fixed point B on the take-up wheel).

*Condition for non-recurrence of slip when viscous effects
are important*

Viscous effects are introduced into the model by allowing

relaxation of stress to occur through a relaxation time λ. Consider

times greater than t_{ns} and whether slip recurs at $\theta = 0$. Since the

stress relaxation in the free length of the filament is independent

of position, it can be incorporated into $\sigma_0(t)$ as in (2.16).

On the take-up wheel, since $t \geq t_{ns}$ the filament adheres and the

strain remains constant following an element of the filament. This

means that stress relaxation depends on the time θ/ω , that the

filament element has been in contact with the take-up wheel and is

incorporated into (2.36) by multiplying by a factor of $\exp(-\theta/(\lambda\omega))$.

Thus

$$\sigma = \sigma_0(t-\theta/\omega)\exp(\frac{-\theta}{\lambda\omega}) \qquad \text{for} \quad t-\theta/\omega \geq t_{ns} \qquad (A2.11)$$

However, consider the solution (A2.5) obtained for

a linear elastic solid.   The solution was chosen to satisfy

the initial condition (2.24).   The velocity at $\theta = 0$ can be calculated

from (A2.5) by evaluating $(L\gamma_t/\gamma)_{\theta=0}$ or equivalently for a linear

elastic solid $L\dot{\underline{\sigma}}_0/(\underline{\sigma}_0+1)$.   The resulting expression is complicated

and as only the limit as $t \to 0$ is required intermediatory results

are not stated.   It can be shown that

$$\lim_{t \to 0} \frac{L\dot{\underline{\sigma}}_0}{\underline{\sigma}_0+1} = \frac{\mu\omega Le^{\phi}}{(1+2\mu)e^{\phi}-1} \qquad (A2.10)$$

which equals ωR only when $\phi = 0$ (ϕ is given by the initial position

of the fixed point B on the take-up wheel).

Condition for non-recurrence of slip when viscous effects
are important

Viscous effects are introduced into the model by allowing

relaxation of stress to occur through a relaxation time λ.   Consider

times greater than t_{ns} and whether slip recurs at $\theta = 0$.   Since the

stress relaxation in the free length of the filament is independent

of position, it can be incorporated into $\sigma_0(t)$ as in (2.16).

On the take-up wheel, since $t \geq t_{ns}$ the filament adheres and the

strain remains constant following an element of the filament.   This

means that stress relaxation depends on the time θ/ω , that the

filament element has been in contact with the take-up wheel and is

incorporated into (2.36) by multiplying by a factor of $\exp(-\theta/(\lambda\omega))$.

Thus

$$\sigma = \sigma_0(t-\theta/\omega)\exp\left(\frac{-\theta}{\lambda\omega}\right) \qquad \text{for} \quad t-\theta/\omega \geq t_{ns} \qquad (A2.11)$$

Slip does not recur at $\theta = 0$ if (2.38) is satisfied, which for (A2.11) becomes

$$(\lambda \frac{\dot{\sigma}}{\sigma} + 1) \leq \lambda\omega\mu = \frac{L\dot{\epsilon}}{R} \lambda\mu \qquad (A2.12)$$

It is not intended that the condition (A2.12) should be applicable for times t such that $0 \leq t - t_{ns} << 1$ because the rubber has been assumed to be elastic in the neighbourhood of $t = t_{ns}$. From the graph of the experimental measurement of the engineering stress fig.2.7, it can be seen that stress relaxation is particularly important for times when $\dot{\sigma}_0 \leq 0$. In this case, (A2.12) is satisfied at least when

$$\frac{L\dot{\epsilon}}{R} \lambda\mu \geq 1 \qquad (A2.13)$$

However, the implication of (A2.12) for an analysis which assumed viscoelasticity of the rubber for all times t, is that the time to no slip t_{ns} would be only slightly increased for a large enough relaxation time λ.

A3. Wall slip analysis in T.M.S. and Davenport Capillary Rheometers

Flow in the T.M.S. Rheometer

The lubricating layer is formed on the face of the smooth rotor which is either ground or polished, as is shown in fig.A3.1. Let the interface between the layer and the bulk of the rubber have an angular velocity Ω_s and relative thickness $\phi - \phi_s$. Since the flow is viscometric , Ω_s and ϕ_s are constant functions of position.
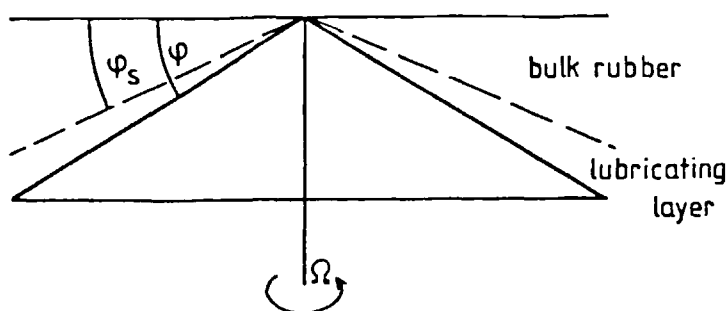
Fig. A3.1 Upper cone and plate in T.M.S.
          Rheometer with position of lubricating
          layer indicated.

The angle of the gap between the cone and the plate ϕ, is small so

that the shear stress $\tau_{\phi\psi}$, is approximately constant throughout

the gap, and the shear rate is constant, though not identical, in

each of the two layers. It is necessary to satisfy no-slip boundary

conditions on the walls and continuity of velocity across the inter-

face.

Assume both the bulk rubber and the lubricating layer

can be described by a Power-Law equation, then

(i) bulk rubber, inner field, $\tau_{\phi\psi} = m(\dot{\gamma}^I)^n$, $\dot{\gamma}^I = \dfrac{\Omega_s}{\phi_s}$

$$(A3.1)$$

(ii) lubricating fluid, outer field, $\tau_{\phi\psi} = p(\dot{\gamma}^0)^q$, $\dot{\gamma}^0 = \dfrac{\Omega - \Omega_s}{\phi - \phi_s}$

$$(A3.2)$$

The subscripts ϕ, ψ are dropped in what follows.

The constants m, n are determined from the data for the grooved rotor

(see fig. 2.9). The other constants, Ω_s, ϕ_s, p and q are unknown.

Assume a functional form for the ground rotor data in fig.2.9

that

$$\tau = \alpha \left(\frac{\Omega}{\phi}\right)^\beta \qquad\qquad (A3.3)$$

for known constants α, β.

Using the fact that the shear stress is constant for any given Ω_i

$$\tau(\frac{\Omega}{\phi}) = m(\frac{\Omega_s}{\phi_s})^n = p(\frac{\Omega-\Omega_s}{\phi-\phi_s})^q = \alpha(\frac{\Omega}{\phi})^\beta \qquad \text{(A3.4)}$$

It follows that

$$\frac{\phi_s}{\phi} = \frac{(\frac{\tau}{p})^{1/q} - (\frac{\tau}{\alpha})^{1/\beta}}{(\frac{\tau}{p})^{1/q} - (\frac{\tau}{m})^{1/n}} \qquad \text{(A3.5)}$$

which relates ϕ_s to the other parameters.

Flow in Davenport Capillary Rheometer
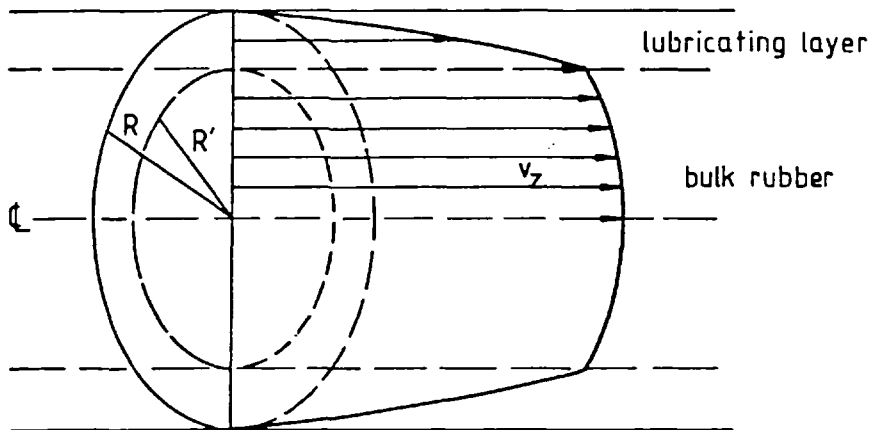
Fig. A3.2 Lubricating layer and bulk rubber
in flow through a capillary

Let v_z^I and v_z^O be the inner and outer velocity fields; laminar flow is assumed, so $v_r = v_\theta \equiv 0$. Let the inner flow of bulk rubber have a radius R' and let the outer flow of lubricating fluid be situated in $r \in (R', R]$ as in fig. A3.2. It is required to satisfy continuity of velocity and stress across the interface and the no-slip boundary condition on the wall. The solutions for the velocity fields obtained from the dynamic equations, and satisfying the boundary conditions and using the constitutive relations (A3.1, A3.2) are

$$v_z^I = (\frac{\tau_R R'}{mR})^{1/n} \frac{R'}{1/n+1} \{1-(\frac{r}{R'})^{1/n+1}\} + (\frac{\tau_R}{p})^{1/q} \frac{R}{1/q+1} \{1-(\frac{R'}{R})^{1/q+1}\}$$

(A3.6)

$$v_z^0 = (\frac{\tau_R}{p})^{1/q} \frac{R}{1/q+1} \{1-(\frac{r}{R})^{1/q+1}\}$$

(A3.7)

in which τ_R is the shear stress at the wall.

The total flux Q can be calculated to be:

$$Q = \pi R^3 \{ (\frac{\tau_R}{p})^{1/q} \frac{(1-(\frac{R'}{R})^{1/q+3})}{1/q+3} + (\frac{\tau_R}{m})^{1/n} \frac{(\frac{R'}{R})^{1/n+3}}{1/n+3} \}$$

(A3.8)

Relating the two flows

The flows in a capillary and a cone-plate device can be related by expanding ϕ_s/ϕ and Q as Taylor Series.

A Taylor Series expansion about $\phi_s/\phi = 1$ is

$$\frac{\phi_s}{\phi} = 1 - (\frac{p}{q})^{1/q} \{ (\frac{\tau}{R})^{1/\beta} - (\frac{\tau}{m})^{1/n} \} + \{ \begin{matrix} \text{higher order terms} \\ \text{in } (p/\tau)^{1/q} \end{matrix} \}$$

(A3.9)

The expansion is valid for

$$(\frac{\tau}{p})^{1/q} = \dot\gamma^0 = \frac{\Omega - \Omega_s}{\phi - \phi_s} \gg 1$$

that is for a thin lubricating layer with a low viscosity relative to the bulk rubber.

Let the flows in the T.M.S. and Capillary Rheometers be compared at the same values of the shear stress; the shear stress in the gap is equated with the shear stress at the wall of the capillary

$$\tau = \tau_R$$

(A3.10)

It is reasonable to suppose that the relative thickness of

the lubricating layer depends solely on the shear stress at

a solid surface, thus when (A3.10) is true

$$\frac{R'}{R} = \frac{\phi_s}{\phi} \qquad (A3.11)$$

Consider evaluating a Taylor Series for Q. Using (A3.9), (A3.10)

and (A3.11) an expression is obtained for the term R'/R in (A3.8)

$$(\frac{R'}{R})^{1/q+3} = 1 - (1/q+3)(\frac{p}{\tau})^{1/q}\{(\frac{\tau}{\alpha})^{1/\beta} - (\frac{\tau}{m})^{1/n}\} + 0((\frac{p}{\tau})^{2/q})$$

$$(A3.12)$$

The results in fig. 2.9 for the capillary rheometer are plotted in

terms of an apparent shear rate $\dot{\gamma}_A$;

$$\dot{\gamma}_A = \frac{4Q}{\pi R^3} \qquad (A3.13)$$

which is readily written as a Taylor Series using (A3.8) and (A3.12)

$$\dot{\gamma}_A = 4\{(\frac{\tau}{\alpha})^{1/\beta} - (\frac{\tau}{m})^{1/n} + \frac{n}{3n+1}(\frac{\tau}{m})^{1/n}\} + \{h.o.t. \ in \ (\frac{p}{\tau})^{1/q}\}$$

$$(A3.14)$$

This can immediately be rewritten in terms of shear rates

(with the understanding that they are evaluated at the same value of

shear stress) as

$$\dot{\gamma}_A = 4(\dot{\gamma}_{ground} - \frac{2n+1}{3n+1}\dot{\gamma}_{grooved}) + 0(\frac{p}{\tau})^{1/q} \qquad (A3.15)$$

When the lubricating layer is not formed, $\alpha = m$, $\beta = n$ and the Rabinowitsch

Correction is retrieved, i.e.

$$\dot{\gamma}_A = \frac{4n}{3n+1}\dot{\gamma}_{grooved} \qquad (A3.16)$$

A4.   Published Paper

Part of Chapter 3 was recently published [64] and a copy of the paper is included here.

AN EXACT SOLUTION FOR THE SLOW FLOW OF A GENERAL LINEAR VISCOELASTIC FLUID THROUGH A SLIT

A.M. HULL

*Department of Chemical Engineering and Chemical Technology, Imperial College of
Science and Technology, London, SW7 (Gt. Britain)*

(Received January 16, 1981)

Summary

An exact solution for the low Reynolds Number flow of an upper convected general linear viscoelastic fluid through a slit is presented. The solution, which is believed to be isolated, involves radial streamlines. Two of the more obvious possible further solutions for converging flow are shown to fail. A comparison with experimental results of stress-birefringence measurements shows a good qualitative agreement with a special case of the exact solution.

The theoretical work of Strauss is examined. A particular case of his result is retrieved in a manner which gives new information about its general validity.

1. Introduction

General solutions are known for the slow flow of a Newtonian and a "power-law" fluid in a wedge of arbitrary half-angle α (α ≤ π/2) which involves radial streamlines [1,2]. The velocity field is given in cylindrical coor-
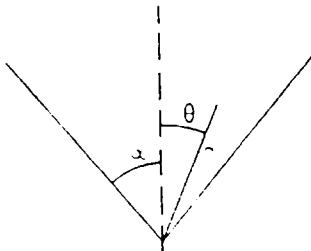

Fig. 1. Geometry and coordinate system of the flow problem.

328

dinates by (see Fig. 1)

$$v_r = -f(\theta)/r, \qquad v_\theta = v_z = 0 \tag{1.1}$$

for an arbitrary function, f, satisfying the boundary conditions. An exact solution for the wedge flow of an Upper Convected General Linear Visco-Elastic Fluid (UCGLV-EF) involving the kinematics (1.1) is obtained for $\alpha = \pi/2$ but not otherwise. This solution is given below, together with a discussion of its characteristics and a comparison with the experimental data of Han and Drexler [3].

2. The Exact Solution

The geometry of the problem is shown in Fig. 1. At the outset no restriction is placed on the wedge half-angle, α. Stress and velocity fields are required which satisfy the equations of mass conservation (2.1) and stress equilibrium (2.2, 2.3), the relevant constitutive equation (2.4) and the boundary conditions (2.5) for incompressible, steady slow flow.

$$\nabla \cdot v = 0 , \tag{2.1}$$

$$\nabla \cdot \pi = 0 , \tag{2.2}$$

$$r = p\,\delta + \tau , \tag{2.3}$$

$$\tau = \int_0^\infty M(s)\,\gamma_{[0]}\,(s)\,ds , \tag{2.4}$$

$$v = 0 \text{ on solid boundaries, i.e. } \theta = \pm \alpha . \tag{2.5}$$

Equation (2.4) is the constitutive equaiton for the UCGLV-EF [4,5]. A cylindrical coordinate system (r, θ, z) is chosen as in Fig. 1, with the z-axis coincident with the slit at the apex of the wedge. The assumed kinematics satisfying the mass conservation eqn. (2.1) are written as

$$v_r = -f(\theta)/r , \qquad v_\theta = v_z = 0 , \tag{2.6}$$

where f is an arbitrary function of θ to be determined. The strain tensor, $\gamma_{[0]}$, is readily calculated to be

$$\gamma_{[0]}(s) = \begin{pmatrix} -\dfrac{2fs}{r^2} - \dfrac{f'^2 s^2}{r^2(r^2 + 2fs)} & \dfrac{f's}{r^2 + 2fs} & 0 \\[3ex] \dfrac{f's}{r^2 + 2fs} & \dfrac{2fs}{r^2 + 2fs} & 0 \\[3ex] 0 & 0 & 0 \end{pmatrix} . \tag{2.7}$$

Combining eqns. (2.2—2.4) yields

$$\nabla p = -\int_0^\infty M(s) \ \nabla \cdot \gamma_{[0]}(s) \ ds \ , \tag{2.8}$$

which upon substitution of $\gamma_{[0]}$ gives two partial differential equations for the isotropic stress, p:

$$\frac{\partial p}{\partial r} = -\int_0^\infty M(s)\left\{\frac{4f'^2 s^2 + f'^2 s^2 + r^2 f'' s}{r^3(r^2 + 2fs)}\right\} ds \ , \tag{2.9}$$

$$\frac{\partial p}{\partial \theta} = \int_0^\infty M(s)\frac{2f's}{r^2 + 2fs} ds \ . \tag{2.10}$$

These are integrated to obtain

$$p = -\int_0^\infty M(s)\left\{\ln\left(1 + \frac{2fs}{r^2}\right)\left[\frac{1}{2} + \frac{1}{8}\left(\frac{f'}{f}\right)^2 - \frac{f''}{4f}\right] - \frac{1}{2r^2}\left(2fs + \frac{sf''}{2f}\right)\right\} ds + f_1(\theta) \ , \tag{2.11}$$

$$p = \int_0^\infty M(s)\ln(r^2 + 2fs) \ ds + f_2(r) \ . \tag{2.12}$$

where f_1 and f_2 are arbitrary functions of their arguments. For the two expressions for p to be identical, the following must be satisfied

$$f_1(\theta) = p_\infty \ , \tag{2.13}$$

$$f_2(r) = \int_0^\infty M(s) \ln r^2 \ ds + \int_0^\infty M(s)(sK/r^2) \ ds + p_\infty \ , \tag{2.14}$$

$$4f^2 + f'^2 = 4Kf \ , \tag{2.15}$$

$$\frac{1}{2} + \frac{1}{8}(f'/f)^2 - f''/4f = 1 \ , \tag{2.16}$$

for some constants K, p_∞. The general solution of (2.15—2.16) is

$$f(\theta) = K \cos^2(\theta + K_1) \ , \tag{2.17}$$

where K_1 is an arbitrary constant which, without loss of generality, may be set to zero. To satisfy the boundary conditions, f must be zero for some values of θ. Clearly the only possibilities are $\theta = \pm \pi/2$. Thus a solution is obtained for a 90° wedge and no other. The pressure distribution and the stress tensor, τ, are given by

$$p = -\int_0^\infty M(s)\left[\ln\left(1 + \frac{2Ks \cos^2\theta}{r^2}\right) - \frac{Ks}{r^2}\right] ds + p_\infty \ , \tag{2.18}$$

330

$$\tau = 2K \int_0^\infty \frac{M(s)\,s}{r^2 + 2Ks\,\cos^2\theta} \begin{pmatrix} -\cos^2\theta\left(1 + \dfrac{2Ks}{r^2}\right) & -\sin\theta\cos\theta & 0 \\ -\sin\theta\cos\theta & \cos^2\theta & 0 \\ 0 & 0 & 0 \end{pmatrix} ds . \quad (2.19)$$

A *local* Deborah Number can be defined for this flow as

$$De = 2\lambda K\,\cos^2\theta/r^2 = \xi^{-1}, \text{ say} . \qquad (2.20)$$

Figure 2 shows streamlines and lines of constant De for this flow. Notice that:

(i) the kinematics of the flow are identical to those of the corresponding flow of a Newtonian fluid;

(ii) the value of De on the solid boundaries is 0;

(iii) the stress and strain tensors, τ and $\gamma_{[0]}$, vanish identically on the boundaries.

By taking a particular form of the Memory Function, M, explicit values of τ and p can be calculated. As an illustration, let

$$M(s) = \eta/\lambda^2 \exp(-s/\lambda) , \qquad (2.21)$$

which represents a Maxwell fluid. The stress tensor and pressure become

$$\tau = \frac{2\eta K}{r^2} \begin{pmatrix} -1 + \sin^2\theta H(\xi) & -\sin\theta\cos\theta H(\xi) & 0 \\ -\sin\theta\cos\theta H(\xi) & \cos^2\theta H(\xi) & 0 \\ 0 & 0 & 0 \end{pmatrix} , \qquad (2.22)$$
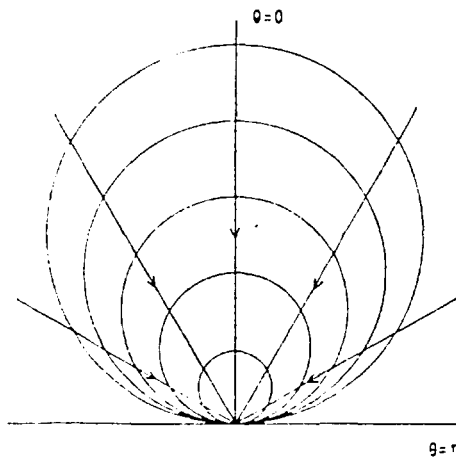

Fig. 2. Sketch of lines of constant local Deborah Number (————) and streamlines (——·——). Deborah Number increases as the origin is approached.
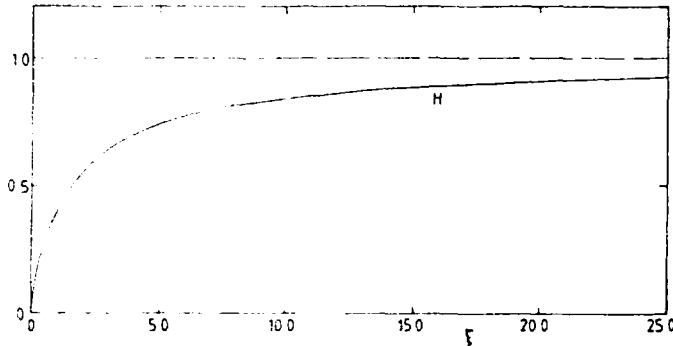
$$p = \frac{\eta}{\lambda}\left[\frac{\lambda K}{r^2} \quad \exp(\xi)\,E_1(\xi)\right] + p\,. \tag{2.23}$$

where $p\,.$ is an arbitrary constant, and E_1 is the exponential integral function. The function $H(\xi)$ is given by

$$H(\xi) = \xi(1 - \xi \exp(\xi)\,E_1(\xi)) \tag{2.24}$$

and is shown in Fig. 3. The stress tensor τ_N for the Newtonian solution is obtained in the limit as $De \to 0$, or $\xi \to \infty$, in which case $H \to 1$. If ratios are taken between corresponding components of τ and τ_N for the normal stress difference and the shear stress, the following are obtained:

$$\frac{\tau_{rr} - \tau_{..}}{\tau_{N_{rr}} - \tau_{N_{..}}} = (1 - H(\xi)(\sin^2\theta - \cos^2\theta))/2\cos^2\theta\,. \tag{2.25}$$

$$\tau_{r.}/\tau_{N_{r.}} = H(\xi),\ \theta \ne 0, \pm\pi/2\,. \tag{2.26}$$

Clearly, on any streamline apart from the solid boundary, the shear stress tends to 0 as the origin is approached and the normal stress difference ratio tends to a range of values in $[\frac{1}{2}, 1]$ depending on the angle of approach. The values of $\frac{1}{2}$ and 1 correspond to the centre line and solid boundary, respectively. An analytic solution has also been obtained for the Oldroyd Fluid B.

3. Brief investigation of the possibility of further solutions

Having obtained a solution for the flow in a converging channel of such a simple kinematic nature, an attempt was made to obtain further solutions by changing the geometry of the flow to a cone or by changing the type of viscoelastic fluid. Two examples are given below of the failure to obtain such solutions for the wedge flow of a corotational GLV-EF defined on page 339 of [4] and the convergent cone flow of an upper convected GLV-EF. These negative results suggest that the solution of Section 2 is isolated and does not belong to a family of such solutions with simple kinematics.

332

Corotational GLV-EF in wedge

Assuming the kinematics are given by (2.6) the corotating strain-rate tensor is calculated as

$$\dot{\Gamma} = \frac{1}{r^2(1 + 2fs/r^2)} \begin{pmatrix} f \cos\beta(s) + f' \sin\beta(s) & f \sin\beta(s) - f'\cos\beta(s) & 0 \\ f \sin\beta(s) - f' \cos\beta(s) & -f \cos\beta(s) - f' \sin\beta(s) & 0 \\ 0 & 0 & 0 \end{pmatrix},$$

where $\beta(s) = f'/2f[\ln(1 + 2fs/r^2)]$.

$$(3.1)$$

After substitution of $\dot{\Gamma}$ in the momentum conservation eqn. (2.2), the resulting expressions are not integrable in a closed form. However, if $\partial^2 p/\partial r \partial \theta$ is calculated from the r and θ components of (2.2), the resulting expressions should be identical. As can be verified after a lengthy calculation, they are not equal for any function, f, except trivially for f a constant.

Upper convected GLV-EF in converging cone

Let the kinematics be given by a non-zero radial component of the velocity

$$v_r = -f(\theta)/r^2 \qquad v_\theta = v_\phi = 0 \qquad (3.2)$$

which satisfies the mass conservation equation (2.1). It is readily shown that the strain tensor is given by

$$\gamma_{[0]} = \begin{pmatrix} 1 - \left(1 + \frac{3fs}{r^3}\right)^{4/3} - \left(1 + \frac{3fs}{r^3}\right)^{-2/3}\frac{f'^2 s^2}{r^6} & \left(1 + \frac{3fs}{r^3}\right)^{2/3}\frac{f'}{r^3} & 0 \\ \left(1 + \frac{3fs}{r^3}\right)^{2/3}\frac{f's}{r^3} & 1 - \left(1 + \frac{3fs}{r^3}\right)^{2/3} & 0 \\ 0 & 0 & 1 - \left(1 + \frac{3fs}{r^3}\right)^{2/3} \end{pmatrix},$$

$$(3.3)$$

Substitution of (3.3) into the momentum conservation equation produces three expressions for the derivatives of the pressure, which upon integration results in three expressions for p to be satisfied simultaneously

$$p = -\int_0^\cdot M(s)\left\{2\left(\frac{f'}{3f}\right)^2 + 2 - \frac{f''}{3f} - \frac{f'}{3f}\cot\theta - \left(1 + \frac{3fs}{r^3}\right)\left(1 + \left(\frac{f'}{3f}\right)^2\right)\right\}\left(1 + \frac{3fs}{r^3}\right)^{1/3} ds$$

$$+ f_1(\theta), \qquad (3.4)$$

$$p = -2\int_0^\cdot M(s)\left(1 + \frac{3fs}{r^3}\right)^{1/3} ds + f_2(r), \qquad (3.5)$$

$$p = f_3(r, \theta), \qquad (3.6)$$

where f_1, f_2, f_3 are arbitrary functions of their arguments. However, these equations are incompatible and because of the term involving

$$(1 + 3fs/r^3)^{4/3} \tag{3.6}$$

in (3.4), no such p exists except trivially for f a constant.

4. Comparison with experiment

Han and Drexler have published results of experimental measurements of stress in a $180°$ wedge using a birefringence technique. They consider the shear stress and normal stress difference in a rectangular Cartesian coordinate system. Hence the results of Section 2 must be converted to $\tau_{xx} - \tau_{yy}$ and τ_{xy} from $\tau_{rr} - \tau_{\theta\theta}$ and $\tau_{r\theta}$ to enable a comparison to be made. They also use a different sign convention in their definition of τ from that used in (2.3); therefore let $s = -\tau$. The transformation required is readily calculated as

$$s_{xx} - s_{yy} = (\tau_{rr} - \tau_{\theta\theta}) \cos 2\theta - 2\tau_{r\theta} \sin 2\theta \tag{4.1}$$

$$s_{xy} = -\tau_{r\theta} \cos 2\theta - \tfrac{1}{2}(\tau_{rr} - \tau_{\theta\theta}) \sin 2\theta$$

in which the y-axis corresponds to $\theta = 0$. For the purposes of comparison the stresses for a Maxwell Fluid are used as in (2.22). Substitution of $\tau_{rr} - \tau_{\theta\theta}$ and $\tau_{r\theta}$ in (4.1) obtains

$$s_{xx} - s_{yy} = -(2\eta K/r^2)(\cos 2\theta + H(\xi) \cos 4\theta) ,$$

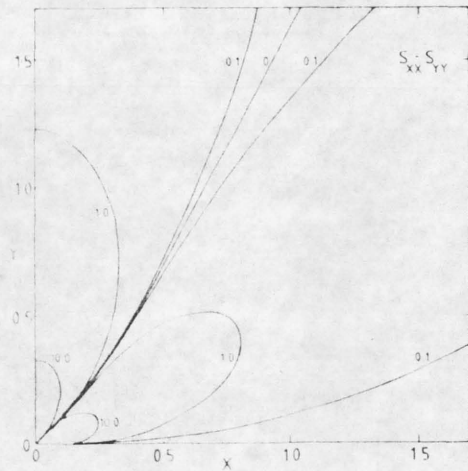$$s_{xy} = (\eta K/r^2)(\sin 2\theta + H(\xi) \sin 4\theta) . \tag{4.2}$$

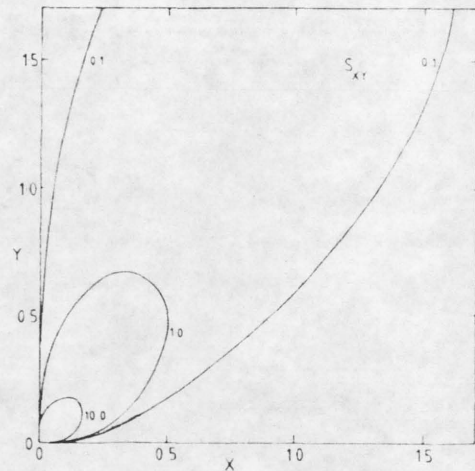Fig. 4. Graph of curves of constant $S_{XX} - S_{YY}$; theoretical.

Fig. 5. Graph of curves of constant S_{XY}; theoretical.

334

Finally, all variables are written in a dimensionless form

$$x = X(2\lambda K)^{1/2}, \qquad y = Y(2\lambda K)^{1/2},$$

$$\bar{s}_{xx} - \bar{s}_{yy} = (\eta/\lambda)(S_{XX} - S_{YY}), \qquad \bar{s}_{xy} = (\eta/\lambda)\,S_{XY}.$$

(4.3)

Figures 4 and 5 show curves of constant $S_{XX} - S_{YY}$ and S_{XY} respectively for half of the stress field; the line $x = 0$ is a line of symmetry, since $S_{XX} - S_{YY}$ is an even function of θ and S_{XY} is an odd function of θ. The x-axis corresponds to a solid boundary and the origin to the position of the sink. Values of the dimensionless stresses are indicated alongside each curve. Figure 6 and 7 show replotted versions of Figs. 13 and 14 of Han and Drexler [3] for a poly-styrene melt, Dow Chemical Styron 686. In Figs. 6 and 7 the fluid exits via a parallel-sided channel as indicated by the line drawn at $x = 0.192$. Again only half the stress field is shown. In order to draw these curves in the dimensionless variables of (4.3), values of η and λ were estimated from viscometric flow data for the melt Styron 686 as reported in [5]. Both parameters were taken as the limiting values at vanishing shear rate:

$$\eta = \eta_0 = 3 \times 10^5 \text{ poise},$$

$$\lambda = \lim_{\dot{\gamma} \to 0} \frac{N_1(\dot{\gamma})}{2\dot{\gamma}^2 \eta_0} = 2.5 \text{ secs},$$

where N_1 is the normal stress difference in steady shear flow.

Qualitatively, the agreement between the theoretical and experimental curves in Figs. 4—7 is good and the values of the stresses are of the same order of magnitude. In fact, the theoretical results predict stresses approximately a factor of 3 larger than the reported experimental values. A quantita-
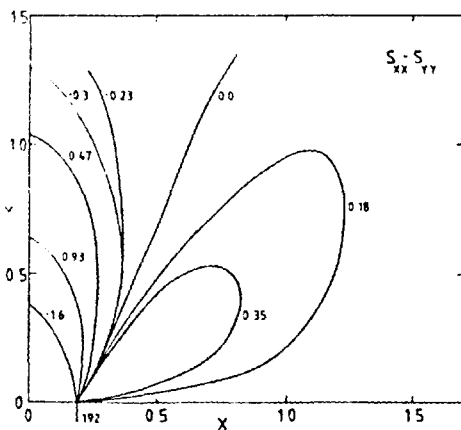

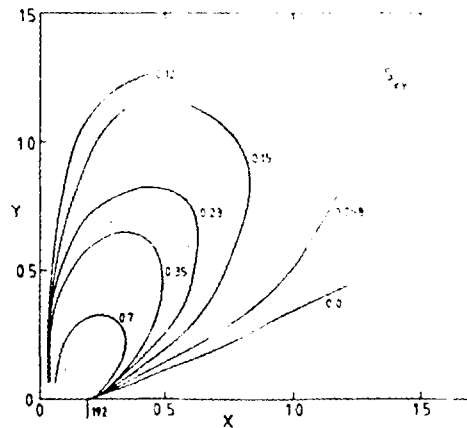Fig. 6. Graph of curves of constant $S_{XX} - S_{YY}$; experimental.

Fig. 7. Graph of curves of constant S_{XY}; experimental.

tive comparison, however, is of limited value primarily because of the finite width of the exit used for the experimental results and the inadequacy of any model of the UCGLV-EF type in describing observed melt behaviour. Good qualitative agreement is also achieved with the experimental results for two other melts, high density polyethylene and polypropylene, as reported in Han and Drexler [3].

5. Discussion

Previous attempts to obtain solutions for the wedge flow of an Upper Convected Maxwell Fluid include that of Strauss [6], who obtains a series solution in terms of decreasing powers of r of the form:

$$\psi(r, \theta) = \sum_{n=0}^{\infty} \frac{\psi_n(\theta)}{r^n},$$

$$S_{rr} = \sum_{n=0}^{\infty} \frac{a_n(\theta)}{r^n}, \qquad S_{r\theta} = \sum_{n=0}^{\infty} \frac{b_n(\theta)}{r^n}, \qquad S_{\theta\theta} = \sum_{n=0}^{\infty} \frac{c_n(\theta)}{r^n}, \tag{5.1}$$

where ψ is a stream function and S the stress tensor. Using the results of Section 2, his result is retrieved by expanding (2.22) in powers of $1/r$ for the special case of $\alpha = \pi/2$ and slow flow. However, the expansion is an asymptotic diverging series for the stresses $S_{rr}, S_{r\theta}, S_{\theta\theta}$ because of the terms involving $\exp(\xi) E_1(\xi)$. This suggests that (5.1) is an asymptotic diverging series expansion for all values of α, certainly for $\alpha = \pi/2$, and is valid only far from the origin. Therefore, serious doubt is cast on the meaning of Strauss' Figs. 7–10 which show streamlines for wedge flow at various values of α, at low Reynolds Number, and the position of a separation point in the flow field. Perhaps what is required is a series solution in ascending powers of r to obtain information about the flow near the origin.

5. Conclusions

Although the results of Section 3 in no way constitute a proof, it seems likely that the solution in Section 2 is an isolated result. However, it is useful as an indication of the magnitude of the stress involved in wedge flow. The most remarkable characteristic of the solution is that, following any streamline towards the origin, the magnitudes of the normal stress difference and the shear stress become increasingly smaller than the corresponding values for a Newtonian fluid of similar viscosity, η.

Acknowledgements

336

preparation of this paper. He also gratefully acknowledges the financial
support of the Science Research Council and Avon Rubber Company, and
the permission of John Wiley and Sons, publishers, to use figures from the
Journal of Applied Polymer Science.

Notation

De local Deborah Number
E_1 exponential integral function as defined in [7]
f arbitrary function specifying velocity field
H particular function defined in (2.24)
K arbitrary constant
M memory function
p isotropic stress or pressure
s time difference between present and past time
S dimensionless stress tensor
v velocity vector
X, Y dimensionless cartesian coordinates
α wedge half-angle
β particular function defined in (3.1)
$\gamma_{[0]}$ strain tensor in upper convected formalism
$\dot{\gamma}$ deformation rate or strain rate tensor
δ identity tensor
η fluid viscosity
λ fluid relaxation time
π momentum flux tensor
τ stress tensor
τ_N stress tensor for Newtonian fluid
ξ auxiliary symbol designating the inverse of the Deborah Number

References

1 L. Rosenhead, Proc. Roy. Soc. A, 175 (1940) 436—467.
2 C.D. Han and L.H. Drexler, J. Appl. Polym. Sci., 17 (1973) 2369–2393.
3 C.D. Han and L.H. Drexler, J. Appl. Polym. Sci., 17 (1973) 2329–2354
4 R.B. Bird, R.C. Armstrong and O. Hassager, Dynamics of Polymeric Liquids, John
   Wiley & Sons, New York 1977, p. 445.
5 C.D. Han, K.V. Kim, N. Siskovic and C.R. Huang, J. Appl. Polym. Sci., 17 (1973)
   95–103.
6 K. Strauss, Acta Mechanica 20 (1974) 233—246.
7 M. Abramowitz and I.A. Stegun, (eds.), Handbook of Mathematical Functions,
   Applied Maths Series No. 55, U.S. Nat. Bureau of Standards, Washington D.C., 1964,
   p. 228.